Arrangement and structure of α-actinins in striated muscle

Brendan Rogers

Submitted in accordance with the requirements for the degree of

Doctor of Philosophy

The University of Leeds

Faulty of Biological Sciences

September 2018

The candidate confirms that the work submitted is his own except work which has formed part of jointly authored publications has been included. The contribution of the candidate and the other authors to this work has been explicitly indicated below. The candidate confirms that the appropriate credit has been given within the thesis where reference has been made to work of others.

The co-sedimentation assays of the wild-type α-actinin actin binding domain and the mutants G111V and A119T with filamentous actin shown in Chapter 5 contributed to the co-sedimentation assays reported in Haywood *et al.* 2016. These were jointly conducted by myself and Dr Marcin Wolny.

This copy has been supplied on the understanding that it is copyright material and that no quotation from the thesis may be published without prior acknowledgement.

Acknowledgements

Firstly, I would like to thank to my supervisor, Michellle Peckham, for all the help and guidance these past four years and a very big thank you to everyone in the Peckham lab. There are a lot of people to thank for the help I got during the PhD. Thanks to Ruth Hughes for all the general help in the lab, preparing the cardiomyocytes and help with the microscopes. Thank you to Alistair Curd for the help analysing of the dSTORM data. Thanks to Chi Trinh for all the crystallography help. Also, thanks to Christian Tiede for generating the Affimer sequences.

Special thanks to my colleague Glenn Carrington and my friend Marcus Holt, for all the lab chat and coffee breaks these past few years.

Finally, I would like to thank my parents for the support they have always given me.

Abstract

The smallest contractile unit within striated muscle cells are called sarcomeres. The boundary regions between sarcomeres are called Z-discs, which contain over 30 different proteins, organised within a narrow ~100 nm wide structure. Standard fluorescence microscopy approaches do not reveal the arrangement of Z-disc proteins, as the width of the Z-disc is below the resolution limit (~250 nm). The arrangement of the actin filaments and the cross-linking proteins α-actinin in the Z-discs are well characterised by electron microscopy (EM) studies, however other Z-disc proteins are not. With the development of super-resolution fluorescence microscopy techniques, it is now possible to obtain Z-disc protein localisation information. Here, dSTORM (direct Stochastic Optical Reconstruction Microscopy) was used, to investigate the arrangement of α–actinins in Z-discs of cardiomyocytes, and then the arrangement of the N-terminal ends of the giant protein titin in the Z-discs. Affimers were generated to bind α–actinin 2 and the N-terminal titin domains (Z1/Z2), to use as binders in dSTORM. Affimers are small (~12 kDa) non-antibody binding proteins, about 1/10th the size of antibodies, that can be selected to bind to a specific protein. The localisation data of dSTORM using the Affimer binders showed the same regular arrangement of α-actinins observed in EM studies. The use of dSTORM with Affimers also suggests the titin Z1/Z2 domains do not only localise at the edges of the Z-discs but arranged throughout the Z-disc with regular spacing (~25 nm) in the transverse plane of the Z-discs.

Also, three mutations located in the actin binding domain of α-actinin 2 associated to hypertrophic cardiomyocytes (G111V, A119T and M228T) were characterised by *in vitro* co-sedimentation assays with actin. The mutants G111V and A119T did not show a significant difference in binding affinity to actin compared to the wild-type. The co-sedimentation assays did however suggest the mutation M228T significantly increases the binding affinity of α–actinin 2.

Table of contents

Chapter 1 - Introduction

1.1 Sarcomeres and Z-discs

Cardiac and skeletal striated muscle cells have highly ordered cytoskeletons with bundles of myofibrils running the length of the cells. Each myofibril is composed of repeating units of sarcomeres, the smallest contractile unit within striated muscle cells. The repeat, parallel order of the sarcomere units within the myofibrils allows for contraction and relaxation of the cells. The basic structure of a sarcomere can be described as a repeat array of inter- laying thick myosin motor filaments and thin actin filaments (**Figure 1.1**). Distinct lateral regions have been observed within sarcomeres by electron microscopy; the Z-disc, I-band, A-band and the M-line. The Z-discs, Z-bands or Z-lines are observed as dense boundary regions between sarcomeres. These boundary regions form highly complex network of proteins, which needs to maintain structural stability during contraction and transmission of force between sarcomeres. Also, major signalling pathways are thought to occur in the Z-discs (reviewed in **Frank and Frey 2011**). The thick myosin filaments extend the A-band region and are not present in the I-bands or the Z-discs (**Figure 1.1**). Filamentous actin, the major component of the thin filaments extends from the Z-discs through into the A-band. Within the Z-discs the barbed ends of the actin filaments are stabilised by the actin capping protein CapZ (**Schafer *et al.* 1995**). Actin filaments from adjacent sarcomeres meet at the Z-disc and are cross linked via α-actinins (**Figure 1.1**), thus the Z-discs are commonly described as the anchoring points between sarcomeres.

The giant proteins nebulin and titin are also integral players within the sarcomere cytoskeleton. Titin (~3 MDa), spans half the sarcomere starting in the Z-disc and ending at the M-line (**Labeit *et al.* 1995, Figure 1.1**). Titin in the A-band is composed of a super repeat pattern of four immunoglobulin-like domains and seven fibronectin type 3 domains and interacts with the thick filaments via myosin binding protein C and the myosin tail (**Houmeida *et al.* 1995, Labeit *et al.* 1995 Freiburg *et al.* 1996**). Titin in the I-band has been termed a molecular spring due to repeat PEKV domains which have elastic properties (**Linke *et al.* 1998, 1999**). The N-terminal end of titin (~ 60 kDa) is within the Z-disc region (**Gregorio *et al.* 1998**), The N-terminus of titin (residues 1-200) is composed of two Ig-like domains, the Z1/Z2 domains. The Z1/Z2 domains from two different titin molecules are thought to be cross-linked by the small protein telethonin (19 kDa) at the periphery of the Z-discs (**Mues *et al.* 1998, Zou *et al.* 2006**). Analysis of the primary sequence from human cardiac titin has shown seven short 45 residue Z-repeat domains are present in the Z-discs, that have been proposed to act as

a scaffold for the α-actinins (**Gautel *et al.* 1996, Sorimachi *et al.* 1997**).

Nebulin (~ 800 kDa) extend the length of the actin filaments and is composed of ~185 α-helical repeat domains (35 residue, M-domains) (**Labeit *et al.* 1995**), which interact each with actin. Vertebrate cardiac muscle only exhibits low level expression of nebulin (**Kazmierski *et al.* 2003**). However, cardiac muscle also expressed a smaller homologue, nebulette (~ 100 kDa), which has twenty-three M-domains and is only present within the Z-discs and extends into the I-band (**Moncman *et al.*1995, Millevoi *et al.* 1998**), Within the Z-discs nebulin/nebulette have highly conserved domains at the C-terminal end; a Src homology 3 domain (SH3) domain and a linker region (**Labeit *et al.* 1995**). From the position of known binding partners (**Pappas *et al.* 2008, Ma *et al.* 2002, Bang *et al. 2002***) a model has been put forward where the C-terminal domain is at the periphery of the Z-discs by single nebulin molecules extending fully into the Z-disc region and crossing actin filaments from adjacent sarcomeres (**Pappas *et al.* 2008**) (**Figure 1.1**).

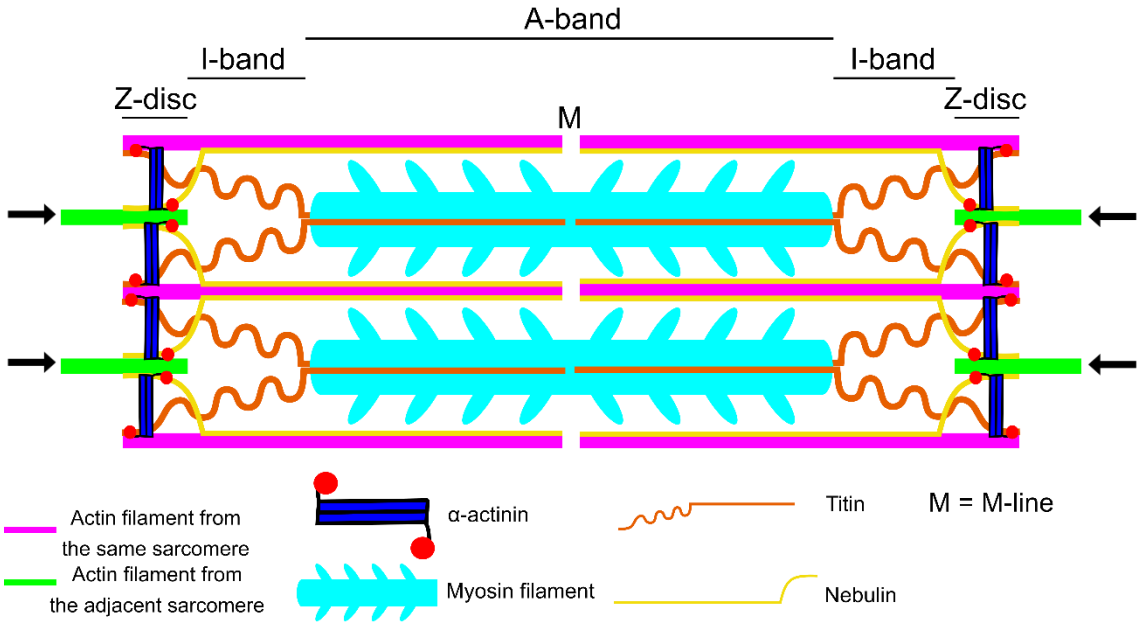

Figure 1.1 – Sarcomere assembly in striated muscle cells. Sarcomeres, the smallest contractile unit in striated muscle, are composed of repeat arrays of inter-laying filaments. The ordered localisation of sarcomeric proteins results in the appearance of distinct lateral bands within each sarcomere unit: the M-line, A-band, I-band and the Z-disc (the boundary region between sarcomere units). The thick myosin filaments span the A-band whilst the interlaying thin actin filaments extend from the Z-disc to the M-line. Within the Z-discs opposing actin filaments from neighbouring sarcomeres are cross-linked by α-actinins. The giant protein titin spans half the sarcomere, extending from the Z-disc to the M-line and is bound to the thick myosin filament in the A-band. The giant protein nebulin also spans half the sarcomere bound to the thin actin filament ending in the Z-disc region.

1.2 Viewing Z-discs by electron microscopy (EM)

The protein dense Z-disc structure within striated muscle has been commonly studied by electron microscopy (EM). The Z-discs are seen as dense regions between sarcomeres in longitudinal views of striated muscle sections. A distinct zig-zag pattern can also be seen in the Z-discs, which are thought to be links between the actin filaments in the Z-disc. The width of Z-discs and the number of zig-zag layers vary depending on the muscles type. Both cardiac and skeletal slow muscle have wide Z-discs (100-140 nm, **Luther *et al.* 2003**) and three zig-zag layers are present spaced ~ 38 nm apart.

Viewing transverse sections of striated muscle by EM have shown the Z-discs to have an ordered lattice structure. Two different conformations within the Z-discs of muscle tissues have been observed; the small square lattice (**Figure 1.2A**) and the basket weave (**Figure 1.2B**). A mixture of the two conformations are commonly seen in muscle samples by EM. These two distinct conformations were also observed by X-ray diffraction in rabbit psoas muscle (**Prez-Edwards *et al.* 2011**). In the same study under relaxed conditions, 89 % of the Z-disc lattice was thought to be small square. Under tension the small square conformation was reduced to 36 %. This study suggests both conformations are present in the Z-discs no matter the conditions, however the ratio between the conformations change.

The lattice spacing (the distances between actin filaments from the same sarcomere) has been reported for many different muscle types. The lattice spacing in the Z-discs of rat papillary muscle was initially proposed to be at ~ 20 nm for the small square lattice conformation (**Goldstein *et al.* 1989**). This is consistent with to the lattice spacing of skeletal muscle reported at a similar time (**Goldstein *et al.* 1986**). In a more recent study however, the lattice spacing was found to be ~ 30 nm (**Burgoyne *et*. *al* 2015)**. The reason for this 50 % increase compared to initial reports is unclear. The lattice spacing for the basket weave conformation in cardiac muscle has also been reported to be 24 nm, a 20 % increase upon the small square (**Goldstein *et al.* 1989**). More recently, only an 8 % increase in lattice spacing from the small square to the basket weave conformations of rabbit psoas muscle was observed (**Prez-Edwards *et al.* 2011**). This is a much smaller increase than for cardiac muscle reported, however the discrepancy could be explained by the different muscle samples used.

1.2.1 3D models of the Z-disc

Via electron microscopy techniques, 3D density maps of Z-discs in different conformations and from different muscle types have been generated. Actin filament rods and α-actinin cross-links between the filaments have been fitted into these density maps. A 3D model was generated by EM for the Z-disc structure of nemaline rods (**Figure 1.2C, Morris *et al.* 1990**). Nemaline rod structures are found in the skeletal muscle cells of patients with nemaline myopathy, a congenital disease which causes muscle weakness (**Sewry and Wallgren-Pettersson 2017**). Nemaline rods have distinctly larger Z-discs (1 -2 μm in width) than normal Z-discs (~ 50 -140 nm in width) and lattice conformation is very similar to that of the small square lattice, when viewed by EM. In this model the rod domains of the α-actinin homodimers are parallel to the actin filaments. Two separate α-actinin molecules are found close together on the same actin filament linking different actin filaments from the neighboring sarcomere. They are separated by an axial rise of 2.74 nm (a single G-actin subunit) and are orientated differently on the actin filament by 167.4°. The α-actinins bound are proposed to follow the 4^3 screw symmetry of the actin filament. Each pair of α-actinins are arranged regularly along the actin filament, spaced 19.2 nm apart and rotated 90 ° from each other (equivalent to every seventh G-actin subunit).

Most recently electron tomography with sub-tomographic averaging has been used to study the small square lattice structure within the Z-discs of rat papillary muscle (**Burgoyne *et al.* 2015**). In this study a density map of the small square lattice with three layers of α-actinin molecules was obtained to a resolution of 8 nm. The Morris *et. al* model for nemaline rods was fitted to this density map for the small square lattice. Thus far Z-discs have been observed to have 2, 3, 4 and 6 α-actinin layers (**Luther 2009**). 3D models of different layered Z-disc in the basket weave conformation have been solved from different muscle types and organisms. These included; the Z-disc from fish white muscle (two α-actinin layers, **Luther 1991**), the Z-disc from fish fin muscle (three α-actinin layers, **Luther 2000**) and the Z-disc from bovine neck muscle (six α-actinin layers, **Luther *et al.* 2002**). In these models the rod domain of the α-actinins are at a different angle to the actin filaments (**Figure 1.2D**) thought to be a result of the increased lattice spacing of the basket weave to the small square lattice. EM studies of the Z-discs have given insights into the conformation the Z-disc lattice structure and the arrangement of both the actin filaments and the α-actinin links. However, the resolution of the models generated have yet to reach a resolution to fit any other Z-disc proteins in the lattice structure.

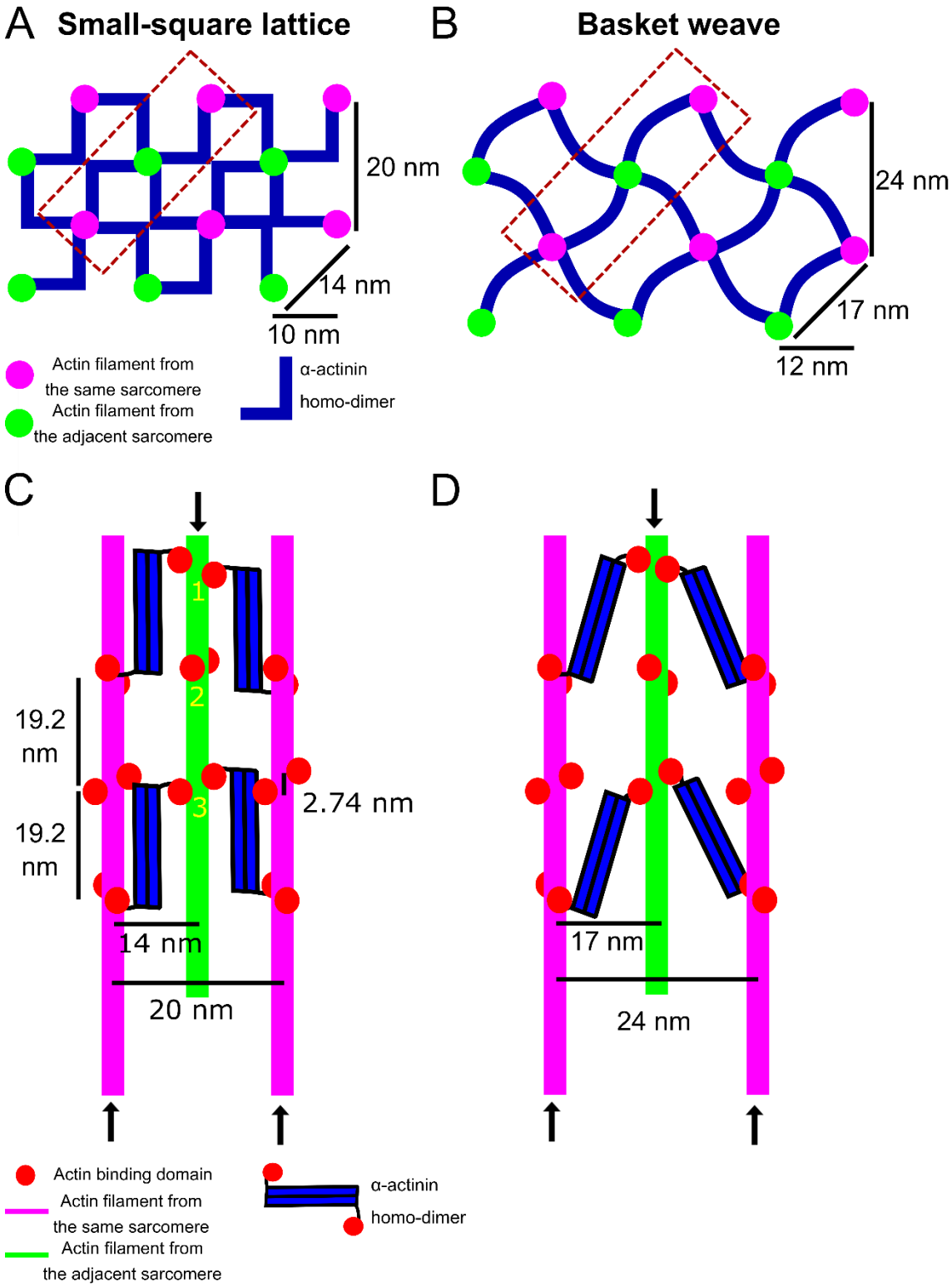

Figure 1.2 – Conformations of the Z-disc. (**A, B**) Transverse views of the Z-disc in the different conformational states; the small-square lattice and the basket weave. (**C**) Side on view of the red boxed Z-disc region (see **A**) (showing three α-actinin layers per actin filament, labelled 1, 2 and 3 in yellow) in the small-square lattice conformation based on 3D models (**Morris *et al.* 1990, Burgoyne et al. 2015**). (**D**) Side on view of the red boxed Z-disc region (see **B**) (showing three α-actinin layers per actin filament) in the basket weave conformation based on 3D models (**Luther *et al.* 2002**). Lattice spacing measurements reported in **Goldstein *et al.* 1989** are shown.

1.3 α-actinin

1.3.1 The domains of α-actinin

There are four different human isoforms of α-actinin; the non-muscle ubiquitous isoforms 1 and 4 and the muscle isoforms 2 and 3. The four different α-actinin isoforms are part of the spectrin superfamily and have a highly conserved primary sequence (**Sjoblom *et al.* 2008**). The non-muscle α-actinin 1 mainly localizes to focal adhesions within cells (**Pavalko and Burridge 1991**) and α-actinin 4 localizes to membrane ruffles in migrating cells (**Honda *et al.* 1998**). The muscle isoforms localize to the Z-discs of striated muscle and where they cross-link the actin filaments. α-actinin 2 and 3 have a sequence identity of 93 %, however isoform 3 is only expressed in skeletal muscle, whilst isoform 2 is expressed in skeletal and cardiac muscle (**Beggs *et al.* 1992**). Thus, α-actinin 2 (103.9 kDa, 894 amino acids) is generally considered the dominant muscle isoform. Muscle α-actinin 2, like the other isoforms, is ~ 360 Å in length and has three distinct domains; the N-terminal actin binding domain (ABD), the central spectrin rod domain and the C-terminal camodulin like (CAM) domain (**Figure 1.3**).

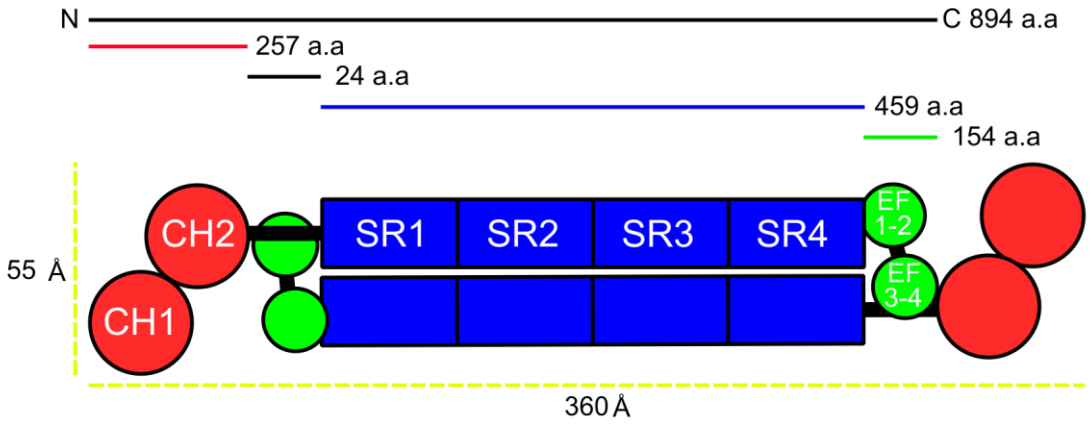

Figure 1.3 - The domains and conformation of the full length α-actinin 2. Two α-actinin monomers (each 894 amino acids in length) interact with each other in an anti-parallel fashion for cross-linking filamentous actin. The N-terminal actin binding domain (ABD) (red) is composed of a tandem calponin homology domain pair. The rod domain (blue) is composed of four spectrin repeats and is the main interaction point for the other α-actinin homodimer. The ABD and rod domain are connected by a helical linker region. The C-terminal calmodulin-like domain (green) is composed of two EF-hand pairs. The EF 3-4 hand pair interact with the linker region of the opposing α-actinin monomer. The measurements of the homodimer were taken from the crystal structure of α-actinin 2 (**Ribeiro *et al.* 2014**, **PBD code 4D1E**).

The N-terminal actin binding domain (ABD) (**Figure 1.3**) is made up of two calponin homology (CH) domains. CH domains are commonly found in the spectrin family (**Gimona *et al.* 2002**). Each globular CH domain is commonly composed of four large α-helices and two smaller α-helices (referred to as α-helices A, B, C, E, F and G). The rod domain or spectrin repeat domain of α-actinins is composed of four spectrin repeats (SR), extended bundles of three α-helices (**Djinovic-Carugo *et al.* 1999**). The rod domains of two α-actinin monomers is the main interaction point for the α-actinin homodimer and these have a very high affinity for one another (Kd ~ 10 pM) (**Flood *et al.* 1995**). Crystallographic structures of the rod domain homodimer (**Ylanne *et al.* 2001, Ribeiro *et al.* 2014**) show a left-handed 90° twist from one end to the other. This is key for the ABDs of the α-actinin homodimer to be in the right orientation to crosslink actin filaments from adjacent sarcomeres in the Z-disc lattice. The rod domain is also thought to be the main interaction point for other Z-disc proteins as many exposed negatively charged residues found on the surface of each SR domain (**Ylanne *et al* 2001**). The C-terminal CAM domain comprises of two pairs of calcium insensitive EF hands. The EF hand motifs are common helix-loop-helix binding domains. The role of the first pair (EF 1-2) of EF hands is unclear, however the second pair (EF 3-4) binds to the Z-repeats of titin within the Z-discs (**Young and Gautel 2000, Atkinson *et al.* 2001**).

1.3.2 Conformation of the N-terminal actin binding domain (ABD)

The crystallographic structures of the ABD of all the human isoforms of α-actinin (**Frazot *et al*. 2005, Borrego-Diaz *et al*. 2006, Lee *et al.* 2008, Haywood *et al.* 2016. PDB codes 1WKU,2EYI, 2R0O, 5A36**) show two CH domains (CH1 and CH2) in a closed compact conformation, with extensive contacts between the domains. The structure for α-actinin 2 ABD shows a N-terminal α-helix preceding the CH1 domain that had not been resolved in the other isoform structures (**Haywood *et al.* 2016**) (**Figure 1.4A**). This N-terminal helix is thought to be flexible. For the CH domains of α-actinin 2; five α-helices form the CH1 domain (A, C, E, F and G) and six α-helices form the CH2 domain (A, B, C, E, F and G) and α-helices A and G of CH1 and the area between helices E to G of CH2 form contacts with the opposite CH domain (**Figure 1.4B)**. Analytical ultra-centrifugation (AUC) of α-actinin 4 suggests the CH1-CH2 domains are predominantly in the closed conformation when free in solution and crystal structure conformations are not crystal packing artefacts (**Lee *et al.* 2008**). The residues involved in contacts between CH domains are conserved in all four isoforms. At the interface, the majority of the residues form weak hydrogen bonds with the main chain of the opposing CH domain. For α-actinin 2 (**PDB code 5A36**) the residues Q39,

K42 and T43 on the α-helix A of CH1 form hydrogen bonds with the main chain of CH2 (**Figure 1.4C**). Whilst H254 from CH2 forms a hydrogen bond with the main chain of CH1 near the linker loop (**Figure 1.4C**). The crystal structures of the other α-actinin isoforms do not show the equivalent contact between K42 and the CH2 main chain, however all the other main chain interactions are conserved.

There are also direct contacts between residues of opposing CH domains. There is direct hydrogen bonding between Q40 (CH1) and D241 (CH2) (**Figure 1.4D**). The crystal structure shown here (**PDB code 5A36**) shows R53 at the C-terminal end of the second helix positioned to form a H-bond with the main chain oxygen of D224 (**Figure 1.4E**). In all other ABD crystal structures solved of α-actinin 2 and the other actinin isoforms a salt bridge forms between these two residues. This difference suggests there is some flexibility in this region. For α-actinin 1, the interaction between the residue pair to W128 (CH1) and K236 (CH2) has been suggested to be an important interaction at the interface (**Borrego-Diaz *et al*. 2006**). This interaction mainly involves hydrophobic interactions with occasional π-cation interaction (**Crowley and Golovin 2005**) and the residue pair highly conserved in the spectrin family (with the lysine is sometimes replaced with either an arginine or glutamine). Muscle α-actinin 2 is the only human isoform to have an arginine in place of a lysine in the interaction pair (R243 (CH2), **Figure 1.4F**). An arginine near an aromatic side chain is more likely to form a π-cation interaction compared to lysine (**Crowley and Golovin 2005**). Therefore, if the interaction is important to the stability of the interface, the CH domain interface of α-actinin 2 should be the most stable of all the isoforms. However, a mutant of α-actinin 4 with the lysine in the residue pair replaced with a glutamate (K225E) was shown to have the same conformation as the wild-type by analytical ultra-centrifugation (**Lee *et al.* 2008**). This tryptophan and lysine (or arginine) interaction may not be important in maintaining the interface alone, however it may contribute to the overall stabilisation of the closed conformation.

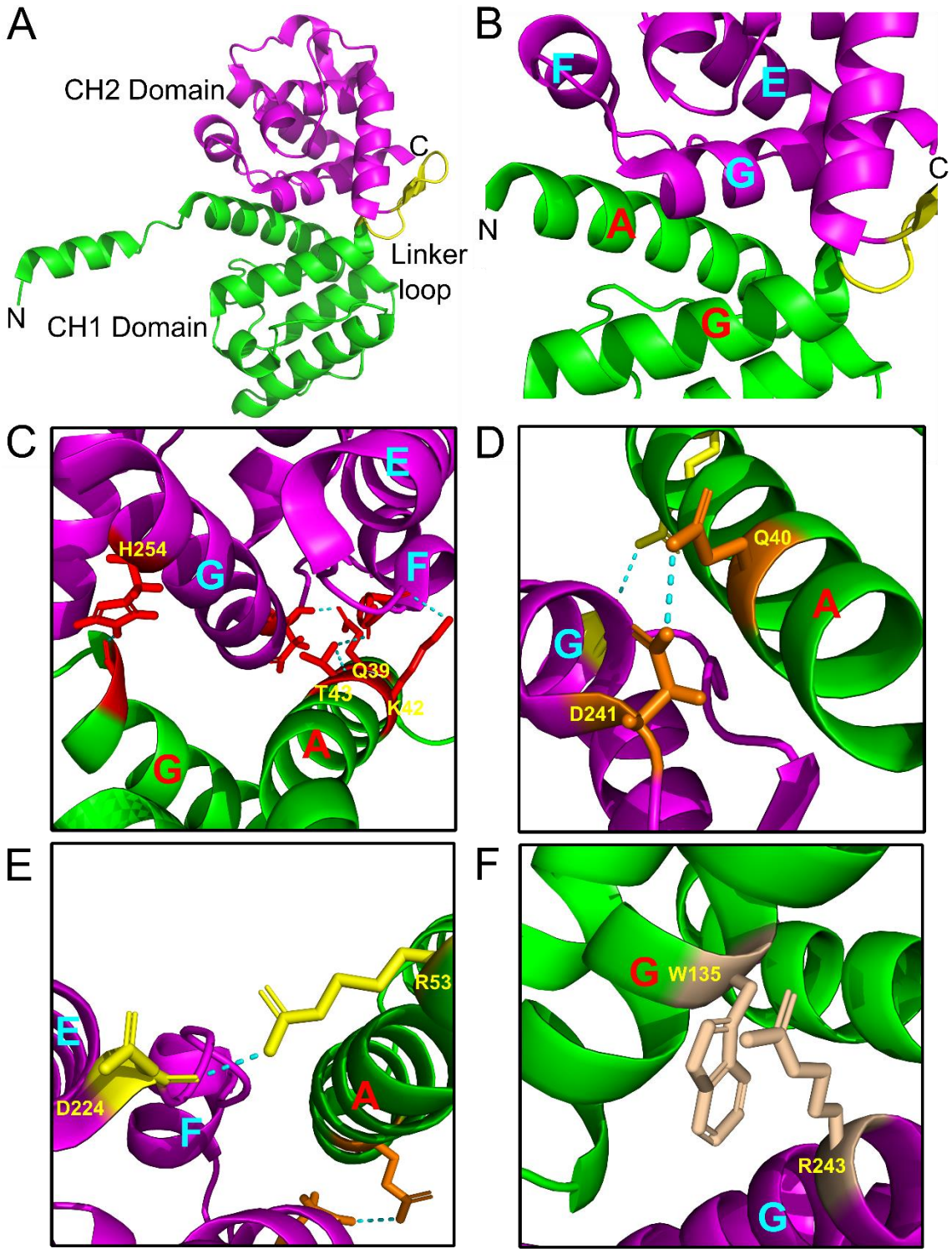

Figure 1.4 – Interactions between the CH domains of α-actinin 2.
(**A**) Crystallographic structure of the ABD (residues 19 – 257) resolved to 2.0 Å (**Haywood *et al*. 2016, PDB code 5A36**). The CH1 domain (green) and the CH2 domain (magenta) are connected by a short nine residue linker loop (yellow). (**B**) CH1-CH2 interface with the α-helices involved in formation of the interface labelled. Helices A and G from CH1 and helices E, F and G from CH2. (**C**) The residues (red) involved in forming weak hydrogen bonding with the backbone of the opposite CH domain. (**D**) Direct H-bonding between Q40 (CH1) and D241 (CH2). (**E**) Interaction between R53 (CH1) and D241 (CH2). (**F**) Residue pair W135 (CH1) and R243 (CH2) involved in hydrophobic and π-cation interactions.

1.3.3 The actin binding sites of α-actinin

Various co-sedimentation assays with actin filaments have been used with different deletion constructs of the ABD (CH1-CH2) from various proteins to assess what regions are important for binding actin. The ABD from smooth muscle chicken α-actinin has been found to interact with filamentous actin (Kd = 4.7 μM) but not monomeric actin (**Way *et al*. 1992**). The same study also found the CH2 domain alone does not bind actin, whilst the CH1 domain does. However there was a ten-fold increase in affinity between the CH1 alone and the CH1-CH2 pair suggesting the CH2 does play a role in the ABD:actin interaction. Further studies identified a major actin binding site (residues 120-134) (**Kuhlman *et al.* 1992, Hemmings *et al.* 1992**), referred to in other literature as actin binding site 2 (ABS 2). The equivalent region in human muscle α-actinin 2 (residues 126-140) is fully conserved and located on the last α-helix (helix G) of the CH1 domain (**Figure 1.5A**). For other spectrin family proteins with two CH domains (filamin and ABP-120), actin binding regions have been identified at a similar position (**Bresnick *et al.* 1990, Bresnick *et al.* 1991, Lebart *et al.* 1994**).

Two actin binding sites have also been identified on the ABD of human dystrophin by proton NMR (**Levine *et al.* 1992**); ABS1 (residues 17-26) and ABS 3 (residues 128-156) (**Figure 1.5B**). ABS 1 has been found to be the most prominent actin binding site by co-sedimentation of deletion constructs (**Fabbrizio *et al.* 1993**). It has commonly been suggested that the equivalent regions in α-actinins (residues 40-49 and residues 141-173) (**Figure 1.5B**) are involved in actin binding as dystrophin and α-actinin are both part of the spectrin superfamily and they both have two CH domains. However, from the studies mentioned above, it is unclear if the CH domains of dystrophin and α-actinin interact with actin filaments in the same way. α-actinin constructs only containing either ABS 1 and ABS 3 only show weak affinity to actin (**Kuhlman *et al.* 1992**), which is the opposite to that found for dystrophin. Also, a KTFT motif is present in spectrin family members within ABS 1, is not critical for binding actin (**Corrado *et al.* 1994**). In addition, ABS 2 has not been identified as an actin binding site for dystrophin despite a number of conserved resides being present in both α-actinin and dystrophin (**Figure 1.5B**). The residues present in the ABS 2 of α-actinin that are not present in the ABS of dystrophin (**Figure 1.5B, red**) may be important for the α-actinin:actin interaction.

On the other hand, the full length α-actinin ABD has a higher affinity for actin than partial constructs which contain ABS 2 (**Kuhlman *et al.* 1992**), suggesting the presence of other weaker actin binding sites. In addition, the affinities of the α-actinin 2

and dystrophin CH domains for actin are comparable (7.5 µM and 5.9 µM) (**Haywood *et al*. 2016** and **Fabbrizio *et al.* 1993**). Interactions of the ABD of α-actinin and actin may involve the conserved residues situated in ABS 1 and 2**.**

The studies outlined above were performed before the crystallographic structures of the ABD from the α-actinin isoforms were solved. There is a clear actin binding region within ABS 2 (in CH1) and ABS 3 (in CH2) that is exposed to solution. It has been proposed that the ABD initially interacts with actin in a closed conformation using this actin binding region (**Borrego-Diaz *et al.* 2006**). The ABD crystal structures also show the ABS 1 partially buried within the CH1-CH2 interface and a number of residues within the ABS 1 form contacts with the CH2 domain (**Figure 1.5A**). Either a conformational change is required to allow the ABS 1 to interact with actin (**Franzot *et al.* 2005**) or the ABS 1 is not directly involved in interacting with actin and is instead involved in maintaining the overall actin binding domain fold required for initial binding to the actin filament.

1.3.4 Models for the ABD (CH1-CH2) bound to actin filaments

Generating high resolution models of α-actinin bound to actin filaments has been a challenge as the crystallographic structure of filamentous actin has yet to be solved. Therefore, there are no crystallographic structures of the ABD bound to filamentous actin. However, models of the ABD from α-actinin bound to actin filaments have been generated by cryo-EM. In a 3D reconstruction of chicken gizzard α-actinin homodimers cross linking F-actin, the densities attributed to the N-terminal ABD at one end were fit by a closed conformation but the at the other end of the dimer, the densities were consistent with an open conformation of the ABD (**Liu *et al*. 2004, PBD code 1SJJ**). However, the resolution for this model was quite low (20 Å), therefore fitting conformational models to the densities becomes problematic. Another study generated a low-resolution density map of 16 Å of an actin filament (consisting of 10 G-actin subunits) by Cryo-EM, with the CH domains bound to every cleft between actin subunits (**Galkin *et al.* 2010, PDB code 3LUE**). In this case, the densities bound to the actin filament were only large enough for one CH domain. The CH1 domain from the crystal structure of the α-actinin 3 ABD (**PDB code 1WKU**) was fitted to these densities and it was hypothesised that the CH2 domains were unbound and free in solution. However, in generating this data, the actin filaments were saturated with CH domains (one per G-actin subunit). This saturation does not occur in the Z-discs and could be the cause of the unbound CH2 domains, which do not bind due to steric clashes. Fitting the CH1 domain and the CH2 domain in a closed conformation into the extra density

did show steric clashes between the CH2 domain and the actin filaments. This suggests in the final bound state the orientation of the CH1 domain is such that it is unlikely for the CH1-CH2 to be in a closed conformation. In the same study it was also suggested that the role of the CH2 domain is to inhibit CH1, however full length α-actinin ABD (CH1 and CH2) has a higher affinity for actin than the CH1 domain alone (**Way *et al*. 1992**).

EM studies have also been conducted with other members of the spectrin family that have N-terminal CH domain pairs. For the dystrophin ABD1, a large bilobed shaped density bound to the actin has been observed by cryo-EM (**Sutherland-Smith *et al.* 2003**) using a 1:2 ratio of actin to ABD1. This was attributed to an ABD1 dimer bound to the actin filament. A more recent study has reported a 1:1 (ABD1 : actin) stoichiometry, and that the two CH domains remain in a closed conformation when bound to F-actin (**Singh and Mallela 2012**). There has been much controversy over how the ABD of utrophin interacts with filamentous actin. Cryo-EM reconstructions of the ABD with actin over the years have suggested different conformational models. An early reconstruction suggested that utrophin binds to actin via an induced fit mechanism (**Moores *et al.* 2000**). Later reconstructions have indicated both an extended conformation (**Galkin *et al.* 2002**) and a closed compact conformation (**Sutherland-Smith *et al.* 2003**). Recent biochemical analysis of utrophin ABD mutants, thought to be permanently in a closed conformation, showed that there was a dramatic decrease in the binding affinity for actin in the mutant compared to the wild type (**Broderick *et al.* 2012**), supporting the open conformation model. Overall there has been little uniformity between how pairs of CH domains from the spectrin family interact with actin filaments reported by EM studies. This could be because of two reasons; (1) There is no universal way CH1-CH2 domains from different proteins interact with actin filaments and/or (2) the density maps from the EM studies to date have been of a low resolution, therefore the CH1-CH2 conformations fitted to the models are not the conformations *in vivo*. With the development of direct detectors for EM it is now possible to generate higher resolution models, which may better answer how the CH domains of α-actinin and other members of the spectrin family bind actin filaments.

Most recently a high-resolution model for the actin binding domain (two CH domains) from human filamin A bound to phalloidin stabilised actin has been generated (**Iwamoto *et al.* 2018**). In this model a resolution of 3.6 Å has been reported for the actin filament and the CH1 domain. Also, in model the CH2 domain has been resolved

to a lower resolution. The two CH domains can be seen in an open conformation with the CH2 domain unbound to the actin and the lower resolution of the CH2 domain suggests it is mobile. The CH1 domain of filamin A is seen to be inserted in the cleft between actin subunits and three actin binding sites were identified: (1) A short sequence located at the N-terminal end of helix A termed the ABS-N, (2) a short sequence located from the middle of C-E loop to the N-terminal end of termed ABS 2' and (3) a major actin binding site starting from the E-F loop and ending in the middle of helix G termed ABS 2. The previously reported ABS 1 and ABS 3 were found not to interact with actin in this model. Comparison of the protein sequence of human filamin A and α-actinin 2 (**Figure 1.5C**) shows residues at these regions are conserved between the proteins, suggesting the CH 1 domain of α-actinin 2 also interact with filamentous actin in a similar manner. The important actin binding residues identified in the ABS-N of filamin A (L35 and W41) are also present in α-actinin 2 (L30 and W36). The ABS 2' sequence is not highly conserved between α-actinin 2 and filamin A apart from two arginines (R89 an R93 in α-actinin 2). The major actin binding site ABS 2 is highly conserved. One major difference is four residues in helix F. This is interesting as in the EM model of filamin A the helix F is buried in the cleft between the two actin subunits with resides D125 and K127, which α-actinin 2 does not have, forming important contacts with both actin subunits. Within this four-residue region α-actinin 2 has two negatively charged glutamates that filamin A does not have, E120 and E121, which may be involved in interacting with the actin subunits. It is also interesting to note W142 (W135 for α-actinin) on the helix G thought to stabilise the CH1:CH2 interface by interacting with a charge residue (**Figure 1.4F**) also forms hydrophobic contacts with actin in the bound state.

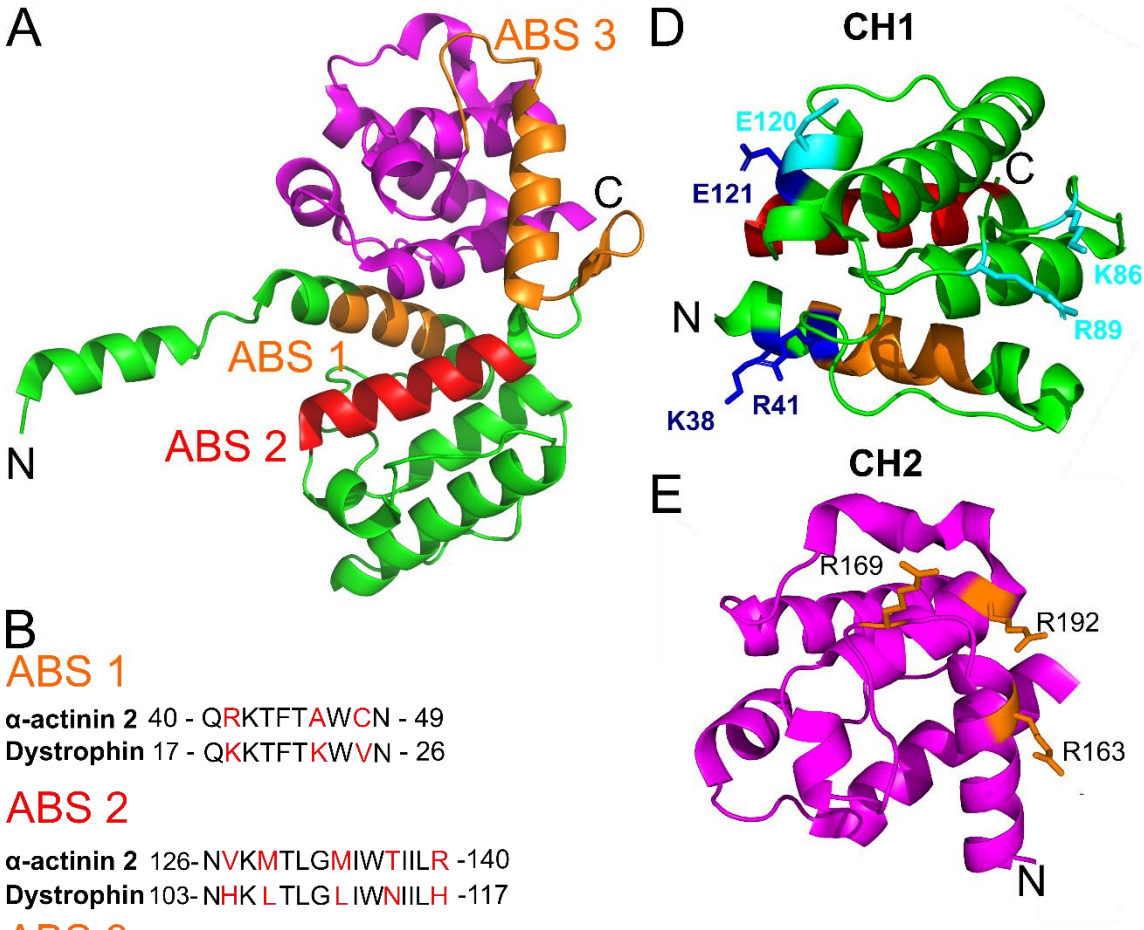

B

ABS 1

α-actinin 2 40 - QRKTFTAWCN - 49
Dystrophin 17 - QKKTFTKWVN - 26

ABS 2

α-actinin 2 126- NVKMTLGMIWTIILR -140
Dystrophin 103- NHK LTLG L IWNIILH -117

ABS 3

α-actinin 2 147- SVEET SAKEGLLL WCQRK TAPYRNVNI -173
Dystrophin 128- MAGLQQTNSEKI LLSWV RQSTRNYPQVNV -156

C

ABS-N

α-actinin 2 30 - LL LDPA WE - 37
Filamin A 35 - LAEDAP WK - 42

ABS 2'

α-actinin 2 86- KP - - DRGKMRF HKI -97
Filamin A 91- RKHNQRPTF RQMQL -104

ABS 2

α-actinin 2 115- VSIGAEEIVDGNLKMTLGMIW -135
Filamin A 122- VSIDSKAIVDGNVKL I LGL IW -142

Figure 1.5 – Actin binding sites located of α-actinin 2.
(**A**) Crystallographic structure of the ABD (residues 19 – 257) from α-actinin 2 (**Haywood *et al.* 2016, PDB code 5A36**) with the proposed actin binding sites (ABS). ABS 1 (orange, residues 40 – 49) located on helix A of the CH1 domain (green). The major actin binding site 2 (red, residues 126 – 140) located on helix G of the CH1 domain (green). ABS 3 (orange, residues 147 – 173) located on helix A of the CH2 domain (magenta). (**B**) Comparison of the amino acid sequences of α-actinin 2 and human dystrophin for each of the actin binding sites. (**C**) Comparison of the amino acid sequences of α-actinin 2 and human filamin A for each of the filamin A actin binding sites – ABS -N, ABS 2' and ABS 2 (**Iwamoto *et al.* 2018**). (**D**) Charged residues on the CH1 domain (green) proposed to form salt bridges with actin subunits (**Shams *et al.* 2016**). At the cleft between two actin subunits, three charged residues interact with one actin subunit (blue) and another three residues interact with the other subunit (cyan). (**E**) Triplet of arginines (orange) on the CH2 domain (magenta) proposed to act as a binding platform for PIP_2.

Molecular dynamic simulations were used to study the chicken smooth muscle α-actinin CH1-CH2 conformation when bound to the actin filament (using the structure generated by **Liu *et al*. 2004**) (**Shams *et al*. 2016**). An overall actin binding mechanism was proposed whereby: (1) in a closed conformation the CH2 domain binds to the actin filament first, (2) the binding to actin induces a conformational change in the ABD from the closed to open conformation, (3) the CH2 domain disassociates from the actin and (4) the CH1 domain migrates to the cleft between two G-actin subunits. It has been hypothesised the CH domains initially bind in a closed conformation as the ABS 1 (on CH1) and ABS 2 (on CH2) (**Figure 1.5A**) together make an actin binding region (**Borrego-Diaz *et al.* 2006**). However, there is no experimental evidence to support the idea that the CH2 domain binds actin first. The dissociation of the CH2 domain from actin in the final bound state is supported by EM models (**Galkin *et al*. 2010, Iwamoto *et al.* 2018**). Overall, there is limited experimental evidence of the mechanism for the CH domain binding actin to support the model proposed by Shams *et al.*

This same study also suggested how CH1 binds the cleft between proximal actin monomers. The CH1 residues K32, R35 and E115 (**Figure 1.5D,** α-actinin 2 equivalent (residues K38, R41 and E121 dark blue)) interact with the actin residues D363, E125 and K118 from one actin monomer. The CH1 residues K80, R83 and E114 (**Figure 1.5D**, α-actinin 2 equivalent (residues K86, R89 and E120 cyan)) interact with the actin residues E364 and R372 from the actin monomer on the other side of the binding cleft. The actin binding residues proposed by molecular dynamic simulation (**Shams *et al.* 2016**) are within or near the actin binding sites proposed for filamin A (ABS-N, ABS 2' and ABS 2) (**Iwamoto *et al.* 2018, Figure 1.5C**), thus suggesting α-actinin binds actin in a similar manner. The residues K86 and R89 (**Figure 1.5D**) are located in the ABS 2' and the filamin equivalent of K86 (R91) has been proposed to be important for actin binding (**Iwamoto *et al.* 2018**). The residues E120 and E121 are located in the helix F situated in the ABS 2 region and are highly likely to directly interact with actin. The α-actinin 2 residues K38 are R41 are located very near to the filamin A ABS -N. A mutant of α-actinin 1 linked to congenital macrothrombocytopenia (CMTP) R46Q, the equivalent to R41 of α-actinin 2, is reported to have an increased affinity to actin (**Murphy *et al.* 2016**). If R41 does form a salt bridge with actin, as suggested by Shams *et al.*, then the mutation to glutamine should decrease the ABD affinity to actin. However, R41/R46 forms a possible salt bridge at the CH1-CH2 interface (**Borrego-Diaz *et al.* 2006**) (**Figure 1.4D**) and the increased affinity can be attributed to the lowering of energy required for transition between the closed and open conformations. Therefore, characterisation of the binding affinity of this mutant alone cannot determine

if R46 directly interacts with actin or not. For the other charged residues not at the CH1-CH2 interface, actin affinity experiments could be used determine if they are important in binding actin.

1.3.5 Regulation of α-actinin in the Z-disc

Models from EM density maps of the Z-disc lattice have shown a regular arrangement of the α-actinin homodimers. *In vitro*, the CH domain from α-actinin can fully decorate the actin filament, which does not occur within the Z-disc (**Galkin *et al.* 2010**). It has been suggested that the Z-repeat (Zr) domains of titin act as a scaffold for the α-actinin molecules in the Z-discs (**Sorimachi *et al.* 1997, Gautel 1996**). The calcium insensitive C-terminal EF 3-4 hand of α-actinin 2 (**Nakayama *et al.* 1994**) has a strong affinity to the Zr 7 domain (Kd ~120 - 190 nM) (**Young and Gautel 2000, Joseph *et al.* 2001**). However, the EF 3-4 hand of α-actinin 2 does not interact with all the Z-repeats with the equal affinity. Z- repeats 1, 3 and 7 bind the EF 3-4 domain with high affinity, whilst Z-repeats 2, 4, 5 and 6 bind weakly (**Joseph *et al.* 2001**). Surface plasmon resonance studies show that the Zq domain of smooth muscle titin has a high affinity to the SR2-SR3 domains of smooth muscle α-actinin (Kd ~ 344 nM) and it was proposed in the same study to interact with the same α-actinin bound to the Zr7 domain between the SR2 and SR3 domains (**Chi *et al*. 2008**).

The structure of EF 3-4 from α-actinin 2 in complex with the Z-repeat of titin (Zr 7) was solved by NMR (**Atkinson *et al.* 2001, PDB code 1H8B**). The more recent crystal structure of the α-actinin 2 homodimer (**Ribeiro *et al.* 2014**) showed that the EF 3-4 of one monomer interacts with the ABD- spectrin repeat 1 alpha helical linker region of the opposing monomer further. This interaction is very similar to the Zr7- EF 3-4 complex (**Atkinson *et al.* 2001**) whereby the α-helix linker region inserts into the EF hand and interacts mainly via a 1-4-5-8 hydrophobic binding motif (**Ribeiro *et al.* 2014**). It has been suggested the α-actinin 2 homodimer auto-inhibits the interaction between the EF 3-4 domain and Z-repeats repeat domains of titin. The capacity for the EF 3-4 hand to bind the Z-repeats of titin is thought to be regulated by the the phosphoinositide, PtdIns(4,5)P_2 (PIP_2), which is present within the Z-disc (**Fukami *et al.* 1992**) and can bind to the CH2 domain (residues 168 – 184) of α-actinin in chicken striated muscle (**Fukami *et al.* 1996**). It has been suggested that the binding site for the negatively charged head of PIP_2 in α-actinin 2 and 3 is a triplet of arginine residues on the CH2 domain (**Figure 1.5E**) (**Franzot *et al.* 2005, Ribeiro *et al.* 2014**). The mechanism by which PIP_2 regulates the binding of α-actinins to titin in the Z-discs is still unclear. A model has been proposed whereby upon PIP_2 binding to the CH2

domain, the fatty acid chain of PIP_2 disrupts the interaction between the EF 3-4 domain and the linker region, freeing EF 3-4 to bind the Z-repeats (**Ribeiro *et al.* 2014**). However, this model has yet to be proven experimentally. It is also thought that the binding affinity of α-actinin to actin increases in the presence of PIP_2, however the increase in binding affinity has yet to be quantified. The addition of PIP_2 to a solution containing actin filaments and α-actinin 2 has shown an increased gelation suggesting PIP_2 increases the affinity of muscle α-actinin to actin (**Fukami *et al.* 1992**), however this has not been investigated further.

1.4 Mutations in α-actinin linked to disease

1.4.1 Identification of disease-causing mutations

Mutations in the α-actinin genes (isoforms 1, 2 and 4) have been identified in individuals with a number of different genetic diseases by genome sequence analysis. These mutations maybe the cause or a contribution to the manifestation of the diseases by changing the properties of the α-actinins. Twenty mutations within the non-muscle α-actinin 1 gene sequence have currently been identified in individuals with a group of disorders called congenital macrothrombocytopenia (CMTP) (**Nakayama *et al.* 2013, Gueguen *et al.* 2013, Yasutomi *et al.* 2016, Westbury *et al.* 2015, Kunishima *et al.* 2013, Bottega *et al.* 2015**). CMTP is characterised by both abnormally large platelets and a reduced platelet count (**Kunishima and Siato 2006**). Twelve mutations in the non-muscle α-actinin 4 gene have also been found in individuals with focal segmental glomerulosclerosis (FSGS), a kidney disease (**Choi *et al.* 2008, Safarikova *et al.* 2013, Barua *et al.* 2013, Weins *et al.* 2005, Feng *et al.* 2016, Buscher *et al.* 2018**). The disease is defined as sclerosis in the glomerulus region of the kidney (**Jefferson and Shankland 2014**). The mutations associated with CMTP and FSGS are located throughout the amino acid sequence of α-actinin 1 and 4 respectively. However, most of the mutations are situated in the N-terminal actin binding domain and the C-terminal EF 1-2 hands. There are no mutations within muscle α-actinin 3 associated to any types of myopathy, however there is a premature stop codon producing a R577X α-actinin 3 variant (**North *et al.* 1999**).

For muscle α-actinin 2, nine point mutations have been identified in individuals with cardiomyopathy (**Theis *et al.* 2006 ref, Chiu *et al.* 2010 refed, Girolami *et al.* 2011**). Cardiomyopathy is a characterised by irregularity in the heart muscle. There are two types of this disease; hypertrophic cardiomyopathy (HCM) and dilated cardiomyopathy (DCM). HCM is characterised by ventricle wall thickening of the left ventricle wall, and DCM is characterised by a thinning of the ventricle wall. The point mutations are

located throughout the α-actinin 2 sequence. Four mutations are present in the N-terminal ABD; Q9R, G111V, A119T and M228T and therefore may alter the ABD:actin interaction. Three mutations, T495M, E583A and E628G, are present in the rod domain. The two negatively charged glutamates, which are mutated to small hydrophobic residues, may play a part in disrupting the binding of other Z-disc proteins. Two mutations linked to HCM (R795T) and DCM (H775Y) are located near each other on EF1-2 of the C-terminal CAM-like domain. It is unclear at this point why one mutation causes HCM whilst the other causes DCM. The mechanisms causing both HCM and DCM are currently not known, and it is unclear why some mutations cause the HCM phenotype and others the DCM phenotype.

1.4.2 Mutation in the actin binding domain causing disease

α-actinins have a major role as actin filament crosslinking proteins integral to actin cytoskeletal networks, such as the Z-disc lattice. Many of the mutations linked to HCM, FSGS and CTMP are regularly found in the actin binding domain (across isoforms 1, 2 and 4) (**Figure 1.6A**). Therefore, many studies have focused on how α-actinin function is altered by the ABD mutations. For CTMP α-actinin 1 mutants, HeLa cells were transfected with the mutant (Q32K, R46Q, V105I and E225K) to determine how the actin filament network and α-actinin localisation compared to non-transfected cells by immuno-fluorescence microscopy (**Murphy *et al.* 2016**). No distinguishable differences between α-actinin 1 mutant transfected cells and transfected cells were observed. Western blot analysis did however show that there were more mutant α-actinins present in the cytoplasm compared to wild type. Either there are only subtle changes in the actin cytoskeleton and α-actinin 1 localisation or there are other factors in play, for example the stability of α-actinin 1 or the disruption of a different binding partner. For FSGS α-actinin 4 ABD mutants, the mis-localisation of α-actinin 4 with the individual mutations W59R, I149del, K255E, T259I and S262P has been reported in podocytes (usually to a small region just outside the nuclei) (**Weins *et al.* 2005**). Also, the α-actinin 4 K255E mutant has been shown to cause an increase actin aggregation in lung fibroblasts (expressing the mutant) and forms disordered network actin filaments networks *in vitro* (**Weins *et al.* 2007**). The point mutations in muscle α-actinin 2, G111V and A119T, associated with HCM have been shown to cause delocalisation of α-actinins to the outside of the Z-disc regions and increased α-actinin aggregation in cardiomyocytes.

In vitro studies of different α-actinin ABD mutant constructs, from α-actinin 1, 2 and 4, with filamentous actin have shown that there the mutations tend to increase the affinity

of the ABD for filamentous actin. With this in mind the mutations currently identified have been mapped out here on the ABD of α-actinin 2 (**PDB code 5A36**) (**Figure 1.6B**), to evaluate common positions of the mutated residues and indicate important actin binding regions. It is clear the majority of mutated residues are located at the interface between the CH1 and CH2 domains (**Figure 1.6C**). There is a run of four mutated residues, associated to FSGS (α-actinin 4), along the length of the G-helix of the CH2 domain, (K225E, T259I, S262P/F and Y265H). Different ABD constructs with separate mutations (K225E, T259I, S262P) have been found to have a higher affinity to actin compared to the wild-type (Kd = 25 – 35 μM, Kd of the WT not determined) (**Lee *et al.* 2008**). The exact affinity of these mutants to actin is uncertain as another study reported a ~ 6 fold increase in binding affinity to F-actin from an ABD K255E construct (residues 1-271) (Kd ~ 5 μM) compared to wild-type (Kd ~ 32 μM) (**Weins *et al.* 2007**). However, both studies demonstrated that the binding affinity of ABD K255E for F-actin was greater than the wild-type. Increased bundling of actin by full length α-actinin 4 with the Y265H mutation *in vitro*, has also been reported (**Feng *et al.* 2016**). The K255 residue is thought to be part of an important interaction with W147 at the CH1-CH2 interface (**Borrego-Diaz *et al.* 2006**)**.** The crystal structure of the ABD of α-actinin 4 K255E shows it to be in a closed conformation and analytical ultra-centrifugation suggests the ABD constructs with the mutations K225E, T259I, S262P are in closed conformations when free in solution (**Lee *et al.* 2008)**. Although the mutations do not change the ABD conformation, it is hypothesised they weaken the interaction between CH1 and CH2 so that the energy required for the transition from closed to open conformations is lowered, thus, increasing the affinity to actin (**Lee *et al.* 2008**).

This mechanism is supported by molecular dynamic simulations of the ABD from chicken smooth muscle α-actinin (**Shams *et al.* 2016**). The simulations of the K255E equivalent mutation in chicken smooth muscle α-actinin (K237E) indicated that this mutation reduces the force required to separate the CH domains. Also, the average interaction energy with F-actin was less for the mutant compared to the wild-type. This indicates that the increase in binding affinity observed is not through direct interactions with the actin filament (**Weins *et al.* 2007**, **Lee *et al.* 2008**). It is also interesting to note that the α-actinin 4 ABD K255E mutation together with two other mutations Q52A and T55A, had a reduced affinity to actin (Kd ~ 33 μM) compared to the ABD construct with K255E mutation alone (Kd ~ 5 μM) (**Weins *et al.* 2007**). The residues Q52 and T55 (helix G, CH1) are also involved in interactions at the CH-CH2 interface, therefore the mutations should further reduce the energy required for the transition from the closed state to the open state. However, a reduction in binding affinity to F-actin was

observed. One possible explanation for this is the residues Q52 and T55 lie in one of the actin binding sites (ABS 1) and so are directly involved in binding F-actin. Another is that the conformation of the ABD with the triple mutation favours an open conformation not a closed conformation. It has been proposed that the CH2 domain initially binds the actin filament with the ABD in a closed conformation (**Shams *et al.* 2016, Borrego-Diaz *et al.* 2006**), therefore the mutations may disrupt the ABD conformation required for preferential initial binding. However, there is no evidence that the ABD mutant construct (K255E, Q52A and T55A) is in an open conformation and the affinity of the mutant construct observed was very similar to the wild-type.

Along helix A of CH1 there are three mutated residues linked CMTP; Q32K, F37C, R46Q/W and one linked to FSGS; W59R. (**Figure 1.6C**) The ABD of α-actinin 4 with the W59R mutation has been shown have an increased affinity to F-actin, similar to the K255E mutant (**Weins *et al.* 2005**). The mutant R46Q had a marked increase in affinity (Kd = ~0.7 μM) compared to the wild-type (**Murphy *et al.* 2016**). The crystallographic structures of α-actinin ABDs show the Q32 and R46 sidechains form contacts with the CH2 domain, therefore the mutations would disrupt these interactions. It should be noted that the uncharacterised mutation F37C is present in the proposed actin binding site 1, however it is part of the KTFT motif which has been shown to be not important in F-actin binding (**Corrado *et al.* 1994**). It can be hypothesised that the mutations on the α-helices A (CH1) and G (CH2) weaken the CH1-CH2 interface, thereby increasing affinity to F-actin. The HCM linked mutated residue M228 is also situated at this interface suggesting that the M228T mutation may also have an increased binding affinity to F-actin.

There are mutations linked to disease which are not located at the interface and therefore highlights regions on the ABD which may directly bind actin. The α-actinin 4 mutations I149del and F153L are both within actin binding site 2 (helix G, **Figure 1.6C**) and the I149del ABD construct has an increased affinity for F-actin (**Weins *et al.* 2005**). Why the deletion of this hydrophobic residue increases actin affinity is unclear. For α-actinin 1 CMPT linked mutations, there are two mutations found on the F helix of CH2; E225K and V228I which may be involved in binding actin. The mutation E225K on α-actinin 1 also has an increased affinity to actin (**Murphy *et al.* 2016**).

The α-actinin 2 HCM mutation A119T is located on the F helix of CH1 (**Figure 1.6D**) and it has been hypothesised this helix is buried in the cleft between adjacent G-actin subunits with E120 and E121 both forming salt bridges with the different actin subunits (**Shams *et al.* 2016**). The G111V mutation is located on the loop between helices E

and F (**Figure 1.6D**). The α-actinin 1 CMPT mutation V105I has been shown to increase binding affinity to actin (**Murphy *et al.* 2016**). The α-actinin 2 V105 equivalent residue (V112) is next to G111, this suggests this region is important for actin binding.

A

Isoform 2 mutations	Residues in Isoform 2
G111V	
A119T	
M228T	
Isoform 4 mutations	
W59R	W47
E72Q	E60
I149del	I137
F153L	F149
K255E	R243
T259I	T247
S262P/F	S250
Y265H	Y253
Isoform 1 mutations	
D22N	D29
Q32K	Q39
F37C	F44
R46Q/W	R53
Q51E	Q58
V105I	V112
E225K	E232
V228I	V235

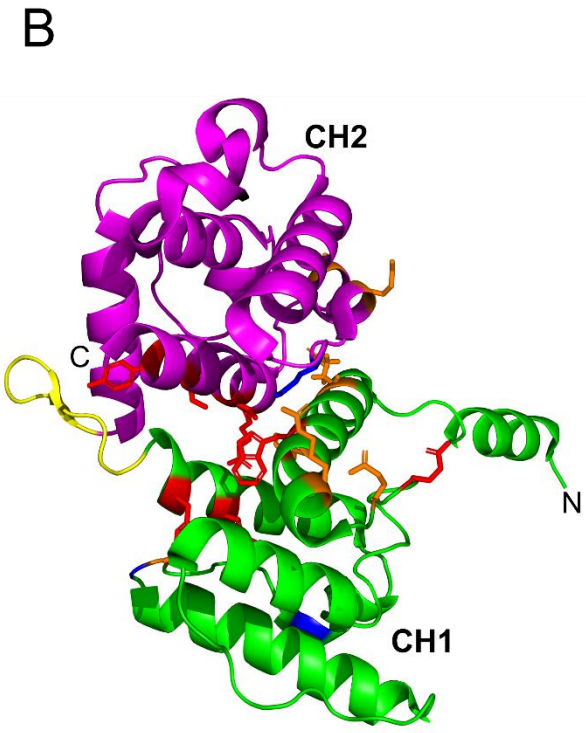

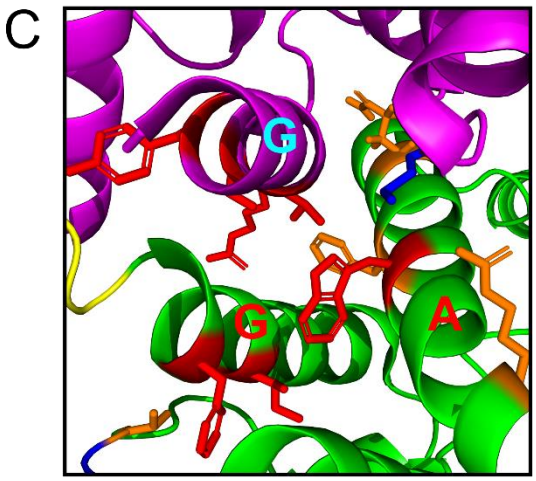

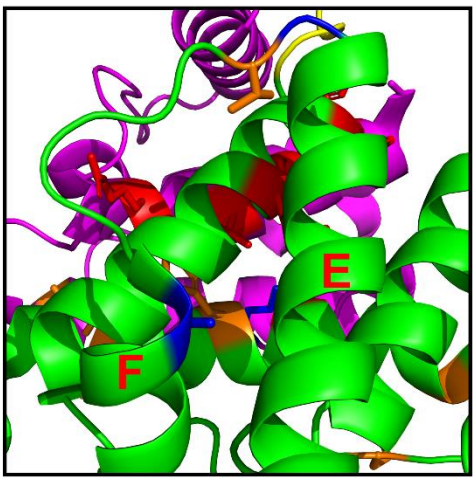

Figure 1.6 – Mutations associated with disease located on the ABD of α-actinin. (**A**) Mutations thought to be associated with CMTP, HCM and FSGS for isoforms 1, 2 and 4. The equivalent residues for isoforms 2 are shown. (**B**) ABD from α-actinin 2 (PDB code 5A36, CH1 (green) and CH2 (magenta)) showing the location of each mutated residue from α-actinin 2 (blue), 1 (orange) and 4 (red). (**C**) Close up of the interface between CH1 and CH2. (**D**) Close up of helix E and F.

Chapter 2 - General methods and materials

2.1 Chemicals

All chemicals and materials used during this project were supplied by Sigma, unless otherwise stated.

2.2 Sterilising Media

For expression of proteins, all lysogeny broth (LB) and LB AGAR was autoclaved before use. All buffers used in protein purification were filtered sterilized using a 45 µm filter (Milipore).

2.3 Escherichia coli strains

For plasmid generation NEB 5α cells were used and are deficient in endA proteases and resistant to phage T1. For expression of proteins BL21(DE3) cells were used (NEB). BL21(DE3) is a standard T7 expression strain that is deficient in Lon and OmpT proteases and resistant to phage T1.

2.4 Transformations

All *E. coli* strains used were chemically competent and therefore the introduction of vectors into *E. coli* cells was done via heat shock transformations. The transformation protocol used was as follows. In a 1.5 mL eppendorff, 1 µL of plasmid was added to 10 – 20 µL of *E.coli* stock from NEB and left on ice for 20 mins. The plasmid and cell mixture was then incubated at 42 ºC for 30 secs. The mixture was left on ice for a further 30 mins for recovery of the cells. 200 µL of SOC media was added to the cells and both were incubated at 37 ºC for 1 hr at 200 rpm, for cell culture growth. The transformed cells were spread onto petri dishes with LB-agar with the appropriate antibiotic (kanamycin 34 µg mL^{-1} or ampicillin 100 µg mL^{-1}). The plates were incubated overnight at 37 °C.

2.5 Molecular Biology

2.5.1 Plasmids

All plasmids used during this project can be found in **Table 1** and the vector maps can be seen in **Figure 2.1**.

2.5.2 Single Stranded DNA Primers

DNA primers (**Table 2**) for PCR and sequencing were designed using Primer3Plus web-based tool and primers for site directed mutagenesis were designed by PimerX web-based tool. All primers were ordered from Integrated DNA Technologies (IDT). All primers were made up to a 100 µM stock in dH_20 and stored at -20 ºC.

2.5.3 Polymerase chain reaction (PCR)

A Bio-Rad T100™ Thermal Cycler was used for the PCRs. A typical PCR had the following mixture, made up in a PCR tube: 10 µL 5x Phusion High Fidelity (HF) buffer, 1 µL dNTP (a mixture of deoxynucleotides is required in the polymerase reaction) (10 mM stock), 1 µL forward primer (10 µM stock), 1 µL reverse primer (10 µM), 1 µL template vector, 1 µL Phusion® HF DNA Polymerase (NEB, 2 units μL^{-1}), 1.5 µL DMSO (optional) and dH_20 to make the final volume 50 µL. After the PCR the products were ran on an agarose gel to verify the PCR had worked followed by gel extraction.

2.5.4 DNA Gel extraction and Plasmid purification (mini-preps)

A Qiagen gel extraction kit (28704) was used for the extraction of DNA after agarose gel electrophoresis. The manufacture's protocol was followed. First the DNA bands were excised from the gel. Then a 4x volume of agarose solubilisation buffer was added to the excised gel and heated to 50 ºC for 10 mins. The DNA in the media was applied to a silica membrane column and briefly centrifuged (17,000 xg) so the media passed through the membrane. After which the membrane was washed with 700 µL high salt buffer followed by 750 µL high ethanol media to remove the salt from the membrane. The DNA was eluted off the membrane in 50 µL of dH_2O.

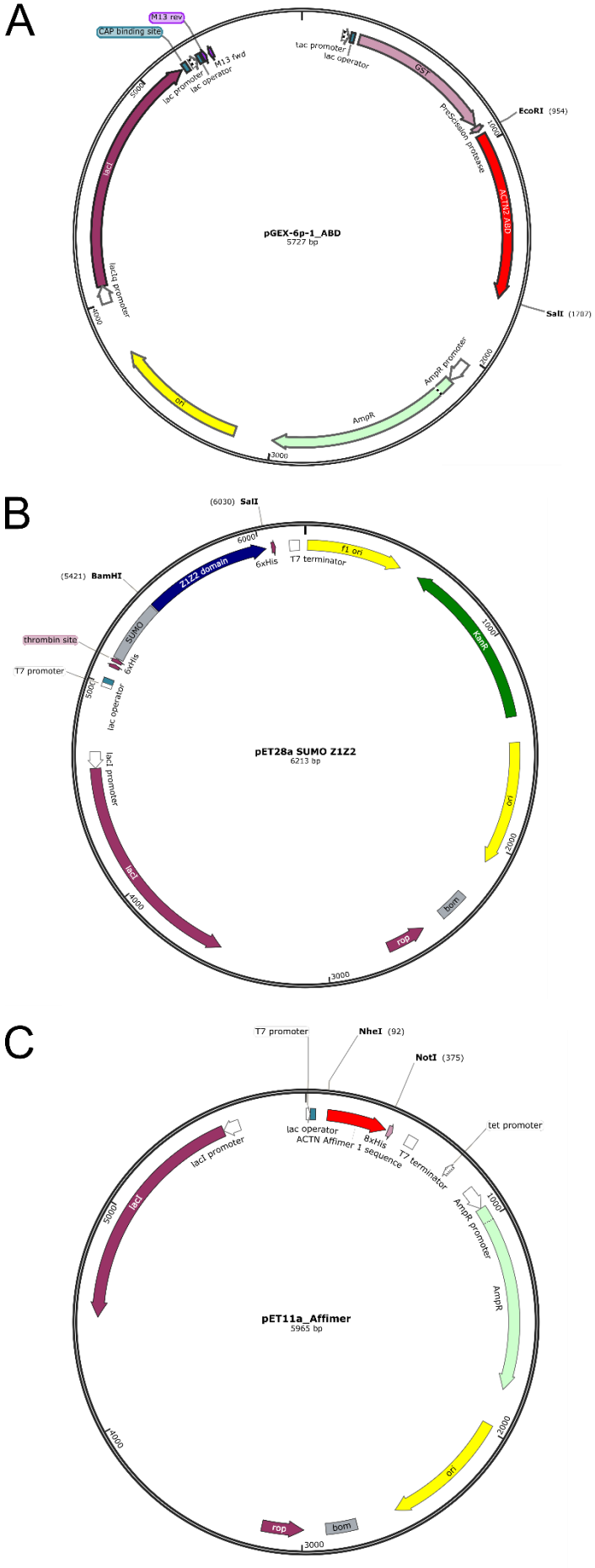

Figure 2.1- Vector maps. (**A**) Expression vector pGEX-6p-1 with the DNA sequence for the actin binding domain of human α-actinin 2 between the restriction sites EcoRI and SalI. (**B**) Expression vector pET28a-SUMO with the DNA sequence for the N-terminal domains of mouse titin Z1Z2 between the restriction sites BamHI and SalI. (**C**) Expression vector pET11a with the Affimer DNA sequence between the restriction sites NheI an NotI.

Qiagen miniprep kits (27104) were used for the purification of plasmids. Qiagen miniprep kits use alkaline/SDS conditions for cell lysis and silica membranes to isolate the plasmid DNA in high salt conditions. 5 mL cultures of NEB 5α cells were grown overnight at 37 ºC, 200 rpm. The cells were then pelleted by centrifugation (3000 xg, 20 mins, at 4 ºC). The LB was removed and resuspended in 250 µL resuspension buffer with RNase A. 250 µL of lysis buffer was then added, mixed and incubated at room temperature for 5 mins. After incubation of the lysis buffer 350 µL of neutralisation/ high salt buffer was added and mixed thoroughly. The lysate was centrifuged at room temperature (17,000 xg) for 10 mins and the lysate was removed from the precipitate. The lysate was applied to a column with a silica membrane and the column was centrifuged for 1 min at 17,000 xg. The membrane was then washed with 900 µL of a high salt buffer followed by a high ethanol wash to remove the salt. The column was further centrifuged for 5 mins at 17,000 xg to remove any excess ethanol on the silica membrane. The DNA was eluted off the column in 50 µL dH_2O.

2.5.5 Digestion of DNA by Endonuclease restriction enzymes

High-Fidelity (HF®) restriction enzymes (NEB) were used to cut vectors and DNA inserts at specific restriction sites. In a double endonuclease restriction digest, 1 µg of DNA vector was digested using 0.5 µL of each restriction enzyme in CutSmart buffer (NEB) (2 µL of 10x stock) in a volume of 20 µL made up with dH_2O, at a temperature of 37 ºC for 1-2 hour.

2.5.6 Agarose Gel electrophoresis

Agarose gel electrophoresis is used to separate DNA fragments of different sizes within a sample. 10 µL of 6x purple loading dye (NEB) was added to 50 µL DNA samples before electrophoresis to access the DNA movement through the gel during electrophoresis. A 30 µL DNA sample was loaded into an individual well of a 1 % agarose gel (1 g agarose in 100 mL TAE buffer with 1 µL Invitrogen™ SYBR™ Safe DNA Gel Stain (10,000x stock)). SYBR™ Safe was used to visualize the DNA bands in the gel. The gels were immersed in TAE buffer (1x) in a Mini-Sub® cell GT (BioRad) and the gel was ran at 100 V for typically 40 mins. The gels were imaged in a ChemiDoc XRS+ (BioRad). If DNA bands in the gel needed to be purified they were cut out using a sterile scalpel and then a gel extraction kit (Qiagen) was used to purify the DNA (manufacture protocol was followed).

2.5.7 Ligations

In this work ligations were used to insert Affimer DNA sequences into empty pET11a vectors. In a ligation reaction the following was added: 75 ng linear pET11a, 25 ng of Affimer DNA insert, 2 µL 10x T4 ligase reaction buffer, 1 µL T4 ligase (NEB, 400 units μL^{-1}) and dH_2O to make up to a final volume of 20 µL. The ligation mixture was incubated at room temperature for 1 hr. 1 µL of the ligation mixture was then used for transformation into NEB 5α cells. The subsequent colonies growing on the LB-agar plates the next day were picked to grow in 5 mL starter cultures. The starter cultures were used for minipreps and the resulting purified plasmids were sent for sequencing the verifying the ligations were successful.

2.5.8 Measuring dsDNA concentrations

The absorbance at 260 nm of dsDNA can be measured using a spectrophotometer. dH_2O was used as a blank. A Nano Photometer® NP80 (IMPLEN) as used with 1-2 µL of the dsDNA sample. Measuring the A_{260} can be used to calculate the dsDNA concentration:

When A_{260} =1.0, there is 50 µg mL^{-1} of dsDNA present in the sample.

2.5.9 Sequencing

Sequencing data was used to verify that the correct DNA sequence is in the vector with no mutations and was in frame. Purified plasmid samples were sent to GATC Biotech. Typically, uninterrupted 600 bp reads were common for one sequencing dataset. Therefore, longer constructs needed more than one reaction. Sequencing primers for the full length α-actinin 2 gene were designed using Primer3Plus. For sequencing of Affimer constructs in pET11a the T7 forward primer was used.

2.6 Protein expression

All protein constructs (**Table 3**) were expressed in BL21(DE3) cells (NEB). The cells were typically grown in a 2 L incubation flask using 400 mL of lysogeny broth (LB) with either kanamycin 34 µg mL^{-1} or ampicillin 100 µg mL^{-1} depending on the plasmid present in the *E.coli* culture grown (**Table 1**). 200 mL of LB was used for Affimer expression. The freshly autoclaved LB with antibiotic was inoculated with a 10 mL starter culture of the cells. Stater cultures were prepared by picking a fresh colony and using the colony to inoculate 10 mL of fresh LB (with the appropriate antibiotic) then incubating the culture overnight (37 ºC, 220 rpm). The 400 mL cultures were incubated at 37 °C, 220 rpm for typically 2-3 hours until the OD_{600} reached 0.6 (measured using a

CARY 50 BIO (Varian) spectrophotometer). Protein expression was induced using IPTG. The concentration of IPTG used and the incubation temperature / time used depended on the protein expressed (**Table 4**).

2.7 Lysis of BL21(DE3) cells

After expression the cells were pelleted by centrifugation (3,000 xg, 4 °C, 30 mins) in a Thermo scientific Hercaeus Megefuge 16R. The cells were then re-suspended in the appropriate lysis buffer. Cells were lysed by sonication, 10 secs on and off, six times at 40% amplitude using a Vibra-cell™ (Sonics) sonicator. Before purification of the proteins the lysates were centrifuged to remove cell debris. Lysates were centrifuged (30,000 xg, 4 ºC, 45mins) using a Beckman Avanti J series centrifuge with a JA 25.50 rotor.

2.8 Determining protein sample concentrations and quality

2.8.1 Measuring protein concentration

Protein sample concentrations were calculated using the Beer-Lambert law:

$A_{wavelength}$ = Concentration (M) x path length (cm) x extinction coefficient (M^{-1} cm^{-1})

The absorbance at 280 nm of a protein was measured using a spectrophotometer. The buffer the protein sample is in is used as a blank for the spectrophotometery. For small volume protein samples (1-2 µL), a Nano Photometer® NP80 (IMPLEN) as used. With larger protein samples (at least 500 µL) a CARY 50 BIO (Varian) was used. The extinction coefficient can be calculated using the protein sequence:

Extinction Coefficient of a protein (at A_{280}) = (5500 x n(Trp)) + (1490 x n(Tyr)) + (125 n(Cys))

2.8.2 Sodium dodecyl sulfate polyacrylamide gel electrophoresis (SDS PAGE)

An SDS PAGE was used to assess the MW of a given protein and to assess the purity of a sample. Unless otherwise stated all equipment used for a SDS PAGE was ordered from BioRad. 2x Laemmli sample buffer was added to a protein sample (1:1) ratio which was then heated to 100 °C for 5 mins. 1x Laemmli buffer contains 0.125 M Tris-HCl pH 6.8, 30% sucrose, 0.04 % bromophenol blue, 2% SDS, 5 % β mercaptoethanol. Heating the sample results in fully denatured proteins with SDS bound, giving all the proteins a negative charge. Gels used during the project were either Mini-PROTEAN® TGX™ Precast 4-20 % acrylamide/Bis-acrylamide gels or lab made 1 mm 12 %

acrylamide/Bis-acrylamide gels using a Mini-PROTEAN® Tetra handcast systems. The gels were run in a Mini-PROTEAN® Tetra Cell System, immersed in 1x Glycine Tris SDS running buffer (Severn Biotech Ltd.) at constant voltage (200 V) for ~ 45 mins. The gels were stained with Quick Blue stain (TripleRed) for 1 hr at room temperature on a rocker and washed with dH_2O. The stained gels were imaged using a BioRad ChemiDoc XRS+.

2.8.3 Freezing protein samples for long term storage

During the project protein samples were regularly frozen and either stored in an -80 °C freezer or in a liquid nitrogen dewar for long term storage. To minimize the damage of the protein samples during freezing, the samples were either frozen in liquid nitrogen or in an ethanol/dry ice bath. The samples were either pipetted drop-by-drop into liquid nitrogen or aliquoted into eppendorf tubes (30 µL maximum), and then frozen. Also, to minimize damage during thawing of the samples, they were thawed quickly in hand.

2.9 Preparation of rat cardiomyocytes for staining

Cardiomyocytes (CDM) were isolated by Dr. Ruth Hughes from heart muscle of adult male Wistar rats. The CDMs were collected in Tyrodes buffer, which was exchanged for cardiomyocyte media (M199 media, Gibco, supplemented with 5 mM creatine, 5 mM taurine, 2 mM Na pyruvate, 2 mM L-carnitine, 0.1 µM insulin, 250 µg normocin, 40 µM cytochalasin D) before the cells were seeded onto the coverslips. CDMs were incubated on either clean 13 mm glass coverslips or larger 25 mm coverslips (for dSTORM imaging) covered in laminin, for 2 hrs at 37˚C to allow for cell attachment. The CDMs were then fixed in 2 % PFA for 20 mins and stored at 4 °C until use.

2.10 Microscopes

For deconvolution microscopy, the cells were imaged using a DeltaVision Microscope (GE Healthcare Life Sciences) using the x100 oil objective. The dSTORM system used was built in-house by Dr. Alistair Curd and had the following specifications (as described in **Tiede *et al.* 2016**): an inverted microscope (Olympus, IX81) with a 60x, 1.2 NA, water-immersion objective lens (Olympus, UPLSAPO60XW), and a cylindrical lens with f = 150 mm (Thorlabs, LJ1629RM-A) for generating astigmatism. Lasers at 642 nm and 405 nm (Omicron, LuxX) provided widefield excitation and photo-activation of Alexa Fluor 647, together with a 2x beam expander before the rear illumination port of the microscope. Images were captured by a back-thinned, electron-multiplying CCD camera (EMCCD), cooled to - 80 °C (Andor Technology, iXON Ultra), using published scripts (**York *et al.* 2011**) called from the camera interface (Andor Technology, SOLIS).

2.11 Methods Tables

Table 1- Plasmids

Plasmids	Purpose	Size /bp	Fusion tag present in vector	Antibiotic resistance
pET28a_SUMO	Protein expression in E. coli	5633	N-terminal 6x HisTag-SUMO	Kanamycin
pGEX-6p-1	Protein expression in E. coli	4984	N-terminal GST	Ampicilin
pET-11a	Protein expression in E. coli	6013	C-terminal 8xHisTag	Ampicilin

Table 2 – DNA primers

Primer name	Forward Primer	Reverse Primer	Comments
SDM M228T ACTN2	5'- CTGGATATTCCTAAAA**C**GTTGGATGCTGAAGAC -3'	5'- GTCTTCAGCATCCAAC**G**TTTTAGGAATATCCAG -3'	Site directed mutagensis primers for the α-actinin 2 mutation M228T The red nucleotide indicates the point mutation t683c
Affimer_pET11a	5'- ATGGCTAGCAACTCCCTGGAAATCGAAG -3'	5'- TACCCTAGTGGTGATGATGGTGATGC -3' 5'- TTACTAATGCGGCCGCACAAGCGTCACCAACCGGTTTG -3'	Primers used to sub-clone Affimer constructs into pET11a Reverse primer used to introduce a cysteine at the C-terminal end
2347 Seq ACTN2	5'- GTAGATCCCAACGGGCAAG -3'	-	Sequencing primer for α-actinin 2 gene starting at bp 2374
1759 Seq ACTN2	5'- GATGAGCTCCGGACCAAGT -3'	-	Sequencing primer for α-actinin 2 gene starting at bp 1759
1148 Seq ACTN2	5'- ACCTGGCTGAGAAGTTCAGG -3'	-	Sequencing primer for α-actinin 2 gene starting at bp 1148
649 Seq ACTN2	-	5'- CGATGTCTTCAGCATCCAAC -3'	Sequencing primer for α-actinin 2 gene starting at bp 649

Table 3 – Protein DNA sequences and their expression vectors

Construct	Organism	DNA sequence size /bp	Codon optimised for E. coli expression	Plasmid	Restriction sites
Z1/Z2 domain of titin	Mouse	603	Yes	pET28a-SUMO	BamHI and SalI
ABD of α-actinin 2	Human	747	No	pGEX-6p-1	EcoRI and SalI
Affimers	Plant consenusus sequence	276	Yes	pET11a	NheI and NotI

Table 4 – Expression conditions for the different protein constructs.

Protein	Protein size /kDa	IPTG /mM	Expression temperature /°C	Expression time
Z1/Z2 domain of titin	21.3	1	37	3 hours
ABD of α-actinin	28.6	0.5	37	3 hours
Affimers	12.5	0.1	25	6 hours

Chapter 3 - Generating and characterising Z-disc protein binding Affimers

3.1 Introduction

How Z-disc proteins localise within cardiomyocytes and other striated muscle cells has been incredibly difficult to study as the Z-disc regions are densely packed with different proteins and are very narrow, between 100 -140 nm in cardiomyocytes and slow striated muscle (**Luther *et al.* 2003**). Conventional fluorescence microscopy techniques give the spatial resolution of ~ 250 nm. Therefore, fluorescence microscopy can currently be used to identify proteins that localise to the Z-disc however, with the limited resolution, it cannot be used to study the organisation of proteins within Z-discs. With the development of super-resolution techniques, it is now possible to study Z-disc protein organisation using fluorescence microscopy.

The super-resolution technique direct Stochastic Optical Reconstruction Microscopy (dSTORM) uses binders directly linked to commercial fluorescent dyes to label specific proteins within the cell for imaging (**Heilemann *et al.* 2008, *van* de Linde *et al.* 2011**). Antibodies have been widely used as binder for conventional fluorescent techniques. Following on from this, antibodies are widely used for dSTORM however, with the improved spatial resolution dSTORM offers (~ 20 nm in the x,y plane and ~ 50 nm in z (***van* de Linde *et al.* 2011**)), antibodies are not the best binders for this technique. Antibodies are large (~ 10 nm in length) therefore there is a large distance between the fluorescent reporter dye and the target, a “linkage error” and they have trouble penetrating dense networks within the cell, such as the Z-discs. Also, producing antibodies is generally a lengthy and costly pursuit. More recently smaller antibodies variants such as the single chain camelid antibodies (nanobodies) have been used for fluorescence microscopy (**Ries *et al.* 2012**), which reduce this linkage error from ~10 nm to ~2 nm. However, like antibodies nanobodies can be time consuming and costly to generate.

Twenty different small scaffold proteins unrelated to antibodies have been developed for research and medical applications with the aim of being cheaper and reliable alternatives to antibodies (**Škrlec *et al.* 2015**). Popular non-antibody binding proteins include DARPins, Monobodies, Affibodies, Anticalin, Affimer type I and Affimer type II. All of which are developed from proteins or protein domains chosen for their stability, small size and easy recombinant expression (**Bedford *et al.* 2017**). The scaffold structure of Affimers (type II) is the consensus sequence of plant phytosystatins, has

no cysteines in the sequence and is highly thermostable (T_m = 101 ºC) (**Tiede *et al*. 2014, Tiede *et al*. 2017**). Each Affimer generated to bind a specific protein target has two unique binding loops (8 - 9 residues in length). Affimer sequences for binding specific proteins are quick and inexpensive to obtained by screening an Affimer phage library against a purified protein target by a phage display assay. Affimers are easily expressible in *E. coli* therefore they are also quick and inexpensive to make using common laboratory equipment and reagents.

Affimers are highly suitable for use as binders for dSTORM. They are small (~ 12.5 kDa) and therefore have a small linkage error (~ 2 - 3 nm). Also, a single cysteine can be inserted at the C-terminal end of the Affimer sequence to allow a single fluorescent dye molecule to be attached per Affimer molecule. Having the reporter dye molecule directly linked to the Affimer reduces the linkage error, compared to the introduction of a secondary Affimer binder with the reporter dye attached for example, using biotinylated Affimers followed by streptavidin conjugated to the reporter dye. Also having one dye molecule conjugated to one Affimer allows for more precise localisation of the Affimers in dSTORM. These small binders have already been shown to work well as binders for fluorescence microscopy techniques. Actin binding Affimers directly linked to commercial dyes have been shown to label actin filaments in Hela cells as well as phalloidin and actin antibodies (**Lopata *et al*. 2018**). Also, actin binding Affimers conjugated to a docking DNA strand have been used to image actin filaments in Cos7 cells by DNA-PAINT imaging (**Schlichthaerle *et al.* 2018**). Tubulin binding Affimers have also been used image microtubules by dSTORM (**Tiede *et al*. 2017**).

The aim of the research discussed in this chapter was to isolate and characterise Affimers that bind to Z-disc proteins, for their suitability in dSTORM. To achieve this, purified actin-binding domain (ABD) of human α-actinin 2 (α-Affimers) and the N-terminal Z1/Z2 domains of titin (Z-Affimers) were used to screen for Affimers by phage display.

3.2 Method

3.2.1 Expression and purification of human muscle α-actinin 2 - actin binding domain (ABD)

The ABD cDNA construct within the *E. coli* expression vector pGEX-6p-1 was kindly provided by Dr. Marcin Wolny. The ABD (residues 1-269) with an N-terminal GST tag was expressed in BL21 (DE3) cells (400 mL culture), for 3 hrs at 37 ºC with 0.5 mM IPTG. After the protein was expressed the cells were first centrifuged (3,000 xg, 30 mins), resuspended in 10 mL of ABD lysis buffer (1 mM DTT, 1mM EDTA, 200 µg/mL lysozyme, 0.1% Triton X-100) and then lysed by sonication. The cell debris was separated from the lysate by another centrifugation (30,000 xg, 45 mins). The ABD was first purified from the lysate by glutathione affinity chromatography. The lysate was added to a polyproplene 5 mL column (Qiagen) column with 2 mL of glutathione resin (amintra). The lysate was rolled with the resin in the column at room temperature for 20 mins to allow the GST to bind the resin. The resin was then washed with 50 mL of PBS. 2 mL of precision protease buffer (20 mM Tris-HCl, 150 mM NaCl, pH 7.5) with 20 µL of precision protease (with a GST tag) (~2 mg mL^{-1}) was rolled with the resin overnight at 4 ºC to cleave the GST tag from the ABD. Following the precision protease treatment, the ABD was eluted off the column by washing the resin in 10 mL of precision protease buffer. The ABD was then exchanged in 50 mM NaCl, 20 mM Tris-HCl, pH 8.0 using a vivaspin 20 concentrator (MWCO = 10 kDa) (GE healthcare) and concentrated down to 2 mL.

To further purify the ABD sample anion exchange purification was used, using a 1 mL HiTrap Q FF (GE healthcare) column attached to an ÄKTA prime plus system (GE health care). The column was equilibrated in 50 mM NaCl, 20 mM Tris-HCl, pH 8.0. After the ABD sample was applied to the column, a NaCl salt gradient was set up over 30 mL from 50 mM to 600 mM at a rate of 0.4 mL min^{-1} using the two buffers: Buffer A (20 mM Tris-HCl, pH 8.0) and Buffer B (1M NaCl, 20 mM Tris-HCl, pH 8.0) a salt gradient. 2 mL fractions were collected. The ABD was seen to elute off the column at ~ 100 mM NaCl. After the purification the fractions were ran on an SDS-PAGE to assess the purity (**Figure 3.1A**). The fractions with the purified ABD were pooled and dialysed against the 2L PBS overnight.

3.2.2 Expression and purification mouse Z1/Z2 domains

The codon optimised Z1/Z2 cDNA for *E. coli* expression was synthesised and sub-cloned into pET28a-SUMO by genscript. The Z1/Z2 domains (residues 1-200) with an N-terminal 6x His-SUMO tag were expressed in BL21 (DE3) cells (400 mL culture), for 3 hrs at 37 ºC with 1 mM IPTG. After expression the cells were pelleted (3,000 xg, 30 mins, 4 ºC), resuspended in 10 mL of lysis buffer (20 mM Tris-HCl, 150 mM NaCl, 20 mM Imidazole pH 8.0) and lysed by sonication. Following this debris within the lysate was removed by centrifugation (30,000 xg, 4 ºC, 45 mins). The Z1/Z2 domains were initially purified from the lysate by nickel affinity chromatography. A gravity flow polyproplene 5 mL column (Qiagen) with 1 mL of cOmplete His-Tag purification resin (Roche) was used. After the lysate was applied to the resin, the resin was washed with 50 mL of Z1/Z2 wash buffer (20 mM Tris-HCl, 500 mM NaCl, 20 mM Imidazole pH 8.0) SUMO protease with a 6x His-tag (~ 2 mg mL^{-1}) in 2 mL of SUMO protease buffer (20 mM Tris-HCl, 150 mM NaCl, pH 8.0) was incubated with the resin on a roller overnight at 4 ºC. The resin was then washed with 10 mL of PBS to elute the Z1/Z2 domains off the resin. The protein was further purified by size exclusion chromatography before use in the phage display assay. A Tricorn 10/200 gp column (GE healthcare) packed with Superdex 75 Prep Grade (GE healthcare) was used on an AKTA Prime plus system and equilibrated in PBS. 300 uL of the Z1/Z2 sample was loaded onto the column and 30 mL of PBS was pumped through the column at a rate of 0.5 mL min^{-1}. Z1/Z2 sample at each stage of the of the purification were taken for SDS-PAGE analysis (**Figure 3.1B**). For more efficient purifications of Z1/Z2 in the future, using more than 1 mL of nickel resin to capture the Z1/Z2 domains from the lysate and incubating SUMO-protease with the Z1/Z2 domains off the column, would be recommended.

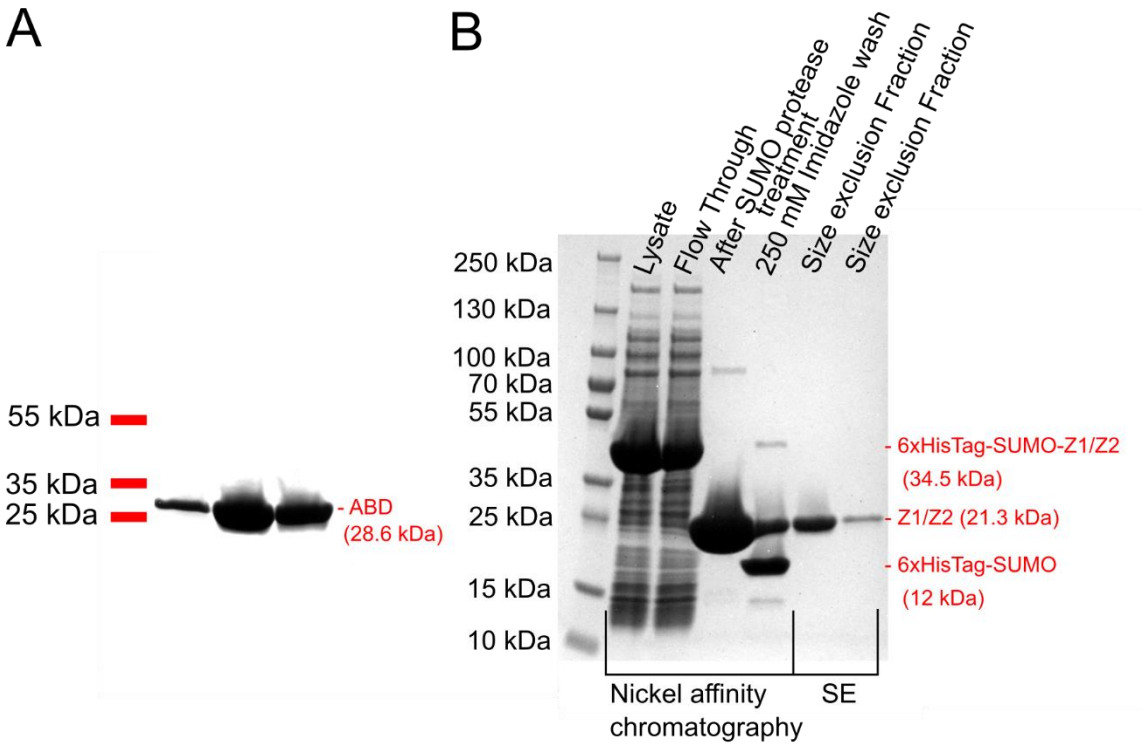

Figure 3.1 – SDS PAGE of the purified samples of the ABD and Z1/Z2 domains to be used as target proteins in phage display assays. All samples were added to the appropriate volume of 2x SDS sample buffer and boiled at 100 ºC for 5 mins before loaded on to 4-20 % acrylamide/Bis-acrylamide gels. **(A)** Final ABD samples after glutathione affinity chromatography and anion exchange chromatography, to be used for the phage display assay. **(B)** Purification steps for the Z1/Z2 domains. Samples of the lysate before and after (flow-through) it was applied to the nickel resin column were both loaded onto the gel for comparison. The wash sample after SUMO protease treatment on the resin shows the presence of the Z1/Z2 domains cleaved from the SUMO protease. The imidazole wash sample shows the presence of 6xHisTag-SUMO-Z1/Z2, cleaved Z1/Z2 and 6xHisTag-SUMO remained bound to the column. 6xHisTag-SUMO is seen to run as a species ~ 5 kDa larger than the MW of the tag. The final size exclusion samples show purified Z1/Z2 domains, which were then used for the phage display assay.

3.2.3 Generating Affimers that bind the ABD and Z1/Z2 domains

The phage display assays were performed by Dr. Christian Tiede. Biotinylated ABD and Z1/Z2 domains at a concentration of 0.5 mg mL^{-1} in PBS were separately used as protein targets for screening of an Affimer library by a phage display assay. These same purified proteins were additionally used to confirm that the Affimer clones obtained bound the targets *in vitro* by phage ELISA assay. The phage display assays were performed as previously described (**Tiede *et al.* 2014, Tiede *et al.* 2017**).

For the phage ELISA, the biotinylated targets were applied to streptavidin coated plates. Affimer phage bound to the target were detected by adding HRP anti-phage antibody (Seramun) and 3.3',5,5-tetramethylbenzidine (TMB), then measuring the absorbance at 620 nm. Affimers clones that were found to bind the targets were then sequenced and sub-cloned in to pET11a for *E. coli* expression.

3.2.4 Sub-cloning Affimer cDNA into pET11a

The cDNA sequence for each Affimer was sub-cloned from the phagemid vector pBSTG1 into the protein expression vector pET11a (section 2.5.1 **Figure 3.1C**). The forward and reverse primers were used for the PCR can be found in **Methods Table 2**. The PCR mixture contained; 10 µL 5x Phusion polymerase HF buffer, 1 µL dNTP (10 mM stock), 1.5 µL 100 % DMSO, 4 µL forward primer (10 µM stock), 4 µL reverse primer (10 µM), 1 µL pBSTG1- Affimer (10 ng μL^{-1}), 1 µL Phusion High-Fidelity DNA polymerase (1.0 unit μL^{-1}, NEB M0530S) and dH_20 to make the final volume 50 µL. The PCR parameters using a BioRad T100 thermocycler are as follows: Initial denaturation at 98 ºC for 30 secs followed by 30 cycles of denaturation at 98 ºC for 20 secs, annealing at 54 ºC for 54 secs and extension 72 ºC for 20 secs and finished with a final extension at 68 ºC for 10 mins.

After the PCR, the PCR product digested via incubation at 37 ºC for 2 hrs with 0.5 µL NotI-HF and 0.5 µL NheI-HF, 6 µL CutSmart Buffer and 3 µL dH_2O (60 µL final volume). The Affimer cDNA inserts were then purified by gel electrophoresis and gel extraction (**Methods 2.5.4**). The cDNA inserts were ligated into linear pET-11a using T4 DNA ligase (NEB) (**Methods 2.57**) and was then transformed into NEB 5α cells (NEB, C2987I) (**Methods 2.4**) for subsequent minipreps (**Methods 2.54**)

3.2.5 Purification of Affimers

All Affimers were expressed in 200 mL cultures of BL21(DE3) cells using 0.1 mM IPTG for 6 hrs at 25 ºC. After the Affimers were expressed the cells were pelleted via centrifugation (3,000 xg, 30 mins), resuspended in 10 mL of Affimer lysis buffer (50 mM NaH_2PO_4, 300 mM NaCl, 20 mM imidazole, 10% glycerol, pH 7.4) and lysed by sonication. To denature low thermostable *E. coli* host proteins the lysates were heated at 50 ºC for 30 mins. Following this, debris within the lysate was removed by centrifugation (30,000 xg, 45 mins). All Affimers were purified by nickel affinity chromatography. The lysate was passed through a polyproplene 5 mL column (Qiagen) column with 1 mL of cOmplete His-Tag purification resin (Roche). 50 mL of Affimer wash buffer (50 mM NaH_2PO_4, 500 mM NaCl, 20 mM imidazole, 10% glycerol, pH 7.4)

was used to wash the resin in the column. The Affimer sample bound to the resin was eluted off with 5x 2 mL fractions of Affimer elution buffer (50 mM NaH_2PO_4, 500 mM NaCl, 300 mM imidazole, 10% glycerol, pH 7.4). For direct labelling of Affimers with a C-terminal cysteine, the fraction with the highest concentration of Affimer was used. For long term storage the fractions were then pooled and dialysed in PBS (or PBS with 1 mM TCEP for Affimers with a C-terminal cysteine).

α-Affimer 9 (no cysteine) was further purified by anion exchange chromatography for analytical size exclusion and crystal screens. A 1 mL HiTrap Q FF (GE healthcare) column attached to an ÄKTA prime plus system (GE health care) with the buffers 20 mM Tris-HCl pH 8.0 and 1 M NaCl, 20 mM Tris-HCl pH 8.0. In the buffer conditions 50 mM NaCl, 20 mM Tris-HCl pH 8.0, α-Affimer 9 did not bind to the column and were collected in the first two fractions (each 2 mL). The Affimer was then dialysed overnight in 2 L of the appropriate buffer.

3.2.6 Labelling Affimers with commercial dyes

All Affimers used as binders for fluorescence microscopy have a single C-terminal cysteine in the sequence before the 8x Histidine tag. The Affimers were linked to a biotin molecule, AlexaFluor 647 and Cy3b via the cysteine and maleimide. Freshly purified Affimers (straight from the column) was diluted in PBS to a concentration of 0.5 mg mL^{-1} (~ 40 µM). 150 µL of Affimer stock was added to 150 µL of TCEP immobilised resin (Thermo scientific, 77712) for 1 hr on a roller at room temperature. This was to make sure the Affimer was in reduced conditions before the introduction of the biotin/dye. Before addition of the Affimer, the TCEP resin was washed in PBS with 1 mM EDTA and 6 µL of PBS with 10 mM EDTA was added. The resin and Affimer was centrifuged (2 mins, 1,500 xg) and the 130 µL of Affimer sample was separated from the resin. Straight after this 6 µL of 2 mM biotin or dye was added to the Affimer and incubated for 2 hrs at room temperature on a roller (covered in the dark if a dye was used). A Zeba (MWCO 7 kDa, 89882) desalting column was used to remove any free biotin/ dye from the Affimer sample. An SDS PAGE was ran of the dye labelled Affimers (**Figure 3.2**), the AF647 linked Affimer ran at a higher MW compared to unlabelled Affimers for labelling efficiency to be assessed. For long term storage 130 µL of 80% glycerol was added to the sample (40 % final dilution) and all Affimers were stored at -20 ºC.

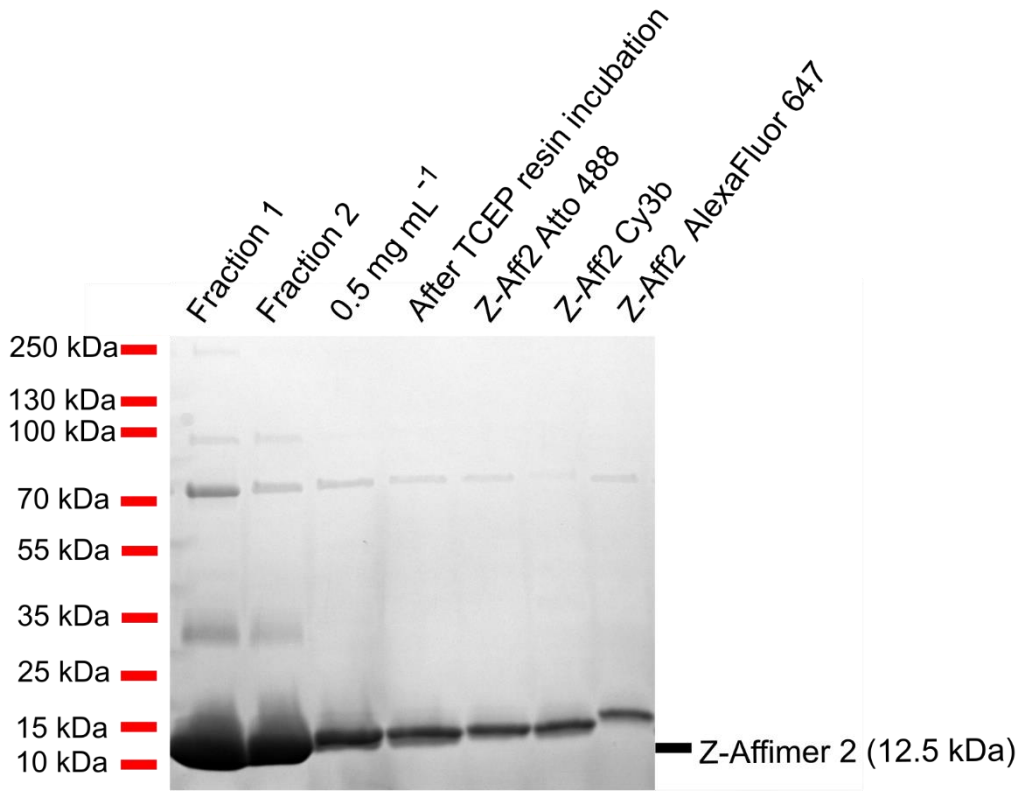

Figure 3.2- Example gel for the purification of Z-Affimer-2 and the direct labelling of Z-Affimer 2 with fluorescent dyes. From the left; Sample of fractions 1 and 2 after nickel affinity purification, fraction 2 diluted to 0.5 mg mL^{-1}, Affimer sample after incubation with TCEP resin, final Affimer sample linked to Atto 488, final Affimer sample linked to Cy3B and final Affimer sample linked to AlexaFluor 647.

3.2.7 Staining adult rat cardiomyocytes

The fixed cells plated on 13-mm diameter washed glass coverslips were permeabilised with 0.5 % Triton X-100 in PBS for 5 mins at room temperature. This was followed by a PBS wash (five washes in total). The cells were then blocked with BSA for 1 hr using 5 % BSA in PBS. The cardiomyocytes were first stained with 50 µL of anti- α-actinin 2 antibody (1:400) (Sigma, A7811, lot no. 024M4758) in 1 % BSA, incubated at room temperature for 1 hour. This was followed by a PBS wash (five washes in total). The cells were further co-stained with the Affimers directly linked to Alexa Fluor 647 (both α-Affimers and Z-Affimers, 1 in 200 dilution) and α- mouse Alexa Fluor 488 antibody (Life Technologies A11059, lot no. 1348651, 1 in 500 dilution). The coverslips were mounted onto microscope slides using Prolong Gold Antifade (Life Technologies, P36934). Cells were imaged using a 100x oil objective, on a DeltaVision Elite Microscope (GE Healthcare).

3.2.8 Size exclusion of Affimers, the ABD of muscle α-actinin and the N-terminal Z1/Z2 domains

A Tricorn 10/200 gp column (GE healthcare) packed with Superdex 75 resin attached to an ÄKTA Prime plus system was used for the size exclusion runs. 100 µL of protein samples were loaded onto the column for each size exclusion run. All protein samples were in PBS for runs involving α-Affimer 9 (no C-terminal cysteine) and all protein samples were in PBS with 1 mM DTT for runs involving Z-Affimer 12 (with a C-terminal cysteine). The column was equilibrated in either PBS or PBS with 1 mM DTT depending on the Affimer used for all runs. Affimer samples (40 µM α-Affimer 9 and 80 µM Z-Affimer 12) and the targets (10 µM ABD and 40 µM Z1/Z2) were separately ran down the column and the UV absorbance of the elution volumes were measured. Affimers with the target proteins samples, α-Affimer 9 with ABD (40 µM : 10 µM) and Z-Affimer 12 with Z1/Z2 (80 µM : 40 µM) were incubated for 30 mins at room temperature before the size exclusion runs.

The molecular weight of the protein species eluted off the column was estimated from runs using low molecular weight standards (Gel Filtration Calibration Kit, GE healthcare) (**Figure 3.3**). The elution volumes for each protein standards (where the UV absorbance was highest) were recorded and the Kav was calculated.

Kav = (protein species elution volume – void volume) / (column volume – void volume)

The column volume was 14.1 mL and the void volume, 6.08 mL, was measured by running dextran blue 2000 (1 mg mL^{-1}) down the column and recording the elution volume. The Kav values of the standards were plotted against the logMW and a standard curve was plotted. Using the standard curve, the estimated MW of the protein samples were calculated.

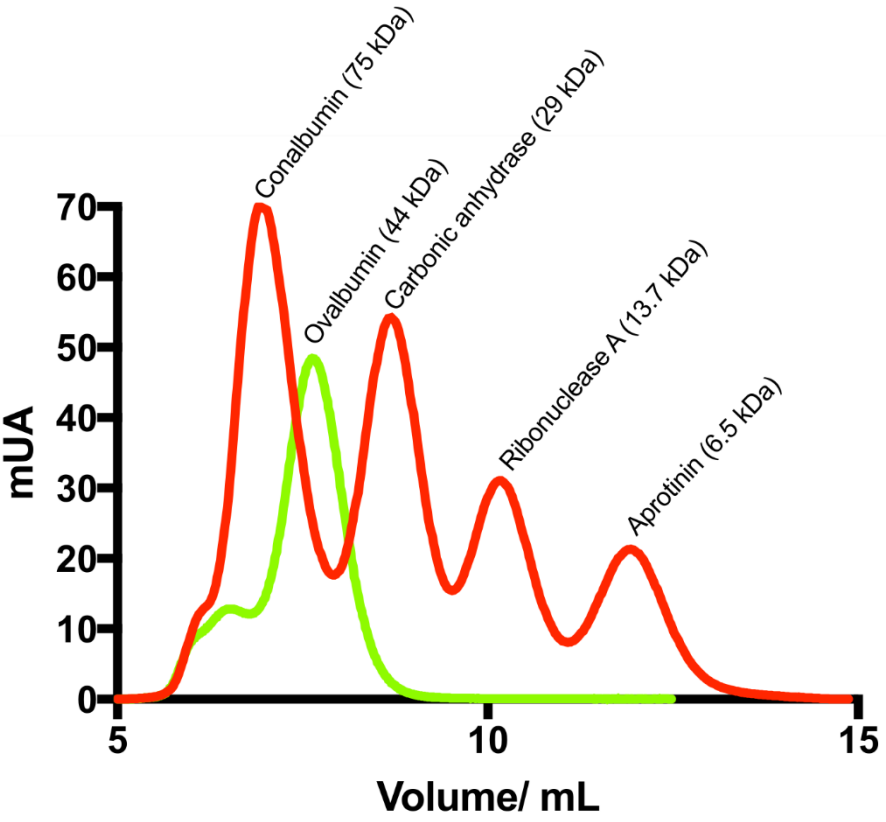

Figure 3.3 - UV absorbance traces from size exclusion runs using low molecular weight (LMW) standards (GE healthcare). LMW standards were ran through the tricorn 10/200 gp column (GE healthcare) packed with Superdex 75 Prep Grade (GE healthcare) attached ÄKTA Prime plus system. The UV absorbance trace of a 100 µL sample containing conalbumin, carbonic anhydrase, ribonuclease A and aprotinin (each 3 mg mL^{-1}) in PBS (red line) show resolved elution peaks for each standard. A 100 µL sample of ovalbumin (4 mg mL^{-1}) in PBS was ran separately (green line) as suggested in the manufactures protocol and the elution volume was recorded

3.2.9 X-ray crystallography structure of α-Affimer 9 bound to the ABD

In a volume of 300 µL, ABD (75 µM) and α-Affimer 9 (135 µM) were incubated at room temperature for 30 mins. Size exclusion was used to separate the ABD:α-Affimer 9 from free α-Affimer 9. The sample was loaded onto a Tricorn 10/200 gp column (GE healthcare) packed with Superdex 75 resin equilibrated in 75 mM NaCl, 20 mM Tris-HCl pH 7.5. At a flow rate of 0.5 mL min^{-1}, 1 mL fractions were collected. The fractions with the complex were pooled and concentrated to 60 µL for crystal screening using a vivaspin 6 (MWCO 3kDa) followed by a vivaspin 500 (MWCO 5 kDa), the final concentration was 7.2 mg ml^{-1}. Crystals were obtained by sitting drop crystal screens vapour diffusion method using JCSG (Joint Centre for Structural genomics) Core Suites 1 and 2 (Qiagen). 1.2 µL of protein sample was added to 1.2 µL of each buffer conditions and the plates were incubated at 20 ºC. Crystals grew with 20 % w/v PEG 3500 present. Data was collected from a crystal that grew using the buffer conditions -

0.2 M $(NH_4)_2$ Tart, 20 % w/v PEG 3500 . This crystal belonged to spacing group P 212121.

3.2.10 Data collection and structure determination

The data was recorded to a resolution range between 1.4 and 1.5 Å at 100 K on the macromolecular crystallography beamline station I04 at the Diamond Light Source by Dr Chi Trinh. The diffraction images were integrated, scaled and reduced using 3DII processing. The unit cell parameters obtained were *a* = 45.71 Å, *b* = 48.86 Å, *c* = 147.19 Å, *α* = 90º, *α* = 90º and *α* = 90º. 5 % of the reflections from the data collected were selected at random and excluded from the refinement using the program FREERFLAG and constituted the R_{free} set. The crystallographic structure of the α-Affimer 9 : ABD complex was solved by molecular replacement using the programme PHASER with the structures of the human wild type ABD from α-actinin 2 (PDB code 5A38, 100 % sequence identity, **Haywood *et al.* 2016**) and a solved Affimer structure (PDB code 4N6T, **Tiede *et al.* 2014**)

3.3 Results

3.3.1 Generating Affimers that specifically bind muscle α-actinin and the N-terminal end of titin

To generate Affimers, the ABD of muscle α-actinin and the N-terminal domains of titin (Z1/Z2) were cloned, expressed and purified and used as targets in separate phage display assays (**Figure 3.1**). Eight unique Affimer sequences for ABD (α-Affimers 1, 2, 3, 4, 5, 9, 11 and 15) and seven for Z1/Z2 (Z-Affimers 2, 5, 7, 12, 17 and 21) were identified from the screens. A phage ELISA confirmed the Affimer sequences obtained bind ABD (**Figure 3.4A**) and Z1/Z2 (**Figure 3.4B**) *in vitro*. The Affimer sequences were then sub-cloned into pET11a (with a single cysteine present at the C-terminal end before the 8x His-Tag), for *E.coli* (BL21 DE3) expression**.** All the Affimers were expressed and purified to then be directly labelled with biotin.

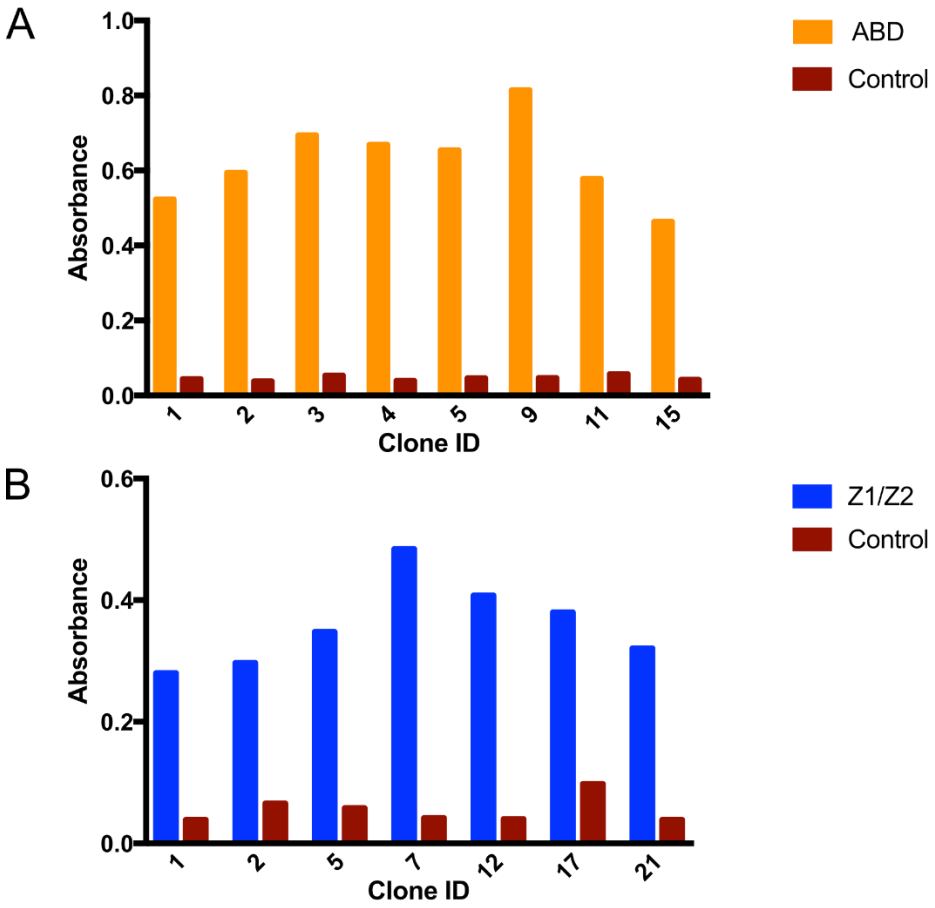

Figure 3.4 - Generating Affimers with the ability to bind the ABD of muscle α-actinin and the Z1/Z2 domains of titin. (**A**) Screening of eight unique ABD binding Affimer clones via a phage ELISA to confirm they bind the target. (**B**) Screening of seven unique Z1/Z2 binding Affimer clones via a phage ELISA to confirm they bind the target. All clones were tested in wells with the target protein present (ABD or Z1/Z2) and wells without the target (the control). The absorbance at 620 nm of oxidised TMB was measured. All clones showed a high absorbance with the target present compared to the controls confirming they bind their targets *in vitro*.

3.3.2 Fluorescence imaging of adult rat cardiomyocytes labelled with α-Affimers and Z-Affimers

Three of the biotinylated α-Affimers (α-Affimers 1, 9 and 15) and four of the biotinylated Z-Affimers (Z-Affimers 2, 5, 7 and 12) showed positive staining of rat cardiomyocytes by fluorescence microscopy with streptavidin directly linked to Atto 488 (data not shown). The presence of distinctive, regularly spaced stripes were observed in positive staining. These are likely the Z-disc regions in the cells. The remaining Affimers did not show positive staining (data not shown) in the cardiomyocytes, suggesting they cannot bind their targets in *vivo*. Either they are very weak binders, or they could not access their binding sites within the cell, or this might also be an effect of fixation conditions. For dSTORM, the Affimers are directly labelled with a fluorescent dye on the cysteine, to reduce linkage error. The Affimers which had shown positive staining (when biotinylated) were directly linked with AlexaFluor 647 (AF647) to use for dSTORM imaging of cardiomyocytes. Fixed cardiomyocytes were stained with α-Affimers 1, 9, 15 and Z-Affimers 2, 5, 7, 12 directly linked to AF647 and imaged by standard fluorescence microscopy to show the successful preparation of the Affimers before dSTORM (**Figures 3.5A and B**). Only α-Affimers 9 and Z-Affimer 12 showed the Z-disc stripped pattern expected, the other Affimers gave a high background fluorescence in the cardiomyocytes. One possible reason for is free dye in the Affimer samples and changes in the Affimer labelling protocol is required in the future. However, α-Affimers 9 and Z-Affimer 12 showed good staining and were therefore further characterised to determine their suitability for dSTORM.

3.3.3 Size exclusion analysis of Affimers bound to their targets

To confirm that the Affimers (non-dye labelled) are monomeric, and that they bind to their targets in vitro, size exclusion was used to assess the size of the Affimers and the stoichiometry of Affimers bound to their respective targets. After application of α-Affimer 9 (40 µM) a single Affimer species eluted off the column (**Figure 3.6A, red line**). The MW was estimated from the elution point of the Affimer species and the elution points of known protein standards (**Figure 3.6B**). The estimated MW (3.6 kDa) of α-Affimer 9 is much smaller that the known MW (12.5 kDa). A possible explanation for this is that the Affimer interacts with the superdex 75 resin, resulting in the elution of the Affimer later than expected. Therefore, the molecular weight of this Affimer cannot be reliably deduced by size exclusion chromatography. The ABD (10 µM) was applied to the same column (**Figure 3.6A, blue line**) and its estimated MW was calculated to be 34.7 kDa. This value is larger than the known MW (28.6 kDa). It is possible that the ABD is not entirely globular in nature causing it to elute off the column earlier than

expected (e.g. it has a slightly extended structure).

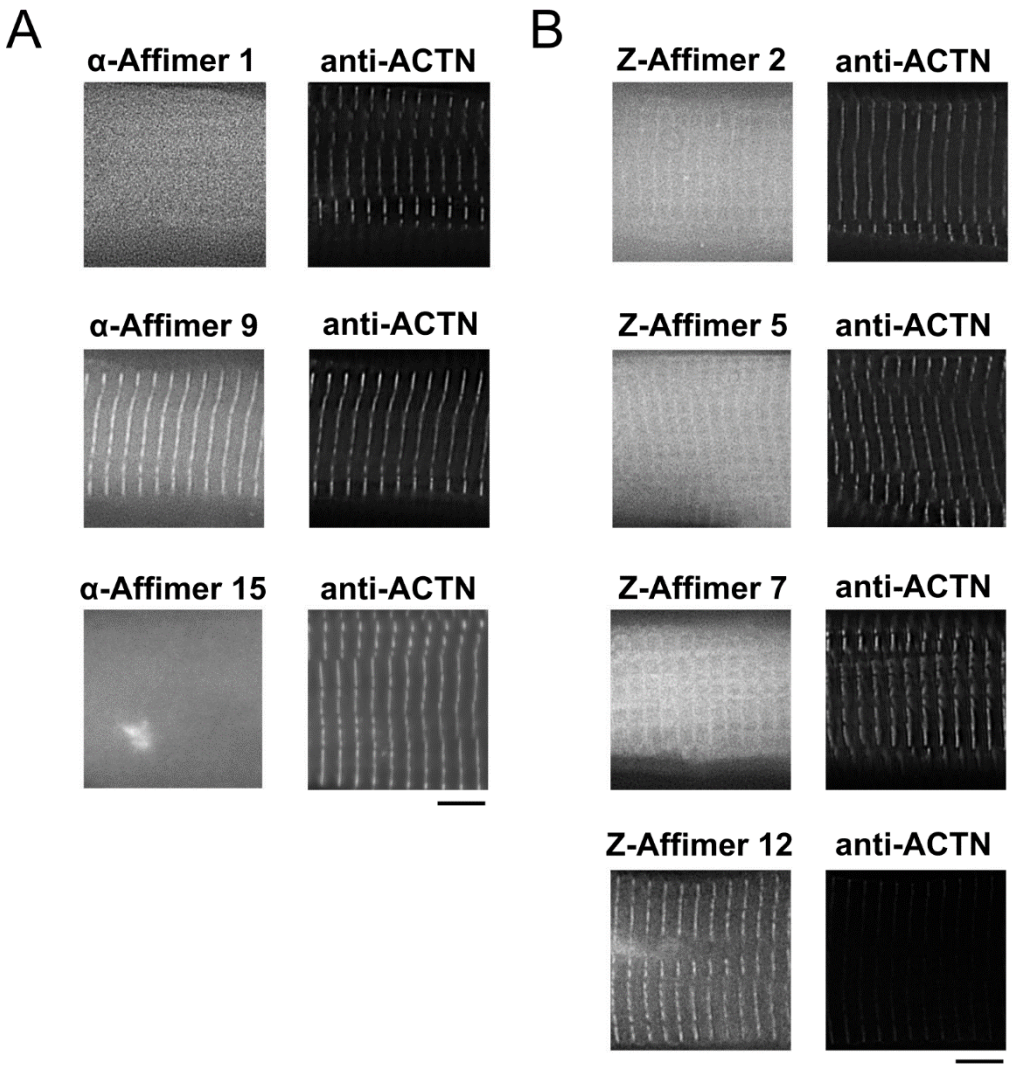

Figure 3.5 – Cardiomyocytes stained with Affimers. (**A**) Cardiomyocytes stained with α-Affimers 1, 9 and 15 each directly linked to AlexaFluor 647 and co-stained with anti- α-actinin antibody to show localisation in the Z-discs. (**B**) Cardiomyocytes stained with Z-Affimers 2, 5, 7 and 12 each directly linked to AlexaFluor 647 and co-stained with anti- α-actinin antibody to show localisation in the Z-discs. Sale bar = 5 μM.

Size exclusion was successful in confirming that α-Affimer 9 and its ABD target formed a 1:1 complex *in vitro*. Two different species eluted off the column. The first species is likely to be the ABD: α-Affimer 9 complex and the second, unbound Affimer 9, which was present in excess. SDS PAGE gel analysis of these two species (**Figure 3.6C**) confirmed that the first species contained both α-Affimer 9 and ABD and the second only contained α-Affimer 9. The estimated MW of the complex (species 1) is 42.7 kDa (**Figure 3.6B**), which is very close to the MW of a 1:1 complex (41.1 kDa). This suggests that the complex contains a 1:1 ratio of α-Affimer 9 and the ABD target.

Size exclusion was also used to evaluate the Z-Affimer 12 : Z1/Z2 complex *in vitro*. The Z-Affimer 12 (80 µM) sample eluted off the column as one species (**Figure 3.7A, orange line**) and eluted much later than expected (Estimated MW = 6.1 kDa, **Figure 3**.**7B**). The Z1/Z2 domains sample on the other hand (**Figure 3.7A, magenta line**) eluted off the column earlier than expected for a 21.3 kDa globular protein (Estimated MW = 31.2 kDa, **Figure 3.7B**). The linker region between the two Ig domains Z1 and Z2 is highly flexible which allows for different conformations of the Z1/Z2 domains (**Marino *et al.* 2006**). Therefore, the Z1/Z2 domains may have an extended conformation, that results in an earlier elution compared to a globular protein of the same size. Size exclusion chromatography of the complex of Z1/Z2 with Z-Affimer 12 (1:2 molar ratio) (**Figure 3.7A, blue line**) suggested that a 1:1 complex is formed *in vitro*. Two species elute off the column. An SDS PAGE of the elution volume confirms that species one is the Z1/Z2: Z-Affimer 12 complex (**Figure 3.7C**) and species 2 is free unbound Z-Affimer 12. Both the difference in estimated MW (**Figure 3.7B**) between Z1/Z2 and the complex (species 1), ~ 12 kDa, and free excess Z-Affimer 12 is present together confirms a 1:1 complex.

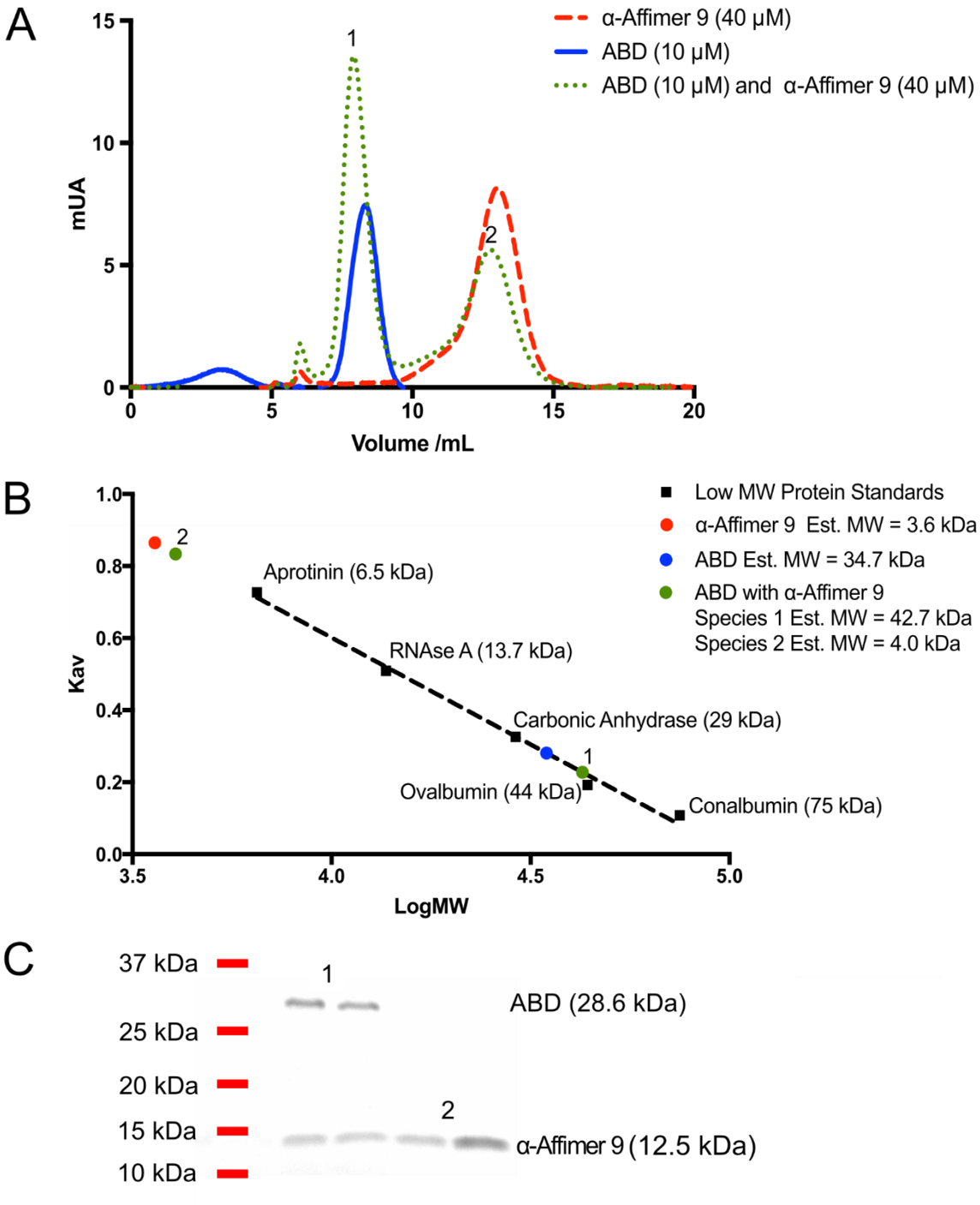

Figure 3.6 – Size exclusion runs of α-Affimer 9 (40 μM), ABD (10 μM) and ABD (10 μM) with α-Affimer 9 (40 μM) using a Tricorn 10/200 gp column (GE healthcare) packed with Superdex 75 resin. (**A**) UV absorbance traces for each size exclusion run. Two different species eluted off the column for the ABD with α-Affimer 9 sample and are labelled 1 and 2. The volumes at the top of the UV absorbance peaks were taken as the elution point for each protein species. (**B**) Kav/logMW plot of low molecular weight protein standards and protein species observed in **A**. Kav values were calculated from the elution points. The estimated MW of the different protein species were calculated from a standard curve generated from the protein standards. (**C**) Example gel of Species 1 and Species 2 after the α-Affimer 9 with ABD size exclusion run.

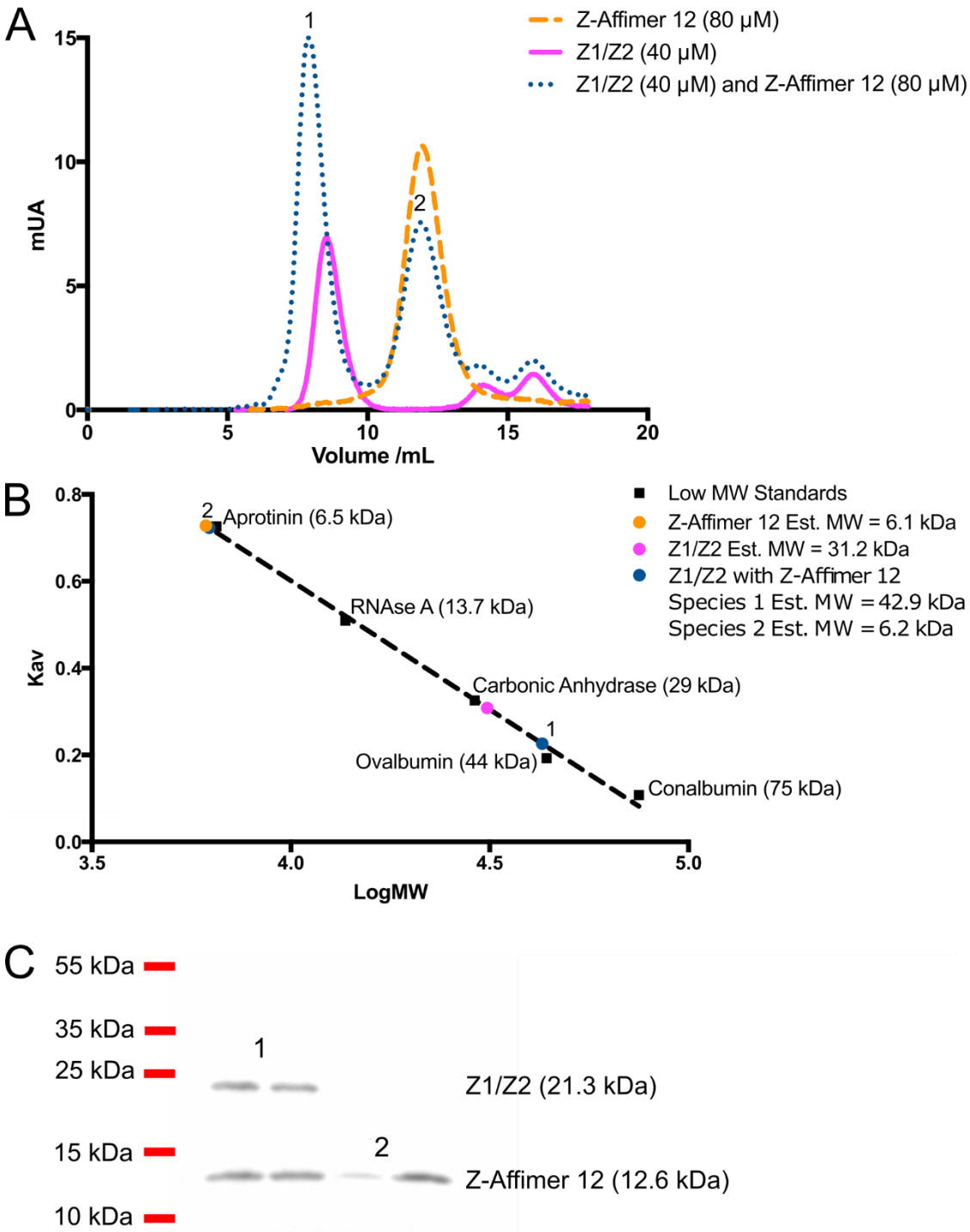

Figure 3.7 – Size exclusion runs of Z-Affimer 12 (80 µM), Z1/Z2 (40 µM) and Z1/Z2 (40 µM) with Z-Affimer 12 (80 µM) using a Tricorn 10/200 gp column (GE healthcare) packed with Superdex 75 resin. (**A**) UV absorbance traces for each size exclusion run. Two different species eluted off the column for the Z1/Z2 with Z-Affimer 12 sample and are labelled 1 and 2. The volumes at the top of the UV absorbance peaks were taken as the elution point for each protein species. (**B**) Kav/logMW plot of low molecular weight protein standards and protein species observed in **A**. Kav values were calculated from the elution point. The estimated MW of the different protein species were calculated from a standard curve generated from the protein standards. (**C**) SDS-PAGE of Species 1 and Species 2 after the α-Affimer 9 with ABD size exclusion run.

3.3.4 Heating of α-Affimer 9 to 50 ºC does not cause misfolding or aggregation

The protocol for the purification of Affimers involves a heat denaturing step at 50 ºC for 30 mins to remove any low thermostable *E. coli* host contaminant proteins present in the sample. The scaffold Affimer sequence is highly thermostable (Tm = 101 ºC) (**Tiede *et al.* 2014**), however with variable binding loops this may not be the case for all Affimers. Two separate sample of pure α-Affimers 9 were prepared; one with the heat denaturing step and one without the heat denaturing step. Size exclusion was used to assess if there was an increase in aggregation of α-Affimer 9, caused by the heat denaturation step. There were no noticeable differences between the elution profiles of the two samples (**Figure 3.8**), suggesting the heat step did not cause unfolding of α-Affimer 9 or aggregation. However, the exact thermostability of α-Affimer 9 and Z-Affimer 12 have yet to be determined. It should also be noted for purification of α-Affimer 9 without a C-terminal cysteine a heat denaturation step is not required. For direct labelling of Affimers using the C-terminal, the Affimer is labelled after the nickel affinity chromatography step and the heat denaturing step is required for a purer sample.

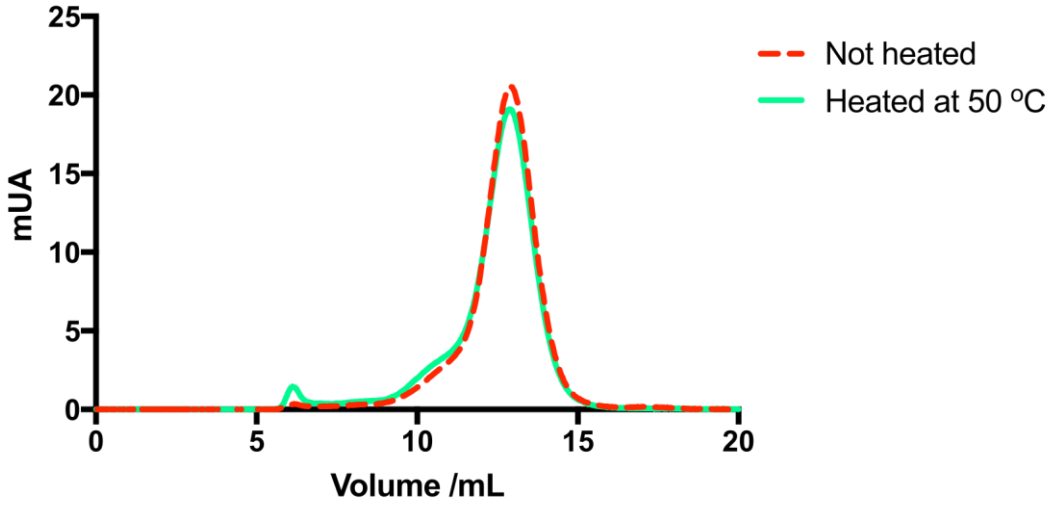

Figure 3.8 – Size exclusion of α-Affimer 9 samples heated to 50 ºC and not heated to 50 ºC. UV absorbance traces for both α-Affimer 9 samples (40 μM) shows no major differences in elution profiles.

3.3.5 Crystal structure α-Affimer 9 bound to the ABD

The X-ray crystallographic structure for the α-Affimer 9 : ABD complex was solved at a resolution of 1.4 Å (**Figure 3.9A**) . The ABD is in a “closed conformation” as seen in all human ABD crystal structures of α-actinins, whereby there are contacts between the two CH domains. Both binding loops 1 and 2 of α-Affimer 9 are packed in against the helix E of the CH2 domain of the ABD (**Figure 3.9B**). The larger loop 2 is the primary binding loop which has most contact with the CH2 domain. At the C-terminal end of the CH2 α-helix E there is hydrogen bonding between the amine group of K222 of the helix and D109, the backbone of N111 and F112 (**Figure 3.9C**). Also, H223 of the α-helix forms hydrogen bonding with F112 on binding loop 2. Only one hydrogen bond interaction forms between the α-helix of CH2 and the smaller binding loop 1 (**Figure 3.9D**), between W74 and the backbone of G211. The Affimer is not bound near any known actin binding sites so is unlikely to inhibit the ABD : actin interaction. However, the ABD with the Affimer bound did elute as a more globular species compared to the ABD alone in size exclusion chromatography (**Figure 3.6**). Thus, the Affimer may still have an inhibitory effect on the ABD as an increase transitional energy may be require to go between the closed and open conformations. Also, the Affimer binding site is not situated near the hypothesised PIP_2 binding site (R163, R169 and R192) and is unlikely to inhibit PIP_2 regulation of α-actinin.

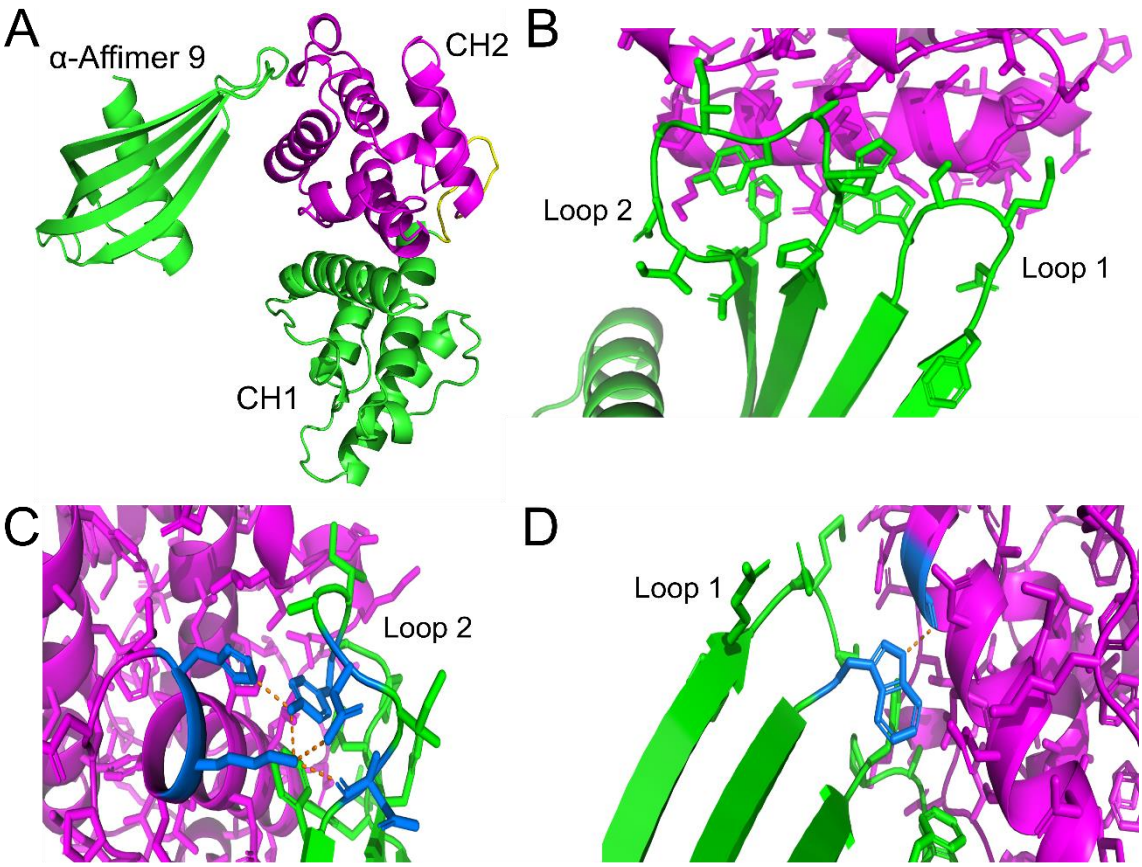

Figure 3.9 – X-ray crystallography structure of α-Affimer 9 bound to the ABD of muscle α-actinin. (**A**) The whole structure resolved to 1.4 Å. The Affimer (green) is bound to the CH2 domain (magenta) of the ABD via the two binding loops. (**B**) Close up of the two binding loops of α-Affimer 9 (green) interacting with the largest α-helix of CH2 (magenta). (**C**) Hydrogen bonding (orange dashed lines) between the residues of the α-helix and the binding loop 2 (blue) (**D**) Hydrogen bonding between the α-helix E and binding loop 1.

3.4 Discussion

Unique Affimers that bind proteins within the Z-discs of striated muscle cells were successfully raised and tested. Of the eight Affimers tested for the ABD of α-actinin 2, three successfully labelled the Z-disc in adult rat cardiomyocytes, with α-Affimer 9 showing the best staining. Of the seven Z-Affimers tested for the Z1Z2 domain of titin, four Affimers successfully labelled the Z-disc in both samples, and Z- Affimer 12 showed the best staining. Size exclusion chromatography of these two Affimers demonstrated that they both formed 1:1 complexes. Also, a crystal structure of α-Affimer 9 with ABD revealed the loop 2 of the Affimer is the major binding loop and forms contacts with the E helix of the CH2 domain.

Affimers are a strong alternative to antibodies. A number of Affimers have already been shown to work well for fluorescence microscopy (**Tiede *et al*. 2017, Lopata *et al.* 2018**) for a variety of targets. Their small size, and the ability to directly label the Affimers with a single fluorescent dye molecule, allows them to penetrate dense cytoskeletal regions such as the Z-disc in muscle cells and places the fluorophore close to the target protein. In contrast antibodies are large and using a combination of both primary and secondary antibodies can restrict access of antibodies, and additionally places the fluorophore at some distance from the target protein, increasing the 'linkage' error in super-resolution microscopy. Our results with the Z-disc Affimers demonstrates that they can be raised successfully to Z-disc proteins, and their small size should be an advantage for super-resolution microscopy approaches.

A possible reason why only three of the eight α-Affimers generated to the ABD of α-actinin-2 and only four of the seven Z-Affimers generated to the Z1/Z2 domains is that the epitopes that they recognise and bind to in fixed cells are not available, as they form part of the binding sites with other proteins. The ABD of muscle α-actinin binds actin filaments and the Z1/Z2 domains are bound to the titin capping protein telethonin (**Gregorio *et al.* 1998**). Equally, this approach also demonstrates that unique Affimers can be isolated to epitopes that are not blocked. This is very promising for generating Affimers in the future for fluorescence microscopy work investigating Z-disc proteins or for proteins that localise in equally dense networks.

Size exclusion chromatography showed that α-Affimer 9 and Z-Affimer 12 were both monomeric in solution and that they bound to their respective target to form a 1:1 ratio complex. This confirms that these Affimers have the potential to work well in dSTORM as a single Affimer will be bound to a single target molecule, with a single dye label

indicating its position in dSTORM. This shows that the Affimers chosen are suitable for dSTORM. Although I did not determine the binding affinity of the Affimers with their targets, the majority of Affimers bind to their target protein with high affinity (nanomolar range **Tiede *et al.* 2016**). The formation of a complex in the size exclusion experiments does indicate relatively strong affinity between the Affimer and its target.

Both the α-actinin 2 ABD and the titin Z1/Z2 proteins eluted earlier than expected from the size exclusion chromatography, suggesting that they may both have an extended conformation. The crystal structure of telethonin bound to the Z1/Z2 domains shows telethonin sandwiched by the two Z1/Z2 domains, with the Ig domains of Z1Z2 showing an extended structure (**Zou *et al.* 2006**). This extended structure is thought to be similar to the preferred conformational state of the Z1/Z2 domains free in solution, however other conformations are possible via the flexibility in the linker loop (**Marino *et al*. 2006**).

The ABD of α-actinin is also two globular domains (CH1-CH2) connected by a small linker loop. However, it is generally considered that the ABD of all α-actinins are in a closed conformation and then adopt a more open conformation when bound to actin (**Galkin *et al.* 2010, Franzot *et al.* 2005**). Previous crystal structures of the α-actinin ABD and the crystal structure here (**Figure 3.9A**) shows the ABD in a globular "closed conformation" whereby the two CH domains form contacts with one another. Analytical Ultracentrifugation (AUC) of the ABD from non-muscle α-actinin 4 (at 20 and 37 ºC) indicates that the ABD is in the closed conformation when free in solution (**Lee *et al.* 2008**). However, the size exclusion run of the ABD from muscle α-actinin 2 shows ABD sample elutes off the column earlier than expected of a globular protein of the same size (**Figure 3.6A and B**). The elution profile of the ABD sample is similar to that of the Z1/Z2 domains. This suggest the ABD population is not globular and may adapt a more open conformation. This is surprising as the residues within the interface of the CH domains are highly conserved between the different isoforms of human α-actinins (see section **1.2.2**). However, the size exclusion runs were conducted at 4 ºC, not physiological temperature, which could account for the differences observed and the ABD eluted off the column as a globular species with α-Affimer 9 bound. The size exclusion chromatography only indicates the ABD population is not globular compared to protein standards (GE Healthcare), further experimentation such as AUC would be required for the ABD from muscle α-actinin 2.

Chapter 4 – Arrangement of α-actinins and the N-terminal ends of titin in the Z-disc

4.1 Introduction

Within the Z-disc lattice structures of striated muscle cells the arrangement of α-actinin is thought to be ordered along the actin filaments (the axial direction of the cells). As discussed in section 1.2, along a single actin filament layers of α-actinin are spaced 19.2 nm apart and following the 4^3 screw symmetry of the actin, rotated 90 º from each other (**Figure 4.1A**). Each layer comprises of pair of α-actinin molecules spaced 2.74 nm apart (a single G-actin subunit) and orientated 167.4 º away from each other on the filament. In slow muscle, six α-actinin layers have been observed by EM (**Luther *et al.* 2002**). There can however be variation in the spacing between bound α-actinin on different actin filaments (transverse directions) due to the heterogeneity of the Z-disc lattice conformation (small square and basket weave). The lattice spacing for the small-square lattice conformation within cardiac muscle has been reported to be 20 - 30 nm (**Goldstein *et al.* 1989, Burgoyne *et*. *al* 2015**) (**Figure 4.1B**). A 20 % increase in lattice spacing has been reported for the basket weave conformation (**Goldstein *et al.* 1989**). By X-ray diffraction both conformational states are seen to present in the Z-discs of rabbit psoas muscle no matter if the muscle sample is tense or relaxed (**Pres-Edward *et al.* 2011**). However, the ratio between these conformational states in the Z-discs depends on the state of the muscle.

It is unclear where the N-terminal Z1/Z2 domains are localised in the Z-disc. There have been conflicting results from different studies investigating the localisation of Z1/Z2 domains by immuno-EM. One indicates titin starts at the edge of the Z-disc region (**Gregorio *et al.* 1998**) in human soleus muscle whilst the other indicates that titin starts well within the Z-discs (**Gautel *et al.* 1996**). In these cases, different antibodies that bind Z1/Z2 domains of titin were used on different muscle tissues, which could account for the discrepancy of the results observed. Also, as mentioned earlier (section **3.1**), the labelling efficiency of antibodies, especially when bound to 10 nm nanobead gold particles within the dense cytoskeletal network of the Z-discs is questionable due to the antibody size. Two Z1/Z2 domains from separate titin chains are thought to be cross-linked by telethonin to form a palindromic complex (**Zou *et al.* 2006**, **PDB code 1YA5**). Both the Z1/Z2 domain and telethonin co-localise in the Z-discs of neonatal rat cardiomyocytes and in four day differentiated human skeletal myofibrils as demonstrated by immunofluorescence microscopy (**Zou *et al.* 2006, Mues *et al.* 1998**). As the Z-repeats of titin are thought to interact with α-actinin, the

Z1/Z2 domains have been modelled at the end of the actin filaments in the Z-discs (**Zou *et al.* 2006**).

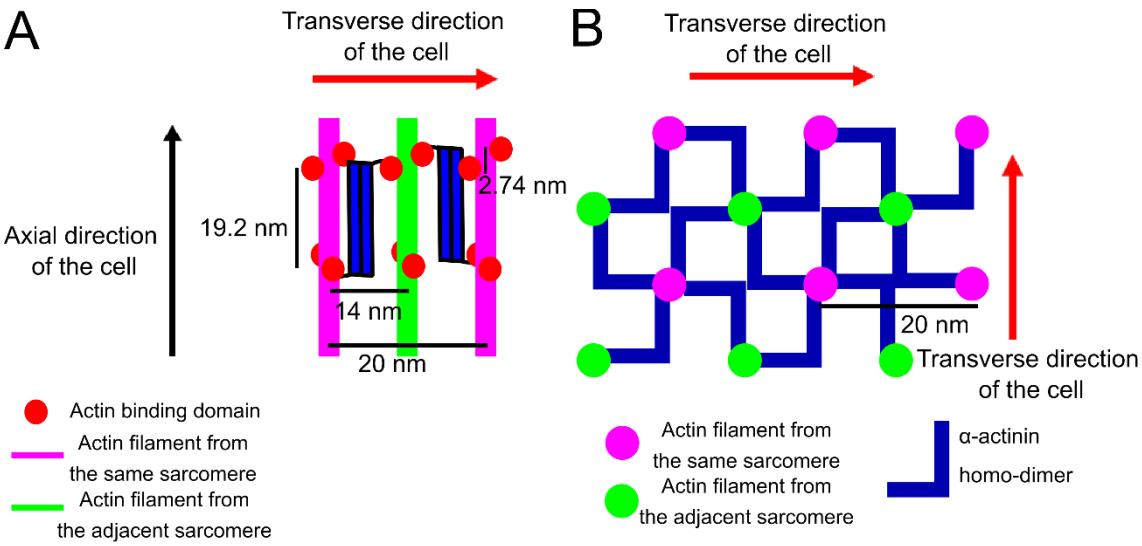

Figure 4.1 – Views of the Z-disc. (**A**) Side on view of the Z-disc in the small square conformation. (**B**) Transverse view of the Z-disc in the small square conformation.

In the previous chapter, Affimers were generated to bind both α-actinin 2 (CH domains) and the N-terminal domain of titin. In this chapter, dSTORM will be used with the Affimers to obtain localisation information for α-actinin and the Z1/Z2 domains within the Z-discs of cardiomyocytes. The localisation data will be further analysed by a novel form of pattern analysis. Studies of how these proteins are arranged within the Z-discs have mainly relied upon finding the binding partners of these proteins, not microscopy techniques. Studying the arrangement of α-actinin in the Z-disc by dSTORM first, before other Z-disc proteins, acts as a proof of principle for the technique. The regular arrangement observed in EM studies should also be seen by dSTORM. The arrangement of the N-terminal end of titin in the Z-disc lattices is less certain, therefore using super-resolution fluorescence should shed light on how the domains localise in the Z-discs.

4.2 Methods

4.2.1 Staining adult rat cardiomyocytes for dSTORM imaging

Adult rat cardiomyocytes seeded onto 25 mm coverslips (cleaned as described **Schierle *et al.* 2011**) were either stained with α-Affimer 9 or Z-Affimer 12 directly linked to Alexa Fluor 647 (AF647). The cardiomyocytes were first permeabilised using Triton X- 100 in PBS (0.5 % for labelling with α-Affimer 9 and 0.2 % for labelling with Z-Affimer 12) and incubated at room temperature for 5 mins, then washed in PBS. The cardiomyocytes were then blocked with 5 % BSA in PBS at room temperature for 1 hr. The Affimers were diluted in 1 % BSA in PBS before incubation with the cardiomyocytes at room temperature for 1 hr in the dark. A dilution of 1 in 750 of α-Affimer 9 was used (Final concentration ~ 0.6 µg mL^{-1}) and a dilution of 1 in 500 of Z-Affimer 12 was used (Final concentration ~ 1 µg mL^{-1}).

The coverslip was mounted into a chamber suitable for the 3D STORM microscope (as described in Section **2.10**). The coverslips were incubated with 0.01 % poly-l lysine (Sigma Aldrich, P4707) for 10 minutes at room temperature, then 200 µl of 150 nm diameter gold fiducials (Sigma Aldrich 742031, diluted 1/10 from stock supplied from the manufacturer) were applied to the sample and allowed to settle on the coverslip. Excess fiducials were then removed, and the imaging buffer was added to the chamber. The STORM buffer contained, 10 % glucose (w/v), 0.5 mg ml^{-1} glucose oxidase, 80 µg ml^{-1} catalase, 110 mM β-mercaptoethanol, PBS pH 8.0).

4.2.2 dSTORM image acquisitions and 3D histogram reconstruction

The workflow for dSTORM image acquisition followed that published (**York *et al.* 2011**) (see https://github.com/AndrewGYork/palm3d for further details) and included capture of a calibration image stack of a selected 150 nm gold nanoparticle in steps of 50 nm in z over a 4 micron range. The fluorescent dyes (Alexa Fluor 647) in the sample were excited using a 642 nm laser (100 mW), until a sufficient number were quenched (**Heilemann *et al.* 2009, 2008**) for spatially nearby emission events to be separated in time, following which we began data collection (exposure time 50 ms, EMCCD gain 150). When fluorescent events appeared to dye down a 405 nm laser with increasing power from 2 to 20 mW was used to re-activate the fluorophores. Fluorescent events lasting for more than one frame were linked into averaged localisations, which were finally binned into a histogram for display, accounting for distortion by the cylindrical lens. All the localisation co-ordinates collected in a single field of view were binned together in a final histogram.

4.2.3 Constructing 3D relative position density histogram

The 3D relative position density (RPD) histograms were generated by scripts created by Dr. Alistair Curd and ran in SPYDR. The 3D RPD histograms were generated by: (**1**) **Aligning the 3D dSTORM cardiomyocyte reconstructions**. Every 2D dSTORM reconstruction of labelled cardiomyocytes was rotated so that the cell axis is pointed along the x. This allows for dSTORM localisation datasets from different cardiomyocytes to be combined as the 3D relative position data were in the same co-ordinate system across all cardiomyocytes. For the 3D RPD histogram the x axis represents the axial direction of the cell and the y and z axis both represent the transverse plane of the cell. (**2**) **Filtering of localisations based on localisation precision**. Only localisations with a localisation precision less than or equal to 5 nm were used (**Figure 4.2A and B**). The localisation precision for each localisation was estimated using the equation - $\sigma / \sqrt{N}$, the standard error on the localisation precision. N is the number of photons emitted from each fluorescent event above background. σ is the mean of the two widths from a 2D gaussian fit from the relevant image from the calibration stack of the nano-gold particle. (**3**) **Plotting the 3D RPD histogram.** Relative positions are the distances between pairs of localisations. In turn, every localisation in the dSTORM histogram is assigned the co-ordinates (0, 0, 0 in x, y and z) then all neighbouring localisations (within a certain range) are plotted per nm in the 3D histogram. The range used in this case was 140 nm as the width of the Z-discs in cardiomyocytes have been reported to be 100 – 140 nm (**Luther *et al.* 2003**). The final density observed in the histogram is the relative position counts per nm. (**4**) **Generating 1D relative position density profiles**. To better visualise the pattern in the 3D relative position density histogram (RPD) and thus analyse the data, 1D RPD were generated for the axial direction and the transverse planes. The relative position density in the axial direction of the 3D RPD histogram, within the range of 0 – 10 nm in the transverse planes was plotted. Likewise, the relative position density in the transverse planes of the 3D RPD histogram, within the range of 0 – 10 nm in the axial direction was plotted.

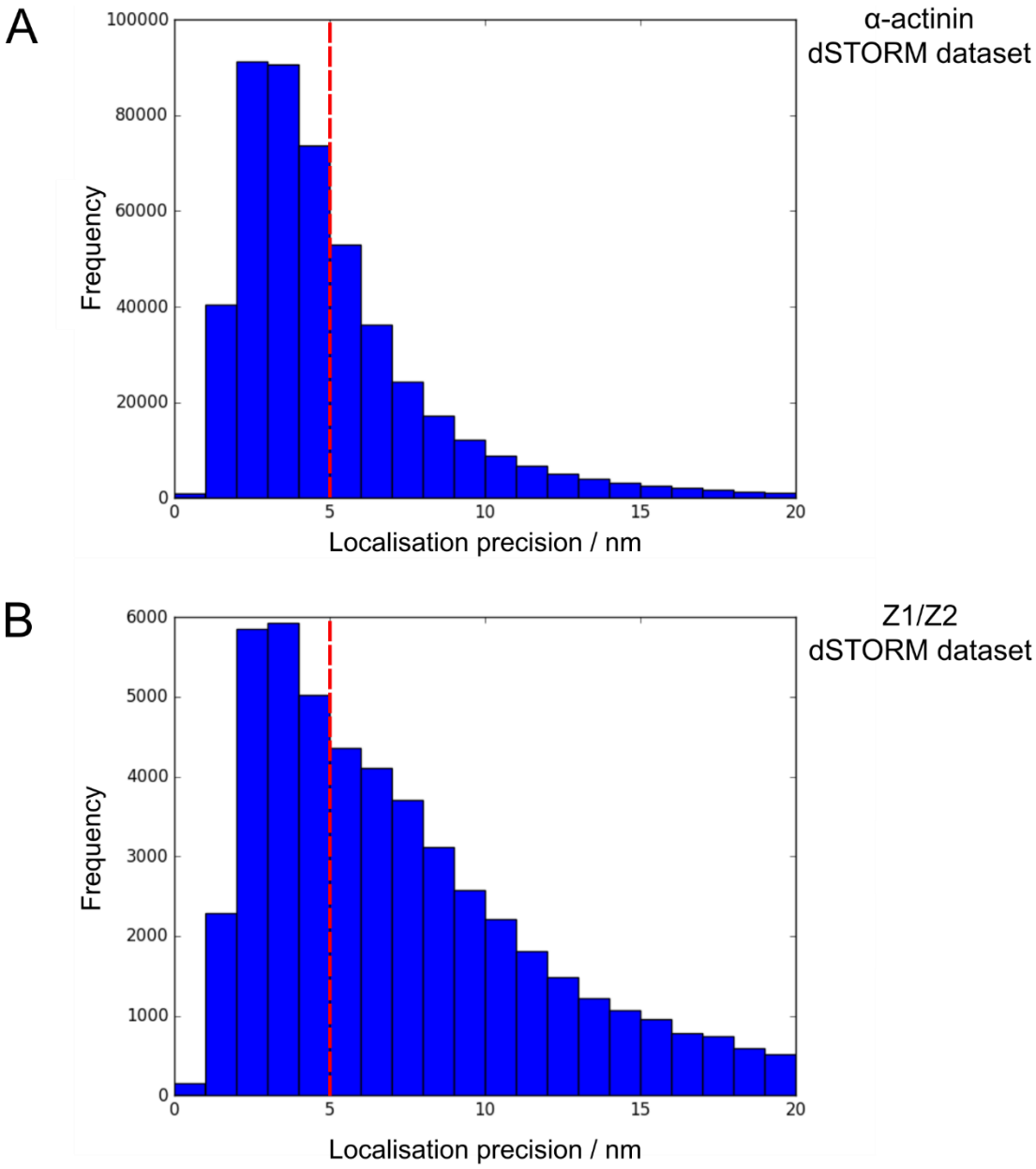

Figure 4.2 – Localisation precision of dSTORM localisations. (**A**) α-actinin localisation dSTORM dataset from three different cardiomyocytes. (**B**) Z1/Z2 localisation dSTORM dataset from three different cardiomyocytes. Sub-sets of localisations with a localisation precision of ≤ 5 nm were used for further PERPL analysis.

4.3 Results

4.3.1 Imaging adult rat cardiomyocytes by dSTORM using α-Affimer 9 and Z-Affimer 12 linked to AlexaFluor 647

To obtain localisation information for α-actinin 2 and the N-terminal ends of titin in the Z-discs of adult rat cardiomyocytes by dSTORM, the fixed cells seeded on coverslips were separately labelled with α-Affimer 9 and Z-Affimer 12 directly linked to Alexa Fluor 647 (AF647). dSTORM involves rapid imaging the same field of view (FOV) whilst the AF647 dyes are activated via an excitation laser (642 nm wavelength, 100 mW). Fields of view which had a single cardiomyocyte and at least one fiducial marker (for image drift tracking) were chosen for imaging (**Figure 4.3A and B**). Whilst the excitation laser is on, the AF647 dye population are constantly cycling between photon emitting and dark states, due to the dye quenching buffering conditions of the cells during imaging (**Heilemann *et al.* 2009, 2008**). Only a sub-set of the AF647 dyes are activated within the cardiomyocytes at any one time. Therefore, each image taken of the FOV captures sparsely activated individual fluorescent events. The localisation co-ordinates for each of the fluorescent events (in x, y and z planes) are then determined from all the images and are plotted in the final 3D histogram.

The 3D dSTORM reconstruction of single cardiomyocytes labelled with either α-Affimer 9 (**Figure 4.3C**) or Z-Affimer 12 (**Figure 4.3D**) showed the regular Z-disc striped pattern (shown as 2D plots, projected in z). At 100 nm binning of localisation points, the histograms are comparable to cardiomyocytes stained with the Affimers imaged by conventional fluorescence microscopy techniques. Low levels of localisations outside of the Z-discs were seen, thought to be caused by non-specific binding of Affimers together with background auto-fluorescence of the cardiomyocytes. When the localisations were binned together over a smaller distance (10 nm) (**Figure 4.3E and F**), the localisations within the Z-disc regions could be seen. However, analysing the localisation dataset in this format to gauge the arrangement of the Z-disc proteins can be problematic. There are two main reasons for this: (1) The labelling efficiency of the Affimers is not 100 % and not all of the target Z-disc proteins were labelled within the cardiomyocytes. (2) The localisation precision, the precision at which the co-ordinates for each fluorescent event is plotted, were different for each localisation (**Figure 4.2A and B**). For a sub-set of localisations collected per field of view, the localisation precision was not of a quality to resolve the arrangement of protein in the Z-discs. Therefore, further analysis of the dSTORM dataset was required to determine the arrangement of α-actinin and the N-terminal ends of titin in the Z-discs.

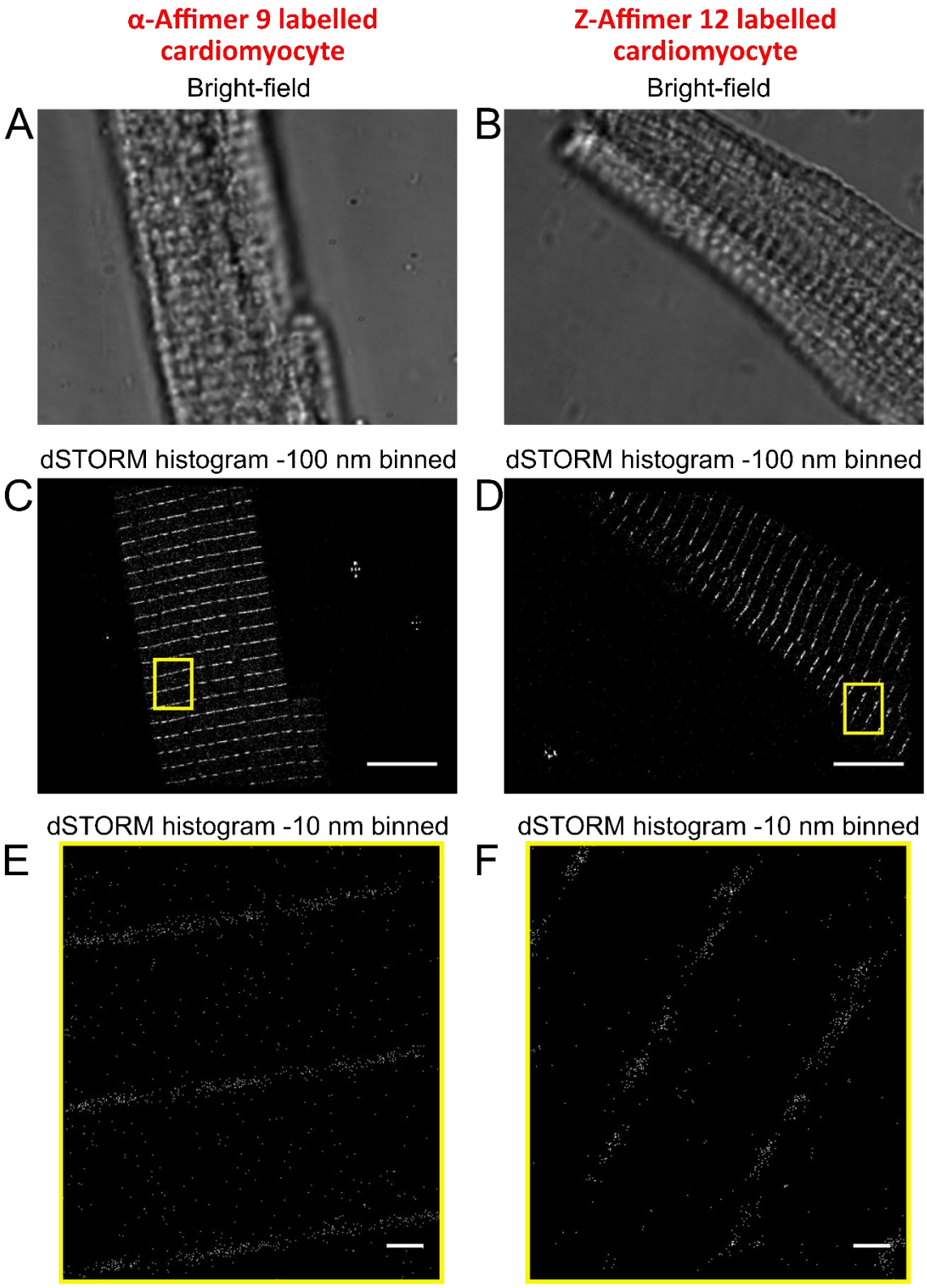

Figure 4.3 – dSTORM imaging of cardiomyocytes labelled with α-Affimer 9 and Z-Affimer 12. (**A**) and (**B**) bright field images of the cardiomyocytes before dSTORM. (**C**) and (**D**) 2D dSTORM reconstruction (100 nm binned histogram). Scale bar = 8 μM. (**E**) and (**F**) 2D dSTORM reconstruction (10 nm binned histogram) of a subset of localisations. Scale bar = 400 nm.

4.3.2 Using PERPL analysis to determine the arrangement of α-actinins in the Z-discs

The localisations datasets for α-actinin in cardiomyocytes were then further analysed using PERPL (patterns extracted from relative positions of localisations), developed by Dr. Alistair Curd, University of Leeds (currently unpublished). PERPL analysis involves generating a 3D relative position density (RPD) histogram (**see Methods 4.2.3**) from localisation pairs in the dSTORM datasets and analysing the pattern in the histogram. If there is a regular arrangement of a target protein *in vivo,* there would be common distances between pairs of localisations (relative positions) in the dSTORM dataset and a pattern in the 3D RPD histogram would be observed. For this analysis 100 % labelling efficiency of the Affimer is not required, datasets from different FOV can be combined into the same 3D RPD histogram and localisation data used can be filtered based upon localisation precision.

For the analysis of the arrangement of α-actinins in the Z-discs, dSTORM localisation datasets from three different fields of view of single cardiomyocytes labelled with α-Affimer 9 were collected. These datasets were initially combined (total number of localisations ~ 135,000), and a localisation precision cap of 5 nm was used (**Figure 4.2A**) as most of the dataset was retained, whilst the resolution of the data is off a quality to discern the arrangement of the α-actinin in the Z-discs. The 3D RPD histogram generated from the combined dSTORM datasets (**Figure 4.4A**)**,** shown here as a 2D representation) clearly shows the highest RPD between 0-20 nm in the axial direction, the RPD dissipating the further along the axial direction and a weak to no RPD signal past 100 nm (**Figure 4.4A**). The Z-discs in cardiomyocytes are ~ 100 nm wide, it was therefore not unexpected for there to be weak to no RPD past 100 nm. Also, it was not unexpected for RPD to dissipate the further along in the axial direction. For each six layers of α-actinins regular spaced on an actin filament (in the axial direction, **Figure 4.1**) there will be more relative positions between pairs of α-actinins closest together (~ 19.2 nm) compared the relative positions of furthest apart from one another (~ 96 nm). However, from the 3D and 2D RPD histogram plots alone it is hard to discern a pattern as there is a high background.

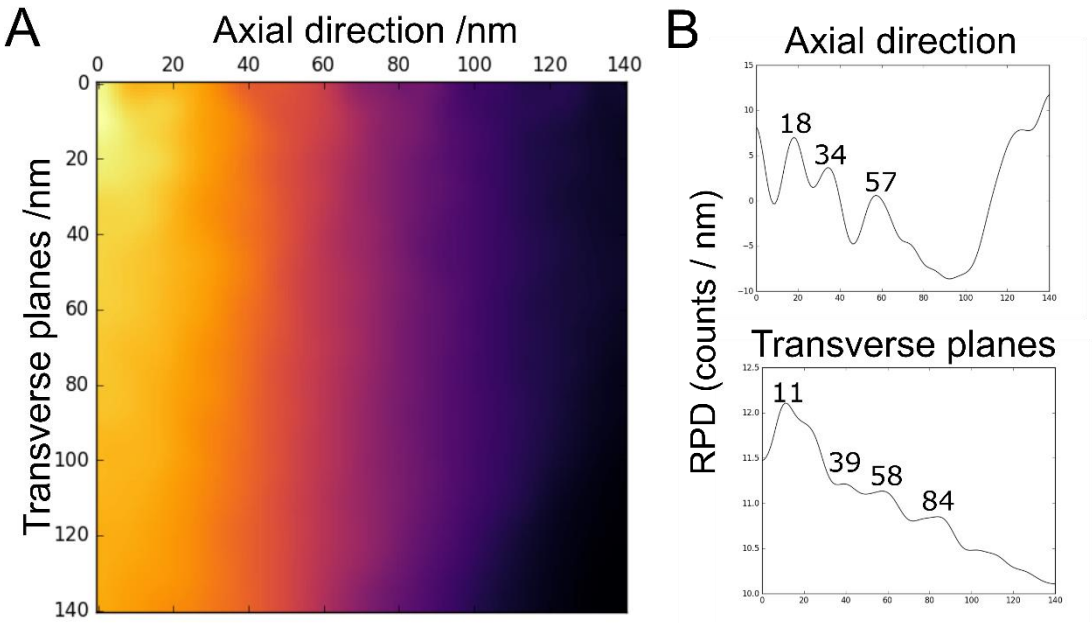

Figure 4.4 – PERPL analysis of combined α-actinin dSTORM localisation datasets. (**A**) 2D representation of the α-actinin 3D relative position density histogram. (**B**) 1D relative position density profiles for the axial direction and in the transverse planes from the RPD histogram.

To better visualise the RPD pattern above background in the histogram, 1D RPD profiles were generated for the axial direction of the cell and the transverse plane of the cell (**Figure 4.4B**, **See methods 4.2.3**). In the axial direction the 1D RPD profile was expected to show high relative position densities above background at 19.2, 38.4, 57.6, 76.8 and 96 nm, representing the 19.2 nm spacings between the six α-actinin layers in the Z-discs. The axial profile shows three distinct high RPD peaks 18, 34 and 57 nm, representing a repeating spacing pattern of α-actinin of ~ 18 nm. This is very similar to the expected spacing (~ 19.2 nm) and a clear repeating pattern can be seen. The ~ 1 nm difference in α-actinin spacing observed in previous EM studies and the spacing seen here could be due to the limitations of the localisation precision. Also, there were three distinct peaks in the RPD profile not five peaks representing spacing between six layers of α-actinins. As previously stated, there are fewer relative positions between α-actinins spaced further apart along the actin filament in the dataset. In the axial profile the RPD significantly reduced after ~ 60 nm in the axial direction and there is no discernible pattern. The collection of more dSTORM data would be required to better show the RPD pattern past 60 nm in the axial direction.

The greatest RPD in the transverse plane profile is at 11 nm (**Figure 4.4B**). One possibility for this is the spacing between the two actin binding domains of the same α-actinin layer bound to the same actin filament (~10 nm in the transverse planes, **Figure**

4.1). However, the relative positions between actin binding domains in the same layer (separated 2.74 nm apart) were not observed in the axial direction RPD profiles. With the localisation precision of the datasets (≤ 5 nm) it is unlikely that small relative positions will be resolved. The high RPD at 11 nm could also represent the spacing between α-actinin ABD bound to actin filaments from different sarcomeres. The distance would be ~14 nm if the lattice spacing is ~ 20 nm (**Figure 4.1**). This spacing could be observed as 11 nm in the profile because of the linkage error of α-Affimer 9 (~ 3 nm). The transverse planes profile also shows a repeating pattern of ~20 nm. There are peaks above background at ~ 20, 39, 58 and 84 nm. This pattern could be the lattice spacing, the spacing between actin filaments from the same sarcomere (~20 nm, **Goldstein *et al.* 1989**). However, there is not a distinct peak at 20 nm. The profile also does not show the presence of two different conformations of Z-disc lattice present in the cardiomyocytes (small square and basket weave). It can be argued the localisation precision of the dSTORM dataset is too poor to show the different conformations if they were both present in the cardiomyocytes imaged.

PERPL analysis was also used for each individual FOV α-actinin dSTORM dataset in addition to the combined dataset to gauge any variation between cardiomyocytes (**Figure 4.5, PERPL analysis**). The difference in number of localisations for each dataset varied widely, and this was due to a different number of acquisitions for each dataset; 7 for FOV 1 (**Figure 4.5A** ~ 100,000 localisations) and only 1 for FOV 2 (**Figure 4.5B** ~ 24,000 localisations) and FOV 3 (**Figure 4**.**5C** ~ 6,000 localisations). The labelling efficiency of the α-Affimer 9 could also had been a factor in the different size datasets. It is clear as the FOV 1 dataset contains many more localisations compared to FOV 2 and 3, therefore the RPD profiles for FOV 1 (**Figure 4.5A**) is similar to the profiles of the combined dataset (**Figure 4.5D**). The axial direction RPD profile of the FOV1 dataset even shows five peaks above background representing. It can be argued PERPL analysis of a single FOV dSTORM dataset can be used to reliably determine the protein arrangement. Despite FOV 2 and 3 having smaller localisation dataset, patterns in the 1D RPD profiles could be seen (**Figure 4.5B and C**). However, the patterns observed on the FOV2 and FOV3 RPD profiles deviate from the pattern expected from the known arrangement of α-actinins in the Z-disc (from EM studies). Also, the RPD profiles in the axial direction for the different fields of view are not consistent with one another. The RPD profiles generated from FOV2 and 3 highlight the need for large localisation datasets (similar to FOV 1) for reliable PERPL analysis.

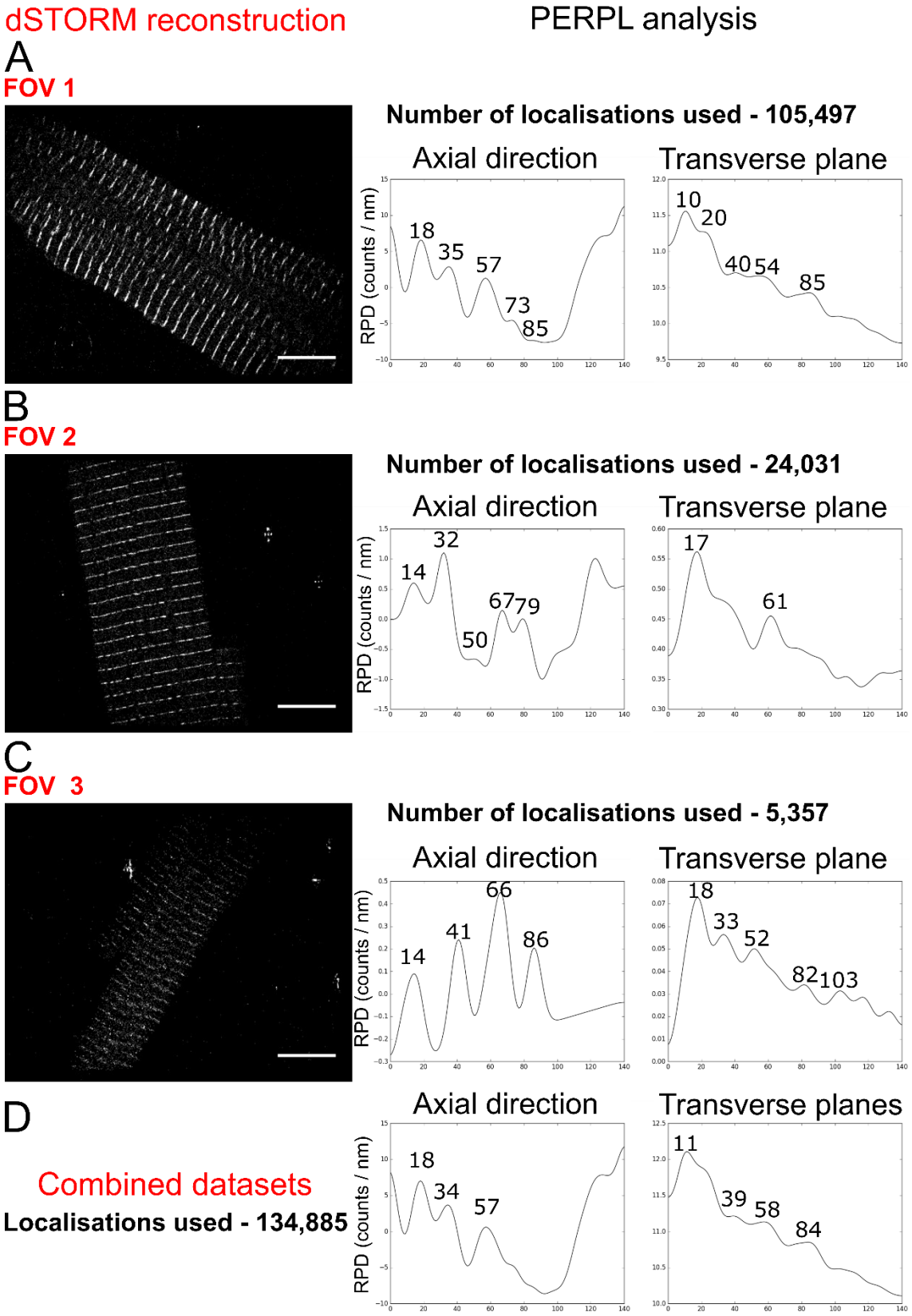

Figure 4.5 – PERLP analysis of dSTORM localisations datasets from cardiomyocytes labelled with α-Affimer 9. (**A**) FOV1, (**B**) FOV2 and (**C**) FOV3 - dSTORM reconstructions (100 nm binning) of cardiomyocytes labelled with Affimer 9 -AF 647 (1 in 500 dilution). Scale bars = 8 µm. RPD profiles using the localisation datasets of each FOV were generated for the axial direction and the transverse plane of the cell. (**D**) RPD profiles for the combined dataset from all three FOV. The numbers in each profile indicate the distance (nm) at the height of the RP D peaks.

4.3.3 Using PERPL to analyse the arrangement of the N-terminal Z1/Z2 domains of titin in the Z-discs of titin

dSTORM localisation datasets from three different FOVs of single cardiomyocytes labelled with Z-Affimer 12 were collected and PERPL analysis was used for the combined dataset (~ 12,600 localisations) (**Figure 4.6A and B**). The size of dSTORM localisation datasets for each FOV were small (**Figure 4.2B**). Only 2-3 acquisitions were collected for each field of view before the AF647 dye population was bleached. This could be due to poor labelling efficiency of the Z-Affimer 12. Alternatively, this could be due to a lower number of available binding sites, there are thought to be only two Z1/Z2 domains per actin filament in the Z-discs compared to twelve α-actinin molecules. Despite this, a pattern was observed in the 3D RPD histogram generated (**Figure 4.6A**)**.** Similar to the α-actinin RPD histogram (**Figure 4.4A**), weak to no RPD signal past 100 nm. The 1D transverse planes RPD profile shows high RPD at 24, 49, 75 and 107 nm (**Figure 4.6B**) suggesting regular spacing of ~ 25 nm between Z1/Z2 domains of titin from the same sarcomere. It could be argued this is the same as the lattice spacing of the actin filaments. The 1D profile in the axial direction shows high relative position density above background at 20, 33, 63, 84 and 100 nm. This suggest the Z1/Z2 domains are not only at the edges of the Z-discs but are arranged throughout the Z-disc in the axial direction with no clear ordered arrangement. The relative positions of 100 nm could be the spacing between Z1/Z2 domains at the edges of the Z-discs and the relative positions of 20 nm could be Z1/Z2 domains positioned 10 nm from the centre. From the data here it is unclear if titin is anchored at different positions the Z-discs in the axial direction or titin filaments capable of sliding in the Z-discs. However, a larger dataset would needed to better answer this question.

It is thought that the Z1/Z2 domains of two titin molecules from the same sarcomere are crosslinked in a palindromic complex at the end of the actin filaments (**Zou *et al.* 2006**). The crystal structure of Z-Affimer 12 bound to the Z1/Z2 domains has yet to be solved. If two Z1/Z2 domains molecules are bound to telethonin (2:1 ratio) in cardiomyocytes in a palindromic complex the furthest distance the Z-Affimer 12 can be from each other is 11 nm (measured between the two Z2 domains in the Z1/Z2 : telethonin crystal structure, **PDB code 1YA5**, **Zou *et al.* 2006**). The transverse profile does show a high above background RPD at 5 nm (**Figure 4.6B**), which may correspond to the spacing of Z1/Z2 domains cross-linked by telethonin. However common relative positions below 20 nm were not seen in the axial profile. There could be due to Z-Affimer 12 only binding to one Z1/Z2 domain per complex or the spacing between two Z1/Z2 domains bound to telethonin is too small for the relative positions to

be resolved. Alternatively, the 2:1 ratio Z1/Z2 to telethonin seen in the crystal structure may not occur *in vivo*. Assuming the Z1/Z2 domains of two titin filaments from the same sarcomere are cross-linked by telethonin, the relative positions shown in the RPD axial plots are likely to be between titin filaments from adjacent sarcomeres separated at the most by 10 nm in the transverse plane. The N-terminal domains of titin from the same sarcomeres are spaced too far away from each other in the transverse plane (~ 25 nm) for the relative positions of the Z1/Z2 localisations to be seen in the axial RPD plot.

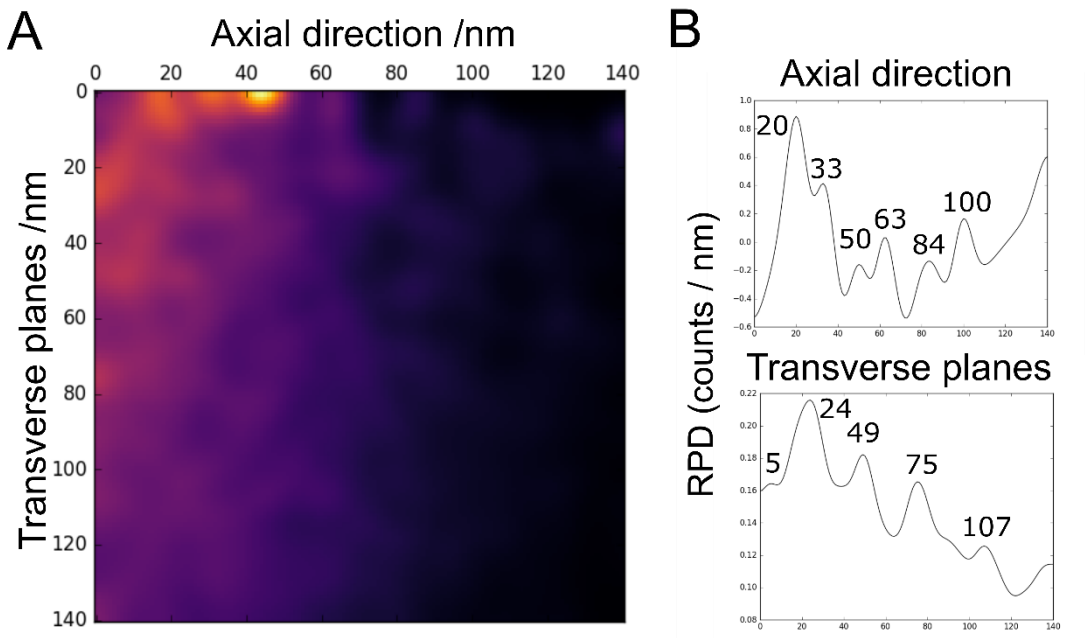

Figure 4.6 – PERPL analysis of combined titin Z1/Z2 domains dSTORM localisation datasets. (**A**) 2D representation of the Z1/Z2 domains 3D relative position density histogram. (**B**) 1D relative position density profiles for the axial direction and in the transverse planes from the RPD histogram.

PERPL analysis was also used for the individual FOV dSTORM datasets which make up the combined dataset, to gauge if there are any variations between the different cardiomyocytes (**Figure 4.7A, B and C**). Like PERPL analysis of the α-actinin dSTORM dataset it is clear the 1D RPD profiles of the combined dataset is most influenced by the FOV with the largest dataset, in this case FOV 2 (~ 7,000 localisations). It could be argued that the other fields of views (FOV 1 and 3) also show the 25 nm spacing pattern clearly seen in the FOV 2 transverse planes profile, however not as well. Interestingly the axial profile for FOV 3 (**Figure 4.7C**) shows high RPD at 17 and 100 nm. Also, the highest RPD for the FOV 1 in the axial profile is at 6 nm, which is not seen in the other fields of view. This may correspond to the spacing between two Z1/Z2 domains crosslinked by telethonin. However, with the small dataset sizes it is unclear if the patterns seen in the 1D profiles are common Z1/Z2 relative positions or simply background noise. Further Z1/Z2 localisations need to be collected to reliably determine the spacing of the N-terminal domain titin in the Z-discs.

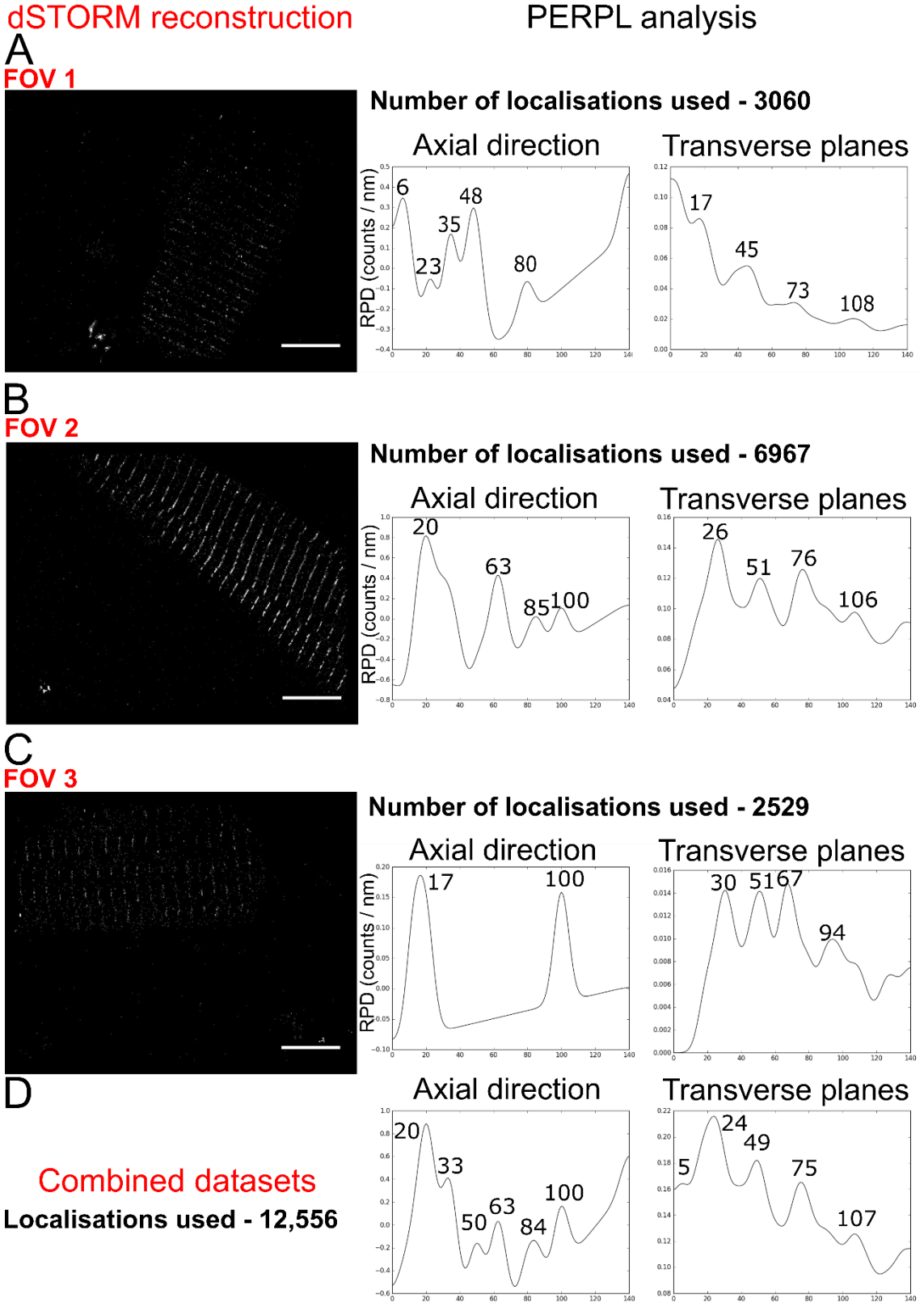

Figure 4.7 – PERLP analysis of dSTORM localisations datasets from cardiomyocytes labelled with Z-Affimer 12. (**A**) FOV1 - dSTORM reconstruction (100 nm binning) of a cardiomyocyte labelled with Z-Affimer 12 -AF 647 (1 in 1500 dilution). (**B**) FOV2 and (**C**) FOV3 - dSTORM reconstructions (100 nm binning) of cardiomyocytes labelled with Z-Affimer 12 -AF 647 (1 in 500 dilution). Scale bars = 8 µm. RPD profiles using the localisation datasets of each FOV were generated for the axial direction and the transverse plane of the cell (nm). (**D**) Relative position density (RPD) profiles for the combined dataset from all three FOV. The numbers in each profile indicate the distance (nm) at the height of the RPD peaks.

4.4 Discussion

One of the aims of this chapter was to determine if dSTORM is a suitable technique to reliably show the arrangement of proteins within the Z-discs of cardiomyocytes. From EM studies, the arrangement of α-actinin molecules is well understood. α-Affimer 9 directly linked to AF647, which binds α-actinin, was used to label adult rat cardiomyocytes and imaged by dSTORM. From the dSTORM reconstructions alone, it was difficult to determine the arrangement of α-actinin due to the localisation precision of the dataset and the labelling efficiency of α-Affimer 9. Therefore, only a sub-set of dSTORM localisations (5 nm localisation precision cut-off, **Figure 4.2A**) was used for further PERPL analysis to look for common spacing between localisations. In the axial direction (along the actin filaments) repeat spacing of 19.2 nm was expected. The RPD profiles in the axial direction (**Figure 4.4B**) did show regular spacing along the actin filaments. Also, the RPD profiles of the transverse plane did show the spacing of ~20 nm, possibly following the lattice spacing of the Z-disc. Also, FOV1 (**Figure 4.5A**) showed the relative positions for ~10 nm, the distance between two actin binding domains in one α-actinin layer bound to the same actin filament or the distance between actin binding domains of opposing actin filaments.

The results from the dSTORM/α-Affimer 9 localisation dataset show the potential for the use of dSTORM with PERPL analysis for the arrangement of Z-discs protein in cardiomyocytes. From the analysis of α-actinin localisations in this chapter, it is clear that good labelling of the cardiomyocyte with the Affimer is key. dSTORM imaging of one well labelled sample as in FOV1 (**Figure 4.5A**) reliably showed the arrangement of α-actinin. Why one field of view showed better labelling with the Affimer however the other is unclear. The localisation precision cut-off used for PERPL analysis used in this work was 5 nm, to retain a larger proportion of the dataset. As a result, the spacing of α-actinin less than 10 nm apart were not observed. Also, any heterogeneity in α-actinin arrangement caused by the heterogeneity in Z-disc lattice conformations was not observed. For analysis of Z-discs proteins in the future, a larger dataset would need to be collected and a smaller precision localisation cut-off (e.g. 2 - 3 nm) could be used for PERPL analysis to give a more detailed view of the arrangement of proteins in the Z-discs.

With dSTORM successfully showing the arrangement α-actinins, the same procedure was used to analyse the arrangement of the N-terminal domains of titin (Z1/Z2) in the Z-discs of cardiomyocytes. PERPL analysis of dSTORM/Z-Affimer 12 localisation data clearly showed regular 25 nm spacing of Z1/Z2 domains from the same sarcomere in the transverse directions of the Z-disc lattice (**Figure 4.6B**), consistent with its organisation following that of the actin filaments. However, the α-actinin dSTORM suggested actin lattice spacing of 20 nm. To more confidently determine the actin filament lattice spacing in the Z-discs, the same dSTORM protocol can be used for the actin capping protein CapZ. It was previously suggested that the N-terminal end of titin only localised at the edges of the Z-discs (**Gregorio *et al.* 1998**). Here dSTORM and PERPL analysis shows the Z1/Z2 domains are distributed throughout the Z-disc not the edges, supporting what was seen by immuno-EM in another study (**Gautel *et al.* 1996**). Moving forward a larger dataset is required for a more comprehensive analysis. The dSTORM dataset used here (**Figure 4.2B**) was very small and so the localisation precision of the dataset analysed was ≤ 5 nm. Also, it would be interesting to see if using the dSTORM/PERPL analysis technique for telethonin shows the same arrangement in the Z-discs as the Z1/Z2 domains. From the work in this chapter, it is clear the use of Affimers with dSTORM is a viable technique to show the arrangement of proteins within the Z-disc and other organised structures within cells.

Chapter 5 - Characterising the mutations in the actin binding domain of α-actinin 2 associated with hypertrophic cardiomyopathy

5.1 Introduction

Familial hypertrophic cardiomyopathy (HCM) is a cardiovascular condition which could affect up 1 in 200 people in the population as the most prevalent genetic heart disorder (**Maron *et al.* 2015**). It is characterised clinically by hypertrophy of the left ventricular wall of the heart (thickness >13 mm). The genetic basis of the disease has been evaluated by the sequencing of genes encoding sarcomeric proteins, from individuals with HCM (**Theis *et al.* 2006**, **Chiu *et al.* 2010**, **Girolami *et al.* 2011**). From these studies, three point mutations located in the CH domains of α-actinin 2 have been identified, which may cause HCM by changing the properties of muscle α-actinins.

The mutation A119T in the α-actinin gene 2 was identified in individuals from an Australian family spanning three generations (**Chiu *et al.* 2010**). 23 individuals within the family across all generations had the g to a missense mutation resulting in the A119T mutation. The A119 residue is located on helix F in the CH1 domain (**Figure 5.1A**). The mutation G111V was identified in a single male individual diagnosed with HCM but with no prior family history of the disease (**Theis *et al.* 2006**). The G111 residue is located on the loop between helix E and F just proceeding helix E (**Figure 5.1A**). Both G111V and A119T mutations have been shown to cause reduced incorporation of α-actinin into the Z-discs and increased α-actinin aggregation in cardiomyocytes (**Haywood *et al.* 2016**). However how the mutations cause this mis-localisation is unclear.

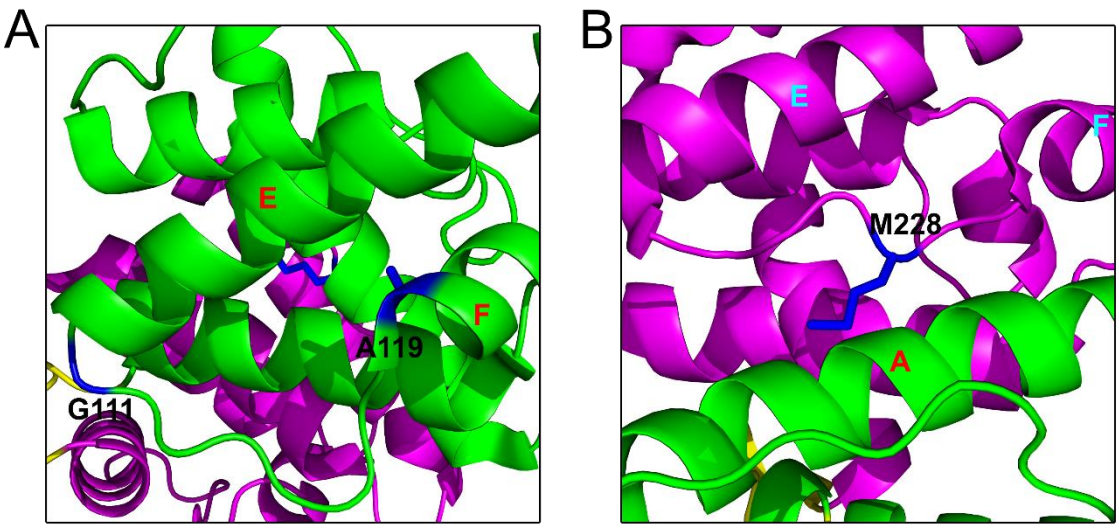

Figure 5.1 – Locations of α-actinin mutated residues linked to HCM.
(**A**) Residues G111 and A119 (blue) on the CH1 domain (green). (**B**) Residue M228 (blue) located at the interface between the CH1 (green) and CH2 (magenta) domains.

The mutation t683c (M228T) in the α-actinin gene 2 was identified in eighteen individuals from an Italian family spanning four generations with a range of autosomal dominant cardiomyopathic traits (**Girolami *et al.* 2011**). M228 is located on the loop between helices E and F of the CH2 domain with the residue inserted between helix A (CH1) and helix G (CH2), in the middle of the interface (**Figure 5.1B**). α-actinin 2 with this mutation has yet to be characterised *in vitro* or *in vivo* and therefore it is uncertain how the mutation contributes to the manifestation of HCM. However, mutations in α-actinins 1 and 4 located at the CH1-CH2 interface have regularly been found to increase filamentous actin binding affinity (**Lee *et al.* 2008, Weins *et al.* 2007, Murphy *et al.* 2016**), see section **1.4.2**. In the case of α-actinin 4, the mutations at the interface linked FSGS have been found to cause increase actin filament aggregation and α-actinin 4 mis-localisation (**Weins *et al.* 2007**).

The research in this chapter focusses on the three mutations located in the N-terminal CH domains of α-actinin 2, associated with hypertrophic cardiomyopathy; G111V, A119T and M228T. The effect of the mutations upon actin binding affinity were assessed by *in vitro* co-sedimentation assays of actin filaments and ABD constructs (19 – 269 residues) comparing the separate point mutations and the wild-type sequence. As M228 is located at the interface between the CH1 and CH2 domains, size exclusion of the M228T ABD construct was performed to determine if the “closed conformation” of the CH domains is altered by the methionine to threonine change.

5.2 Methods

5.2.1 Introduction of M228T mutation by site directed mutagenesis (SDM) of muscle

SDM was used to introduce the single point mutation, t683c (numbering using the full length human α-actinin 2 gene), into the cDNA sequence of wild type (WT) α-actinin 2 ABD within the vector pGEX-6p-1 (**General Methods Figure 2.1**). The forward and reverse primers designed,

5'- CTGGATATTCCTAAAA**C**GTTGGATGCTGAAGAC -3'
5'- GTCTTCAGCATCCAAC**G**TTTTAGGAATATCCAG -3'

are complementary to the same region in the wild-type α-actinin 2 gene sequence (nucleotides 667-669) apart from a single nucleotide (t683c, in bold). For whole plasmid PCR, KOD polymerase was used as it has high fidelity and processivity. The SDM PCR mixture contained; 10 µL 5x KOD polymerase buffer, 1 µL dNTP (10 mM stock), 1 µL forward primer (10 µM stock), 1 µL reverse primer (10 µM), 1 µL pGEX-6p-1 – ABD WT (10 ng μL^{-1}), 1 µL KOD Hot Start DNA polymerase (1.0 unit μL^{-1}, Merck 71086) and dH_20 to make the final volume 50 µL. The PCR parameters using a BioRad T100 thermocycler are as follows: Initial denaturation at 95 ºC for 1 min followed by 20 cycles of denaturation at 95 ºC for 50 secs, annealing at 60 ºC for 50 secs and extension 68 ºC for 5 mins 45 secs and finished with a final extension at 68 ºC for 7 mins.

After the PCR, the original template plasmid without the mutation was removed via a DpnI digest. 1 µL of DpnI (10 U μL^{-1}, Promega R6231) was added to the PCR mixture and incubated at 37 °C for 2 hrs. The whole plasmid PCR product was then transformed into NEB 5α cells (NEB, C2987I) (**General Methods 2.4**) for subsequent minipreps (**General Methods 2.5.4**). The purified plasmids were then sent for sequencing to confirm the presence of the mutation.

5.2.2 Expression and purification of mutant α-actinin 2 ABD WT, G111V, A119T and M228T

The construct pGEX-6p-1_ABD_M228T was generated by SDM outlined previously (**5.2.1**). The constructs pGEX-6p-1_ABD_G111V and pGEX-6p-1_ABD_A119T were kindly provided by Dr. Marcin Wolny. The ABD mutants were expressed using BL21(DE3) cells (NEB, C2527I) in 400 mL LB cultures with 0.5 mM IPTG at 37 ºC for 3 hrs. The ABD mutants were purified by the same methods as the wild-type ABD, first via glutathione affinity chromatography with a precision protease incubation step and followed by an anion exchange chromatography step. The full protocol for the purification of the α-actinin 2 ABD construct (residues 19 – 269) can be found in section **3.2.1**. The concentrations of the final 1 mL ABD mutant samples are as follows; ABD M228T ~ 10 µM, ABD G111V ~ 30 µM and A119T ~ 60 µM.

5.2.3 Actin preparation and polymerisation

Actin was purified from rabbit skeletal muscle as described in **Pardee and Spudich 1982** and stored as globular actin (G-actin, ~100 µM) at -80 ºC in G-actin buffer (20 mM Tris–HCl, pH 8.0, 0.2 mM Na_2ATP, 0.2 mM $CaCl_2$, 0.5 mM mercaptoethanol) until use. For the co-sedimentation assays the G-actin was polymerised by adding 20 µL of exchange buffer (3 mM $MgCl_2$, 11 mM EGTA) to 200 µL of the G-actin sample and incubated on ice for 15 mins. This was followed by the addition of 20 µL of polymerisation buffer (300 mM KCl, 120 mM MOPs, 1 mM EGTA, 12 mM $MgCl_2$, and 1 mM DTT pH 7.0) and a further 2 hr incubation on ice. The filamentous actin was then dialysed in F-actin buffer (50 mM KCl, 10 mM MOPs, 1 mM EGTA, 1 mM $MgCl_2$, and 1 mM DTT pH 7.0) for 72 hrs at 4 ºC.

5.2.4 Co-sedimentation assays of actin filaments with WT, G111V, A119T ABD from α-actinin 2

In a volume of 200 µL, F-actin (5 µM) and mixtures of varying concentrations of ABD (2.5, 5, 10, 15, 20, 40 and 60 µM) were used. ABD samples were dialysed in F-actin buffer (50 mM KCl, 10 mM MOPs, 1 mM EGTA, 1 mM $MgCl_2$, and 1 mM DTT pH 7.0) before use in the co-sedimentation assays. Samples were incubated at room temperature for 1 hour before centrifugation in Beckman Coulter ultra-centrifugation tubes (7 x 20 mm, 343775). Samples were then centrifuged at a high speed (100,000 xg) in a Beckman optima TLX centrifuge (Beckman TLA100 rotor) for 1 hour at 24 ºC. The supernatants were then carefully separated from the pelleted actin. The pellets were resuspended in 200 µL 1x SDS sample buffer. The supernatant protein samples were precipitated using trichloroacetic acid (TCA) and resuspended in 200 µL 1x SDS sample buffer. All samples were subsequently boiled at 100 ºC before running on a

SDS-PAGE. 15 µL of each sample were loaded onto 12 % acrylamide/Bis-acrylamide gels and the gels were stained with Coomassie Blue after the electrophoresis run. The software package Image-Lab (Bio-Rad) was used to perform densitometry analysis of the bands on the gels after imaging. Control gels of both actin and ABD at a range of concentrations (1 - 60 µM) were also run and analysed for normalisation of the band intensity values obtained.

5.2.5 Co-sedimentation assay of actin filaments with wild-type and mutant M228T ABD from α-actinin 2

Filamentous actin (10 µM) was incubated with a fixed concentration of ABD (5 µM) in F-actin buffer (50 mM KCl, 10 mM MOPs, 1 mM EGTA, 1 mM $MgCl_2$, and 1 mM DTT pH 7.0), 200 µL volume in total. Three samples of actin with wild-type ABD were prepared and three with the ABD M228T mutant were prepared in Beckman Coulter ultra-centrifugation tubes (7 x 20 mm, 343775). Control samples were also prepared; WT ABD only (5 µM), WT M228T only (5 µM) and actin only (10 µM). All samples were incubated at room temperature for 30 mins. Samples were then centrifuged at a high speed (100,000 xg) in a Beckman optima TLX centrifuge (Beckman TLA100 rotor) for 1.5 hrs at 24 °C. The supernatants were carefully separated from the pelleted actin. The pellets were resuspended in 1x SDS sample buffer and the supernatants were diluted (1:1 volume) in 2x SDS sample buffer. All samples were subsequently boiled at 100 ºC before a SDS-PAGE run. 10 µL of each sample were loaded onto a Mini-PROTEAN® TGX™ Precast 4-20 % acrylamide/Bis-acrylamide gels (Biorad, 4561095) and the gels were stained with Coomassie Blue after the electrophoresis run. The software package Image-Lab (Bio-Rad) was used for the densitometry analysis of the bands on the gels after imaging.

5.2.6 Size exclusion of Wild-type and M228T α-actinin 2 ABD

A Tricorn 10/200 gp column (GE healthcare) packed with Superdex 75 resin attached to an ÄKTA Prime plus system was used for the size exclusion runs. 100 µL of protein samples were loaded onto the column for each size exclusion run. The WT and M228T ABD samples (each 10 µM) were in PBS for the runs and the column was equilibrated in PBS. During each run the UV absorbance was measured and the elution volume was taken as the top of the elution peak.

The molecular weight of the ABD species eluted off the column was estimated from runs using low molecular weight standards (Gel Filtration LMW Calibration Kit, GE healthcare, 28403841) (**Figure 5.2A**). The elution volumes for each protein standards (where the UV absorbance was highest) were recorded and the Kav was calculated.

Kav = (protein species elution volume – void volume) / (column volume – void volume)

The column volume was 14.1 mL and the void volume was measured by running dextran blue 2000 (1 mg mL^{-1}) down the column and recording the elution volume (5.79 mL). The Kav values of the standards were plotted against the logMW and a standard curve was plotted (**Figure 5.2B**). Using the standard curve, the estimated MW of the protein samples were calculated.

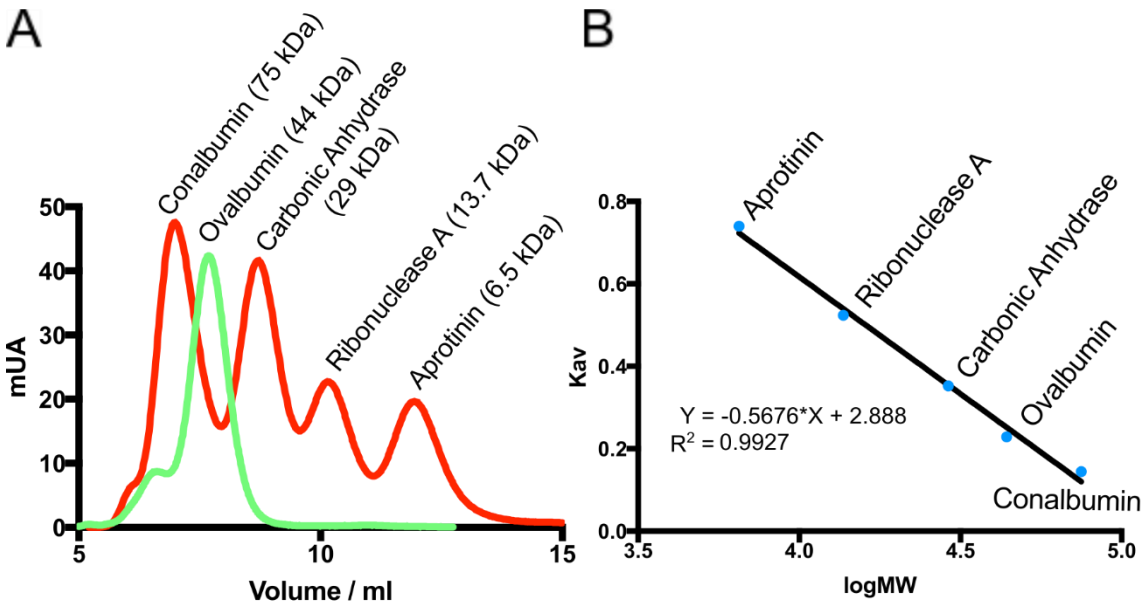

Figure 5.2 - Size exclusion runs using low molecular weight (LMW) standards (GE healthcare). LMW standards were ran through the tricorn 10/200 gp column (GE healthcare) packed with Superdex 75 Prep Grade (GE healthcare) attached ÄKTA Prime plus system. (**A**)The UV absorbance trace of a 100 µL sample containing conalbumin, carbonic anhydrase, ribonuclease A and aprotinin (each 3 mg mL^{-1}) in PBS (red line). A 100 µL sample of ovalbumin (4 mg mL^{-1}) in PBS was ran separately (green line) as suggested in the manufactures protocol. (**B**) The Kav values for each protein standard (calculated from the elution volumes) plotted against the logMW of the standards. A standard curve was plotted using the protein standards Kav and logMW values.

5.3 Results

5.3.1 Affinities of α-actinin 2 ABD mutants G111V, A119T, M228T and wild-type to filamentous actin

To assess how the point mutations change the binding affinity of α-actinin-2 to actin, co-sedimentation assays with filamentous actin and the mutant ABD constructs (ABD G111V and A119T) were compared to that for wild-type ABD constructs (**Figure 5.3**). For the co-sedimentation assays shown here (compared against the wild-type ABD), the Kd for ABD A119T increased ~2 fold and only increased by a small amount for ABD G111V. Neither mutant ABD showed a significant difference in affinity compared to the wild-type. Similar Kd values were reported in **Haywood *et al.* 2016** using the results shown here and three further repeats for each construct performed separately by Dr. Marcin Wolny. Across all human isoforms of α-actinin the mutations G111V and A119T are the first reported mutations located on the CH domains not to increase the actin binding affinity of α-actinin.

Due to poor expression of the ABD M228T construct, a fixed concentration of the wild-type and the M228T construct were pelleted with filamentous actin (1:2 molar ratio) to and compared (**Figure 5.4**). Although a Kd value could not be determined, there was a ~ 2 fold increase in the levels of ABD M228T pelleting with the actin compared to wild type ABD. This suggests a significant increase in actin binding affinity. This was not unexpected, as it follows a similar trend to that shown for other mutations at the CH1-CH2, which also increase binding affinity to actin (**Lee *et al.* 2008, Weins *et al.* 2007, Murphy *et al.* 2016**)

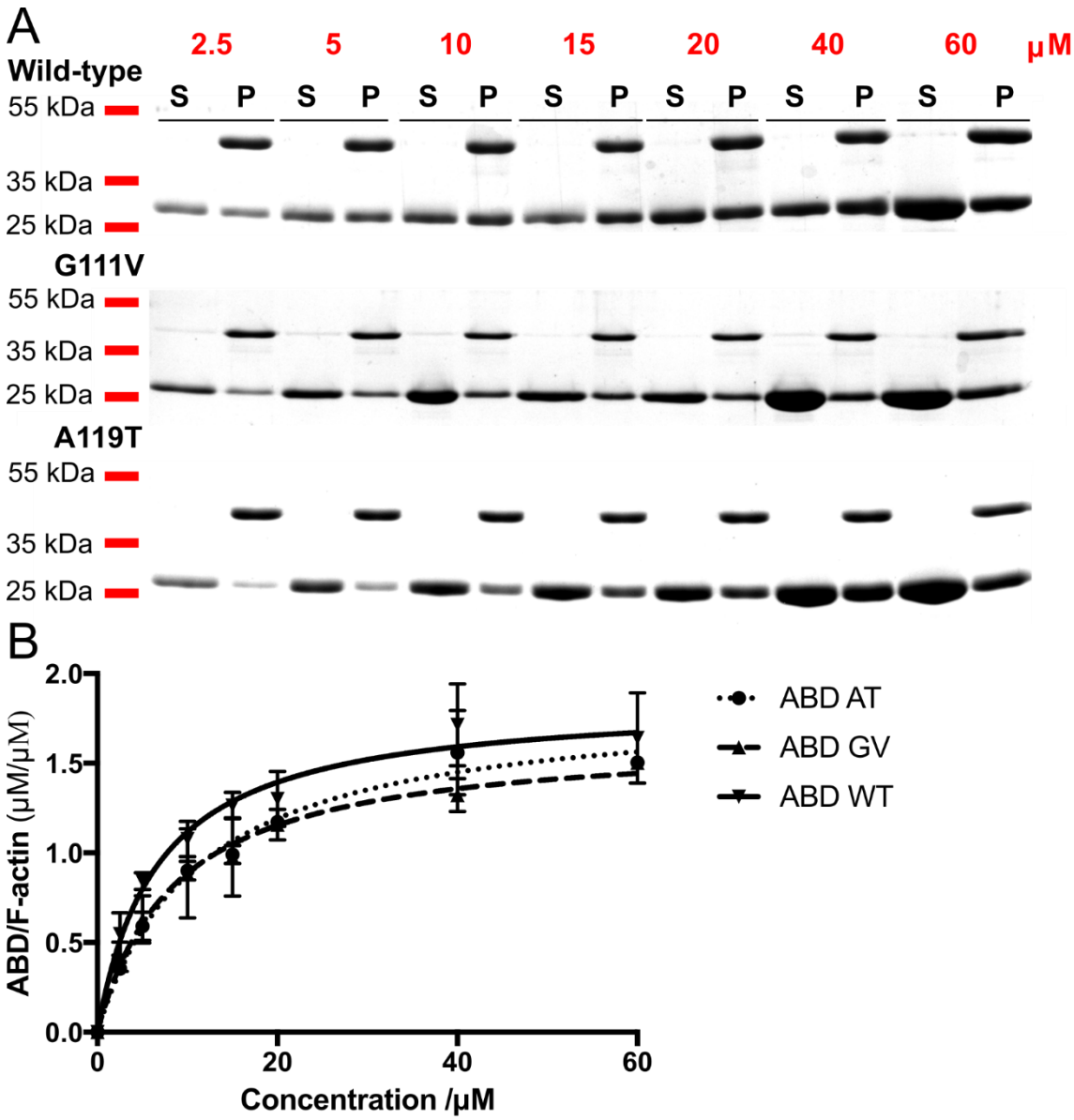

Figure 5.3 – Co-sedimentation assays of the ABD wild-type and the ABD mutants G111V and A119T with filamentous actin. (**A**) Example gels for the co-sedimentation assays for each ABD construct used. The ABD constructs (28.6 kDa) co-pelleted with actin (42 kDa) (P) and the supernatant samples (S) are shown for each ABD concentration (2.5 – 60 µM). (**B**) Binding curves for the wild-type (Kd = 6.6 µM +/- 1.7, n = 3) and the mutant constructs A119T (Kd = 11.1 µM +/- 2.0, n = 3) and G111V (Kd = 11.1 µM +/- 2.2, n = 2). Data points are the mean values of the repeat assays for each construct (error bars +/- S.E.M).

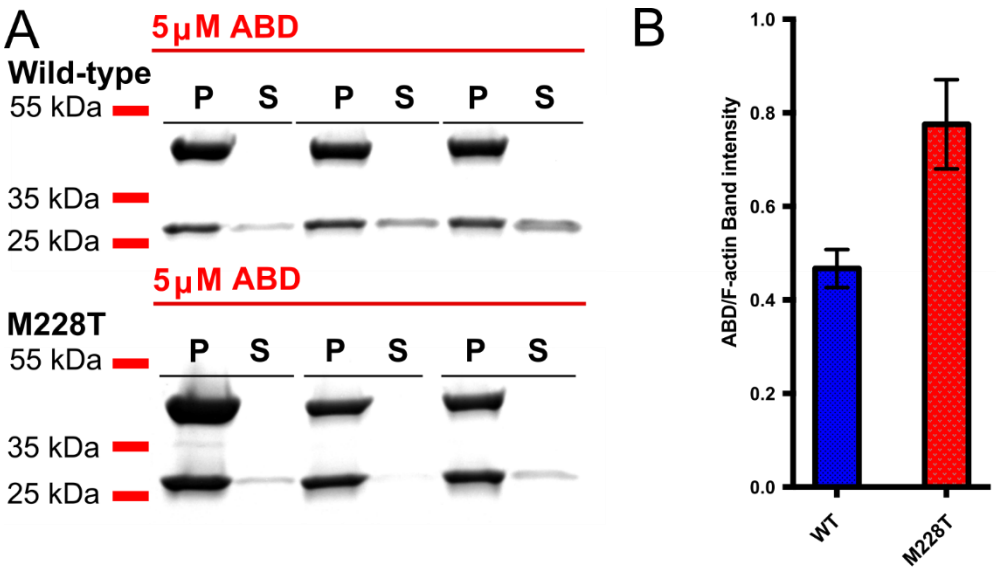

Figure 5.4 – Co-sedimentation assays of the ABD wild-type and the ABD mutant M228T with filamentous actin. (**A**) Example gels for the co-sedimentation assays for WT and M228T ABD constructs used. The ABD constructs (5 μM) (28.6 kDa) co-pelleted with actin (10 μM) (42 kDa) (P) and the supernatant samples (S) are shown for each repeat (n = 3). (**B**) Mean ratio of ABD to actin band intensities from the wild-type and M228T pelleted samples (n = 3, error bars = SD).

5.3.2 Analytical size exclusion of the α-actinin 2 ABD mutant M228T

Out the three known α-actinin 2 mutations located in the ABD linked to hypertrophic cardiomyopathy, M228T is the only mutation situated at the interface between CH1 and CH2 and ABD M228T has an increased affinity to actin. A conformational change from the closed conformation to a more extended conformation, whereby the CH1 and CH2 disassociate from one another, is thought to occur upon actin binding (**Lui *et al.* 2004, Franzot *et al.* 2005, Galkin *et al* 2010**). Size exclusion chromatography was used to evaluate if the ABD M228T mutant population adopts a more open, extended conformation compared to the wild-type. The UV absorbance elution profiles of wild-type ABD and the M228T ABD are almost identical (**Figure 5.5**). This suggests the overall conformation of the mutant construct is the same as the wild-type. It is also interesting to note the estimated MW for both constructs were ~ 34 kDa, an increase upon the real MW of 28.6 kDa similar to what was reported in section **3.3.3**.

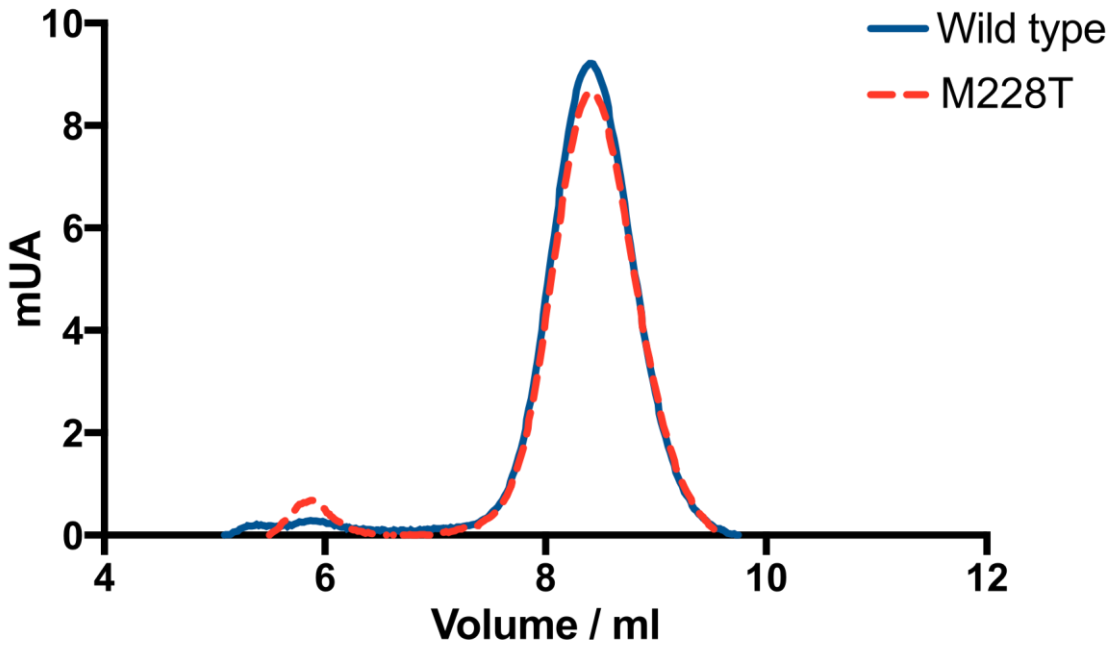

Figure 5.5- Size exclusion of the wild type ABD and M228T ABD constructs. The UV absorbance measured during the size exclusion runs for wild-type ABD (10 μM) and the mutant M228T (10 μM). The estimated MW of the wild-type (elution volume = 8.40 mL) and the M228T mutant (elution volume = 8.41 mL) were calculated to be ~ 34 kDa.

5.4 Discussion

Here the ABD A119T and G111V mutants were both found to not significantly reduce the binding affinity to actin compared to wild-type ABD. In adult rat cardiomyocytes, a reduced incorporation of mutant α-actinins, G111V and A119T, into the Z-discs was reported (**Haywood *et al.* 2016**). As the reduced affinity to actin of the mutants was not significant, it was suggested that the reduced incorporation into the Z-disc might the result of disruption to PIP_2 regulation of α-actinin (**Haywood *et al*. 2016**). The effects of the mutations in the CH domains upon the regulation of α-actinin 2 by PIP_2 have yet to be explored.

PIP_2 is thought to regulate the interaction of α-actinin 2 with the Z-repeats of titin (**Young and Gautel 2000**). After analysis of the ABD α-actinin 3 crystal structure, a triplet of arginines on the CH2 domain were proposed to act as a binding platform on the CH2 for the negatively charged PIP_2 head (R163, R192 and R169 on α-actinin 2) (**Franzot *et al.* 2005**). The mutations linked to HCM; G111V, A119T and M228T are not located near the arginine binding platform. Fluorescence anisotropy has been used with a shorter PIP_2 variant (PIP_2 - C6) and an α-actinin mutant construct, in which the triplet arginines were mutated to glutamates (**Ribeiro *et al.* 2014**). About a 50 % reduction in anisotropy signal was observed between the wild-type and the mutant construct indicating the importance of the arginines for PIP_2 binding. However, binding was not completely ablated suggesting other residues maybe involved. The mechanism for PIP_2 regulation has been proposed whereby the C-terminal EF 3-4 domain binds titin when PIP_2 disrupts the interaction between the EF 3-4 and the linker region of α-actinin (**Franzot *et al.* 2005, Ribeiro *et al.* 2014**). Molecular dynamic simulations show it is possible for the fatty acid chain of PIP_2 to reach the neck region when bound to the CH2 domain (**Ribeiro *et al.* 2014**). The role of the CH domain mutations in disrupting PIP_2 cannot be ruled out as the PIP_2 mechanism remains unclear. There is also precedence for mutations in the ABD altering the regulation of non-muscle α-actinins. Calcium has been shown to have no effect on the full-length α-actinin 4 affinity to actin with the K255E mutation, which is situated at the CH1-CH2 interface (**Weins *et al.* 2007**).

It could still be argued the mis-localisation of the α-actinin 2 mutants G111V and A119T outside of the Z-disc is the result solely of a weaker affinity to actin. The residue A119 is located on helix F of the CH1 domain. On the same helix are residues E120 and E121 (conserved in all isoforms of α-actinin) which have been hypothesised to form salt bridges with actin subunits, by molecular dynamic simulations (**Shams *et al.* 2016**). In

the ABD A119T crystal structure (**Haywood *et al.* 2016, PDB code 5A4B**), the T119 residue forms a hydrogen bond with N101 on helix E. This partial anchoring of helix F may not allow for the optimal orientation of helix F for actin binding, resulting in its reduced affinity. However, the involvement of E120 and E121 at the ABD : actin cleft interface has not been shown experimentally. Also, the glutamate pair is not well conserved in the spectrin family; human utrophin, dystrophin and filamin A all have a threonine and an aspartate positioned on helix F instead of the glutamate pair.

G111 is located on the loop between helix E and F, preceding helix E of the CH1 domain. The CMPT α-actinin 1 linked mutation V105I, a mutation to a larger hydrophobic residue has been shown to have an increased affinity to actin, however the exact Kd has not been determined (**Murphy *et al.* 2016**). The helix E and F region is conserved in all human α-actinins and the equivalent residue to V105 in α-actinin 2 is V112. Having two mutations next to each other, one increasing affinity to actin (V112I) and the other decreasing affinity (G111V), highlights the importance of the region for binding actin.

In vitro characterisation of the ABD M228T construct here has shown that this mutation increases binding to actin and does not result in a major change to the conformation to the CH domains. Single α-actinin 4 focal segmental glomerulosclerosis (FSGS) causing mutations at the interface have also been reported to increase the ABD affinity to actin whilst not changing the ABD conformation (**Lee *et al.* 2008**). It has been hypothesised these mutations disrupt interactions between the CH domains and lower the energy required for the transition between the closed and open conformations, resulting in the increased affinity to actin filaments. Without a solved crystal structure of the ABD with the M228T mutation it is unclear if the methionine to threonine mutation disrupts contacts at the interface. Further characterisation of the role of M228T in the manifestation of HCM is required, especially to determine how the mutant α-actinin localises in striated muscle and how the Z-discs are altered.

Chapter 6 – Final Discussion

6.1 Using dSTORM with PERPL analysis to study protein arrangement in the Z-disc

A main objective of this project was to determine if dSTORM is a viable technique for determining protein arrangement of Z-disc proteins. dSTORM has the reported resolution (20 nm in the x,y plane, 50 nm in the z-direction) (**van de Linde *et al.* 2011**) and therefore has the capability to acquire localisation information for proteins within the Z-disc regions. The models of the Z-discs from previous electron microscopy and tomography studies have yet to reach a resolution to determine the arrangement of most Z-disc proteins apart from the α-actinin links between actin filaments. Here, the dSTORM reconstructions of the cardiomyocytes labelled with either α-Affimer 9 or Z-Affimer 12 showed localisation data within the Z-disc regions of the cardiomyocytes (see **4.3.1**). Therefore confirming, localisation information within the Z-discs can be obtained using dSTORM. However, from the dSTORM reconstruction of a single field of view alone the arrangement of α-actinins and the Z1/Z2 domains could not be determined. This was for two reasons; (1) the labelling efficiency of Affimers were not 100 % and the localisation precision of the dSTORM dataset varied (see **Figure 4.2**). Further PERPL (patterns extracted from relative positions of localisations) analysis of the dSTORM dataset was required to analyse the arrangement of the Z-disc proteins. PERPL analysis was used to analyse the distances between pairs of localisations (relative positions) to visualise the arrangement of proteins *in vivo* (see **4.2.3**). 100 % Affimer labelling efficiency is not required and localisation datasets from different fields of view can be combined for PERPL analysis. Also, only localisations with a localisation precision of ≤ 5 nm was used for used for further PERPL analysis as common relative positions could be reliably observed whilst retaining a majority of the dataset.

Studying the arrangement of α-actinins in cardiomyocytes using dSTORM with PERPL analysis in chapter 4 has shown it to be a promising technique for determining the arrangement of regularly spaced proteins in the Z-discs. The relative position density histogram of the α-actinin localisation dataset showed high relative position density (above background) in the axial direction at 18 nm. From EM studies, α-actinins are thought to be regularly spaced every 19.2 nm along the actin filament in the axial direction. The arrangement of α-actinins observed from EM studies and the arrangement observed by dSTORM with PERPL analysis are within ~ 1 nm of each other. Also, the PERPL analysis of the α-actinin dSTORM dataset suggests regular spacing of 20 nm in the transverse plane. Previous EM studies have put the lattice

spacing of the Z-disc in the small square lattice conformation at ~ 20 nm (**Goldstein *et al.* 1989**). It can be suggested the arrangement of α-actinin actin binding domains bound to actin also follow the lattice spacing of 20 nm from the final RPD histogram.

However, this technique can be improved upon to better show arrangement of proteins in densely packed Z-disc regions. It can be argued larger dSTORM localisation datasets, than those used in chapter 4, are required. In chapter 4 the 1D RPD axial profile generated from the α-actinin localisation dataset did show the repeat spacing of 18 nm, with three distinct peaks above background (see **Figure 4.4B**). However, five peaks of high RPD above background representing the spacing between six layers of α-actinin bound to actin were expected in the 1D axial profile. This could be the result of having fewer relative positions between the α-actinins spaced further apart in the dataset. This is one case where more prominent common relative positions in the dataset are more easily observed above background in the final RPD histogram than other less prominent common relative positions. Therefore, the less prominent relative positions will only be seen in the final RPD histogram when using a larger dataset.

It can also be argued to better show the regular arrangement of proteins in the Z-disc, the localisation precision cap of the dSTORM dataset for PERPL analysis should be lowered below 5 nm. Using a 5 nm localisation precision cut-off, the repeat 18 nm spacing of α-actinins was observed in the axial direction. Also, in the case of the Z1/Z2 domains localisation dataset a regular 25 nm spacing was observed in the transverse plane (**see Figure 4.6B**). The two cases of using PERPL analysis in chapter 4 shows for the study of proteins regularly space ~ 20 nm or more apart, a localisation precision maximum of 5 nm is sufficient. However, there are limitations in the PERPL analysis when using a 5 nm localisation precision cut-off. If the proteins of interest are arranged less than 5 nm apart from each other, the arrangement may not be seen in the final RPD histogram. For example, a high RPD representing the spacing between a pair of ABD in the same layer (~ 2.74 nm, **Figure 4.4B**) was not seen in the α-actinin RPD histogram (in the axial direction). Also, if the proteins of interest have different spacing of a similar distance (within 5 nm of each other), the different spacing may not be distinct from one another in the final RPD histogram. For example, a high RPD at ~ 10 nm in the transverse plane of the α-actinin RPD histogram. This may correspond to both the spacing of actin binding domains in a single α-actinin layer bound to the same actin filament and the spacing of actin binding domains bound to adjacent actin filaments because they are thought to be similar distances. It is also known the Z-discs has two different lattice conformations, the basket weave and small-square lattice, with

different lattice spacing. The α-actinin transverse plane RPD did not suggest the presence of two different lattice spacings, only a 20 nm spacing. Lowering the localisation precision cap may also reduce the background in the final RPD histogram. A high RPD background could be seen in the α-actinin RPD histogram (**Figure 4.4A**). The background could be attributed to mis-localisation of the Affimer, auto-fluorescence of the cardiomyocyte and poor localisation precision of the dataset. Therefore, the background seen in the α-actinin RPD histogram could be reduced by lowering the localisation precision cut-off. Lowering the localisation precision cut-off would however reduce the number of usable localisations for PERPL analysis. Therefore, again a larger localisation dataset would be required. To generate the dSTORM localisation dataset required many fields of view of labelled cardiomyocytes would need to be imaged and combined for PERPL analysis.

6.2 Using other microscopic techniques for studying the arrangement of Z-disc proteins

6.2.1 Multi-colour dSTORM

In the future, multi-colour dSTORM (**van der Linde *et al.* 2009**) with PERPL analysis can be used to obtain localisation information of two different Z-discs protein within the same cell. Interpretation of the final RPD histogram from single colour dSTORM to understand the arrangement of a specific protein can be difficult. For example, in chapter 4 the spacing of α-actinin in the transverse planes was shown to be ~ 20 nm which was thought to follow the actin filament lattice spacing in the Z-discs. Whilst the spacing in the transverse planes of the Z1/Z2 domains was shown to be ~ 25 nm. It is unclear if the Z1/Z2 domains have a different spacing to the actin filament lattice spacing or the difference observed is due to the cell variation or the small Z1/Z2 domains localisation dataset used. As discussed in chapter 4, the actin capping protein CapZ would be a good candidate protein for studying the lattice spacing. Multi-colour dSTORM can be used to obtain localisation information for the CapZ protein and either α-actinins or the Z1/Z2 domains from the same cardiomyocyte. The comparison of the arrangement of CapZ with the arrangement of either α-actinin or the Z1/Z2 domains can determine if these proteins are following the actin lattice spacing. Likewise, multi-colour dSTORM can be used to obtain localisation information for α-actinins and the Z1/Z2 domains in the same cell to compare the transverse spacing of the two proteins. The main disadvantage of this technique is that to discount any cellular variation only the localisation information from a single field of view could be used. This would limit the size of the dataset used for PERPL analysis. The labelling efficiency of the molecular probes (e.g. Affimers) would be required to be high. Also, different

molecular probes and fluorescent dyes would be used for each target protein. As a result, the size of the localisation datasets to be compared by PERPL analysis would be different. If the datasets are significantly different they cannot be reliably compared.

6.2.2 Photoactivated localisation microscopy

Photoactivated localisation microscopy (PALM) is another viable super-resolution fluorescence microscopy technique to use to study the arrangement of proteins *in vivo*. The single molecule localisation principle of PALM is the same as dSTORM however PALM imaging uses photo-switchable fluorescent fusion proteins (**Betzig *et al.* 2006**) instead of stochastically activated fluorescent dyes. Therefore, PALM can also be used to gain localisation information within the Z-discs which can be used for further PERPL analysis. It can be argued dSTORM is the more suitable technique for studying Z-disc protein arrangement. From using dSTORM to study the arrangement of α-actinins and Z1/Z2 domains, it is clear having a high localisation precision dataset is vital for determining the arrangement of closely spaced Z-disc proteins. Localisation precision is dependent upon the number of photons emitted from a fluorophore (**see 4.2.3**). Fluorescent fusion proteins emit fewer photons than commercially available fluorescent dyes (**Moerner 2012**) and therefore the localisation precision for a PALM localisation dataset would be lower compared to a dSTORM localisation dataset.

6.2.3 Electron tomography

The resolution of the current models of the Z-disc generated by EM generated have yet to reach a resolution to determine the arrangement of most Z-disc proteins. The most recent model of the Z-disc small square lattice structure generated by electron tomography with sub-tomographic averaging came to an 8 nm resolution (**Burgoyne *et al.* 2015**). However, with the advancement in electron microscopes, detection and image processing it is now possible to produce higher resolution models by electron tomography. Whether models of the Z-disc generated can reach a resolution so that density in the model can be identified as specific Z-disc proteins, remains to be seen. Also, sub-tomographic averaging would be required to generate a high-resolution model with the assumption all the sub-tomographs are homogenous. Therefore, any variation between sub-tomograms would be lost. As shown with α-actinin arrangement in chapter 4, electron tomography and super-resolution fluorescence microscopy can be used in tandem with each other to support and verify any Z-disc arrangements concluded by either technique.

6.3 Using dSTORM and PERPL analysis to study protein arrangement in other cellular structures

The work in chapter 4 has shown the capability of dSTORM with PERPL analysis to study the arrangement of Z-disc proteins in cardiomyocytes. However, dSTORM with PERPL analysis is not limited to the study of the arrangement of Z-disc proteins and can be used to study the arrangement of other regularly spaced protein *in vivo*. As shown in chapter 4, PERPL analysis is highly suited to study the arrangement of proteins in striated muscle cells. The cytoskeleton throughout striated muscle cells is highly ordered with bundles of myofibrils running the length of the cell. Therefore, all the localisation information throughout the cell can be used and localisation information from different cells can be easily combined by aligning the dSTORM reconstructions. (**see methods 4.2.3**). The same methodology shown in chapter 4 can also be used to study the arrangement proteins in other regions of the sarcomeres within striated muscle cells.

The cytoskeleton structures of other cell types are not as highly organised as striated muscles cells. However highly ordered sub-cytoskeletal structures have been reported, for example the microtubule assembly of primary cilia, and PERPL analysis can also be used to study protein arrangement within these sub-structures. In these cases, however dSTORM data collection and PERPL analysis could be more time consuming compared with using the techniques to study Z-disc protein arrangement. As the localisation collected during dSTORM imaging are confined to sub-structures more fields of may need to be imaged to be collect enough localisation data for reliable PERPL analysis. Also, rather aligning the whole cell for the combination of localisation dataset each sub-cytoskeletal structure would need to be individually aligned.

6.4 Affimers as molecular probes for super-resolution fluorescent microscopy

6.4.1 Using α-Affimer 9 and Z-Affimer 12 to label cardiomyocytes for dSTORM imaging shows the potential of Affimers for super-resolution imaging

Another objective of this project was to determine if Affimers are a viable option as molecular probes for super-resolution fluorescent microscopy. One advantage of using Affimers as molecular probes over immunoglobin based probes such as antibodies and nanobodies is the fast generation of Affimers which can bind specific targets. Using a phage display assay with an Affimer phage library allows for the fast generation of specific Affimer binders. Using this approach eight unique Affimer binder sequences for the ABD of α-actinin and seven Affimer sequences for the Z1/Z2 domains of titin were generated in this project. However, it is uncertain if the Affimer binders can be reliably generated by the *in vitro* phage display assay to be used as molecular probes *in vivo*. However, in this work three of the eight α-Affimers and four of the seven Z-Affimers were found to bind their target *in vivo*. Therefore, in the future there is promise that Affimers generated to bind other Z-disc proteins by phage display assays can be used as molecular probes for fluorescence microscopy.

Another key advantage over of Affimers over other molecular probes available is their small size (~ 12.5 kDa, ~ 3 nm in linkage error). It can be suggested that because of the size of the Affimers, they are more capable of penetrating dense networks of proteins than larger molecular probes, such as antibodies. In this project dSTORM imaging of the cardiomyocytes labelled with α-Affimer 9 and Z-Affimer 12 showed localisations throughout the densely packed Z-disc regions. Further PERPL analysis of localisation information from cardiomyocytes labelled with α-Affimer 9 and Z-Affimer 12 suggest a high labelling efficiency of the Affimers. The 1D relative position density profile in the axial direction from a α-Affimer 9 labelled cardiomyocyte (single field of view FOV1, **Figure 4.5A**) showed five peaks above background. This suggest that α-Affimer 9 was capable of binding all six α-actinin layers bound to actin in the Z-discs. Likewise, the regular 25 nm spacing observed in the transverse planes 1D RPD profile from a single Z-Affimer 12 labelled cardiomyocyte (FOV 2, **Figure 4.7B**) suggests ahigh labelling efficiency of Z-Affimer 12. dSTORM imaging of cardiomyocytes with PERPL analysis has shown the capability of Affimers to bind their respective targets in the dense Z-disc network.

For super-resolution fluorescence imaging Affimers are the preferred molecular probes to antibodies due to their smaller size. However, the same dSTORM imaging of cardiomyocytes labelled with antibodies generated to bind the same Z-disc proteins has yet to be performed. Without direct comparison of the different probes it cannot be determined if Affimers have a better labelling efficiency than antibodies in the Z-discs. Also, as discussed in the previous section (**6.1**) large dSTORM localisation datasets are required for PERPL analysis, therefore a high labelling efficiency of the Affimer *in vivo* is also required. A factor that can affect the labelling efficiency of an Affimer is the binding affinity of the Affimer to the target. As shown in chapter 3, the considerations in choosing α-Affimer 9 and Z-Affimer 12 for dSTORM imaging compared to the other candidates generated were: (1) If they could localise to the Z-discs *in vivo* and (2) the stoichiometry of the Affimers bound to their respective targets (by size exclusion). The binding affinity of the Affimers to their respective targets were not determined and were not a factor when the Affimers were chosen. In the future the binding affinities of α-Affimer 9 and Z-Affimer 12 should be determined, for example by isothermal calorimetry. Also, for future Affimers generated the binding affinities should be accessed before use as molecular probes to determine the best Affimer candidate.

6.4.2 Non-immunoglobulin binding protein alternatives as molecular probes for dSTORM

In this work it has been shown that Affimers are a promising alternative to antibodies for super-resolution fluorescence microscopy. There are other small non-immunoglobulin scaffold proteins available which can also be as molecular probes for super-resolution microscopy (reviewed in **Bedford *et al.* 2017**). Like Affimers, to be used as molecular probes they are required to be small for a reduced linkage error and are capable of binding their targets *in vivo*. As non-immunoglobulin scaffold proteins they would also be quick and inexpensive to produce. Two examples of small scaffold proteins which meet the criteria are Affibodies and Monobodies. Affibodies are the single 3-bundle helix “Z-domain” of immunoglobulin binding staphyloccal protein A with the residues involved in Fc binding altered to bind other target proteins (**Nord *et al.* 1997**). They are highly soluble, stable and they have no cysteines present in the sequence. Also, an anti-HER2 affibody has been used to visualise the localisation of HER2 (a transmembrane receptor tyrosine kinase) in SKBR3 breast cancer cell by fluorescence microscopy (**Peckys *et al.* 2015**). Affibodies (58 residues, ~ 6 kDa) (**Nord *et al.* 1998**) are smaller than Affimers (~12.5 kDa) and therefore would have a reduced “linkage error” and would more easily penetrate dense cytoskeleton networks. Affibodies have two binding sites; one on the surface of helix one (7 residues) and the

other on helix two (6 residues). One advantage of Affimers over Affibodies is that the variable binding loops are separate from the scaffold backbone and therefore variable binding residues are less likely to affect the stability of scaffold. Also, the binding loops of Affimers (each 8/9 residues) (**Tiede *et al.* 2014**) are larger than the variable binding regions of Affibodies (13 residues), therefore a more diverse range of Affimers generated to bind a specific target.

Monobodies are based on the 10th fibronectin type 3 domain with a scaffold of seven β-strands and three binding loops (each ~ 5 residues) (**Koide *et al.* 1998**). Monobodies (94 residues, ~10 kDa) are of a similar size to Affimers, highly soluble, highly stable and they have no cysteines present in the sequence. Also, an anti-EphA2 Monobody has been used to visualise the localisation of EphA2 (a marker protein for various tumours) *in vivo* by fluorescence microscopy (**Park *et al.* 2015**). Monobodies have two different phage libraries; one where there is variability in the binding loops only (**Koide *et al.* 1998**) and another where there are also two variable binding sites (~ 3 residues) at the ends of the β-strands next to two of the binding loops (**Koide *et al.* 2012**). With two different binding libraries a more diverse range of Monobodies can be generated to bind a specific target, compared to other scaffold proteins such as Affimers.

6.5 The role of HCM mutations G111V, A119T and M228T in disrupting α-actinin 2 function in the Z-discs

In chapter 5 three mutations linked to hypertrophic cardiomyopathy (HCM), located within the actin binding domain (ABD) of α-actinin 2, were studied to see the mutations effect on the ABD affinity to filamentous actin. Compared to the ABD wildtype, the mutants G111V and A119T showed no significant change in actin affinity (**see 5.3.1**). However, the mutations G111V and A119T respectively have been found to cause α-actinin 2 mis-localisation *in vivo* (**Haywood *et al.* 2016**). Therefore, the mutations must disrupt the interaction between another binding partner of the ABD. It has been suggested the mutations may disrupt PIP_2 regulation of α-actinin 2, as PIP_2 is known to interact with the ABD (**Fukami *et al.* 1996, Ribeiro *et al.* 2014**). Therefore, the next step would be to determine if mutations G111V and A119T disrupts the interaction between PIP_2 and the ABD. The main binding site for the PIP_2 has been proposed to be a triplet of arginines (R163, R192 and R169) on the CH2 domain (**Franzot *et al.* 2005**) and the importance of these residues for PIP_2 binding has been verified by fluorescence anisotrophy (**Ribeiro *et al.* 2014**). A similar experiment can be used to determine if the mutant ABD constructs perturb the ABD : PIP_2 interaction. If it is found that the mutations do not disrupt the PIP_2 interaction, the mutations may disrupt

the binding of another unknown binding partner of the ABD resulting in the mis-localisation *in vivo* observed.

The mutation M228T on the other hand was shown to significantly increase the affinity of the ABD to filamentous actin compared to the wild type construct (**see 5.3.1**). As discussed in Chapter 5 the M228 residue is located at the interface between the two calponin homology (CH) domains. Many other mutations (linked to disease in non-muscle α-actinins 1 and 4) are also located at the interface between the CH domains and have been shown to increase the binding affinity of the ABD to actin (**see 1.3.2**). It has been hypothesised (for α-actinin 4 mutations) the mutations cause the increased binding affinity as they disrupt contacts between the two CH domains and reduce the energy required for CH domain separation (**Lee *et al.* 2008**). M228 within the CH2 domain does not lie in any known actin binding site therefore it can be suggested, the increase binding affinity of the M228T ABD is also due to the disruption of contacts at the interface.

However, the actin binding ABD mechanism and the role of the CH2 domain, where M228 resides, is currently unclear. Previous AUC experiments of the wild type α-actinin 4 ABD have suggested the CH domains to be in a compact closed conformation when free in solution. This suggests the ABD initially binds to actin in a closed conformation. Here, size exclusion of the wild-type and M228T ABD α-actinin 2 constructs however suggests the ABD may be in a more open conformation when free in solution than previously thought. Further experimentation, such as AUC, is required to better analyse the conformation of the ABD from α-actinin 2 when free in solution. However, this suggests the ABD may be required to be in an open conformation to initially bind actin. Also, as there was no difference between wild-type and M228T constructs it can be argued the M228T does not play a role in disrupting contacts at the interface between CH domains. The highest resolution EM model (16 Å) of the α-actinin CH domains (**Galkin *et al.* 2010**) suggests in the final bound state the CH domains are in an open conformation with the CH1 domain bound to the filament and the CH2 either unbound to the filament or only very weak binding. This is further supported by a high-resolution model of the filamin A CH domains bound to actin (**Iwamoto *et al.* 2018**, 3.6 Å) which shows the ABD in an open conformation and the CH2 domain unbound to the actin filament. The ABD being in a final open state with the CH2 domain unbound to actin supports the hypothesis the mutation M228T increases binding affinity by lowering the energy required for the transition from a closed to an open conformation. As the role of the CH2 during the ABD binding mechanism is unclear the role of the M228 residue

also is unclear. To better understand the how the ABD of α-actinin interacts with actin and the role of the CH2 domain a high-resolution model of the CH domains bound to actin is required. As shown by the model of the CH domains of filamin A bound to actin (**Iwamoto *et al.* 2018**), a high-resolution model can be generated by electron microscopy. A model of the CH domain with the M228T mutation can also be generated to determine if the mutation alters the conformation of the final bound state.

References

Atkinson RA, Joseph C, Kelly G, Muskett FW, Frenkiel TA, Nietlispach D, Pastore A. 2001. Ca2+-independent binding of an EF-hand domain to a novel motif in the alpha-actinin-titin complex. *Nature Structural Biology* 8:853-857.

Bang ML, Gregorio C, Labeit S. 2002. Molecular dissection of the interaction of desmin and the C-terminal region of nebulin. *Journal of Structural Biology* 137:119-127.

Barua M, Brown EJ, Charoonratana VT, Genovese G, Sun H, Pollak MR. 2013. Mutations in the INF2 gene account for a significant proportion of familial but not sporadic focal and segmental glomerulosclerosis. *Kidney International* 83:316-322.

Bedford R, Tiede C, Hughes R, Curd A, McPherson MJ, Peckham, Tomlinson DC. 2017. Alternative reagents to antibodies in imaging applications. *Biophysical Reviews* 9:299-308.

Beggs AH, Byers TJ, Knoll JHM, Boyce FM, Bruns GAP, Kunkel LM. 1992. Cloning and characterization of 2 human skeletal-muscle alpha-actinin genes located on chromosome-1 and chromosome-11. *Journal of Biological Chemistry* 267:9281-9288.

Betzig E, Patterson GH, Sougrat R, Lindwasser OW, Oleych S, Bonifacino JS, Davidson MW, Lippincott-Schwartz J, Hess F 2006. Imaging intracellular fluorescent proteins at nanometer resolution. *Science* 313:1642-1645.

Borrego-Diaz E, Kerff F, Lee SH, Ferron F, Li Y, Dominguez R. 2006. Crystal structure of the actin-binding domain of alpha-actinin 1: Evaluating two competing actin-binding models. *Journal of Structural Biology* 155:230-238.

Bottega R, Marconi C, Faleschini M, Baj G, Cagioni C, Pecci A, Pippucci T, Ramenghi U, Pardini S, Ngu L, Baronci C, Kunishima S, Balduini CL, Seri M, Savoia A, Noris, P. 2015. ACTN1-related thrombocytopenia: identification of novel families for phenotypic characterization. *Blood* 125:869-872.

Bresnick AR, Janmey PA, Condeelis J. 1991. Evidence that a 27-residue sequence is the actin-binding site of ABP-120. *Journal of Biological Chemistry* 266:12989-12993.

Bresnick AR, Warren V, Condeelis J. 1990. Identification of a short sequence essential for actin binding by dictyostelium ABP-120. *Journal of Biological Chemistry* 265:9236-9240.

Broderick MJF, Bobkov A, Winder SJ. 2012. Utrophin ABD binds to F-actin in an open conformation. *Febs Open Bio* 2:6-11.

Burgoyne T, Morris EP, Luther PK. 2015. Three-Dimensional Structure of Vertebrate Muscle Z-Band: The Small-Square Lattice Z-Band in Rat Cardiac Muscle. *Journal of Molecular Biology* 427:3527-3537.

Buscher AK, Celebi N, Hoyer PF, Klein HG, Weber S, Hoefele J. 2018. Mutations in INF2 may be associated with renal histology other than focal segmental glomerulosclerosis. *Pediatric Nephrology* 33:433-437.

Chi RJ, Simon AR, Bienkiewicz EA, Felix A, Keller TCS. 2008. Smooth muscle titin Zq domain interaction with the smooth muscle alpha-actinin central rod. *Journal of Biological Chemistry* 283:20959-20967.

Chiu C, Bagnall RD, Ingles J, Yeates L, Kennerson M, Donald JA, Jormakka M, Lind JM, Semsarian C. 2010. Mutations in Alpha-Actinin-2 Cause Hypertrophic Cardiomyopathy A Genome-Wide Analysis. *Journal of the American College of Cardiology* 55:1127-1135.

Choi HJ, Lee BH, Cho HY, Moon KC, Ha IS, Nagata M, Choi Y, Il Cheong H. 2008. Familial focal segmental glomerulosclerosis associated with an ACTN4 mutation and paternal germline mosaicism. *American Journal of Kidney Diseases* 51:834-838.

Corrado K, Mills PL, Chamberlain JS. 1994. Deletion analysis of the dystrophin-actin binding domain. *Febs Letters* 344:255-260.

Crowley PB, Golovin A. 2005. Cation-pi interactions in protein-protein interfaces. *Proteins-Structure Function and Bioinformatics* 59:231-239.

Djinovic-Carugo K, Young P, Gautel M, Saraste M. 1999. Structure of the alpha-actinin rod: Molecular basis for cross-linking of actin filaments. *Cell* 98:537-546.

Fabbrizio E, Bonetkerrache A, Leger JJ, Mornet D. 1993. Actin dystrophin interface. *Biochemistry* 32:10457-10463.

Feng D, Steinke JM, Krishnan R, Birrane G, Pollak MR. 2016. Functional Validation of an Alpha-Actinin-4 Mutation as a Potential Cause of an Aggressive Presentation of Adolescent Focal Segmental Glomerulosclerosis: Implications for Genetic Testing. *Plos One* 11:*e*0167467.

Flood G, Kahana E, Gilmore AP, Rowe AJ, Gratzer WB, Critchley DR. 1995. Association of structural repeats in the alpha-actinin rod domain - alignment of inter-subunit interactions. *Journal of Molecular Biology* 252:227-234.

Frank D, Frey N. 2011. Cardiac Z-disc Signalling Network. *Journal of Biological Chemistry.* 286:9897-9904.

Franzot G, Sjoblom B, Gautel M, Carugo KD. 2005. The crystal structure of the actin binding domain from alpha-actinin in its closed conformation: Structural insight into phospholipid regulation of alpha-actinin. *Journal of Molecular Biology* 348:151-165.

Freiburg A, Gautel M. 1996. A molecular map of the interactions between titin and myosin-binding protein C – Implications for the sarcomeric assembly in the familial hypertrophic cardiomyopathy. *European Journal of Biochemistry* 235:317-232.

Fukami K, Furuhashi K, Inagaki M, Endo T, Hatano S, Takenawa T. 1992. Requirement of phosphatidylinositol 4,5-bisphosphate for alpha-actinin function. *Nature* 359:150-152.

Fukami K, Sawada N, Endo T, Takenawa T. 1996. Identification of a phosphatidylinositol 4,5-bisphosphate-binding site in chicken skeletal muscle alpha-actinin. *Journal of Biological Chemistry* 271:2646-2650.

Galkin VE, Orlova A, Salmazo A, Djinovic-Carugo K, Egelman EH. 2010. Opening of tandem calponin homology domains regulates their affinity for F-actin. *Nature Structural & Molecular Biology* 17:614-616.

Galkin VE, Orlova A, VanLoock MS, Rybakova IN, Ervasti JM, Egelman EH. 2002. The utrophin actin-binding domain binds F-actin in two different modes: implications for the spectrin superfamily of proteins. *Journal of Cell Biology* 157:243-251.

Gautel M, Goulding D, Bullard B, Weber K, Furst DO. 1996. The central Z-disk region of titin is assembled from a novel repeat in variable copy numbers. *Journal of Cell Science* 109:2747-2754.

Gimona M, Djinovic-Carugo K, Kranewitter WJ, Winder SJ. 2002. Functional plasticity of CH domains. *Febs Letters* 513 :98-106.

Girolami F, Iascone M, Bardi S, Berti L, Pezzoli L, Baldini K, Tomberli B, Servettini E, Torricelli F, Cecchi F. 2011. A novel mutation in alpha-actinin-2 responsible for hypertrophic cardiomyopathy identified by massively parallel next generation sequencing. *European Heart Journal* 32:272-272.

Goldstein MA, Michael LH, Schroeter JP, Sass RL. 1986. The z-band lattice in skeletal-muscle before, during and after tetanic contraction. Journal of Muscle *Research and Cell Motility* 7:527-536.

Goldstein MA, Michael LH, Schroeter JP, Sass RL. 1989. 2 structural states of z-bands in cardiac-muscle. *American Journal of Physiology* 256:552-559.

Gregorio CC, Trombitas K, Centner T, Kolmerer B, Stier G, Kunke K, Suzuki K, Obermayr F, Herrmann B, Granzier H, Sorimachi H, Labeit S. 1998. The NH2 terminus of titin spans the Z-disc: Its interaction with a novel 19-kD ligand (T-cap) is required for sarcomeric integrity. *Journal of Cell Biology* 143:1013-1027.

Gueguen P, Rouault K, Chen JM, Raguenes O, Fichou Y, Hardy E, Gobin E, Pan-petesch B, Kerbiriou M, Trouve P, Marcorelles P, Abgrall JF, Le Marechal C, Ferec, C. 2013. A Missense Mutation in the Alpha-Actinin 1 Gene (ACTN1) Is the Cause of Autosomal Dominant Macrothrombocytopenia in a Large French Family. *Plos One* 8:e74728.

Haywood NJ, Wolny M, Rogers B, Trinh CH, Yu SP, Edwards TA, Peckham M. 2016. Hypertrophic cardiomyopathy mutations in the calponin-homology domain of ACTN2 affect actin binding and cardiomyocyte Z-disc incorporation. *Biochemical Journal* 473:2485-2493.

Heilemann M, van de Linde S, Mukherjee A, Sauer M. 2009. Super-Resolution Imaging with Small Organic Fluorophores. *Angewandte Chemie-International Edition* 48:6903-6908.

Heilemann M, van de Linde S, Schuttpelz M, Kasper R, Seefeldt B, Mukherjee A, Tinnefeld P, Sauer M. 2008. Subdiffraction-resolution fluorescence imaging with conventional fluorescent probes. *Angewandte Chemie-International Edition* 47:6172-6176.

Hemmings L, Kuhlman PA, Critchley DR. 1992. Analysis of the actin-binding domain of alpha-actinin by mutagenesis and demonstration that dystrophin contains a functionally homologous domain. *Journal of Cell Biology* 116:1369-1380.

Honda K, Yamada T, Endo R, Ino Y, Gotoh M, Tsuda H, Yamada Y, Chiba H, Hirohashi S. 1998. Actinin-4, a novel actin-bundling protein associated with cell motility and cancer invasion. *Journal of Cell Biology* 140:1383-1393.

Houmeida A, Holt J, Tskhovrebova L, Trinick J. 1995. Studies of the interaction between titin and myosin. *Journal of Cell Biology* 131:1471-1481.

Iwamoto DV, Huehn A, Simon B, Huet-Clanderwood C, Baldassarre M, Sindelar C, Clanderwood D. 2018. Structural basis of filamin A actin-binding interaction with F-actin *Nature structural and molecular biology* 25:918-927.

Jefferson JA, Shanland SJ. 2014. The Pathogenesis of Focal Segmental Glomerulosclerosis. *Advances in Chronic Kidney Disease* 21:408-416.

Joseph C, Stier G, O'Brien R, Politou AS, Atkinson RA, Bianco A, Ladbury JE, Martin SR, Pastore A. 2001. A structural characterization of the interactions between titin Z-repeats and the alpha-actinin C-terminal domain. *Biochemistry* 40:4957-4965.

Kazmierski ST, Antin PB, Witt CC, Huebner N, McElhninny AS, Labeit S, Gregorio CC. 2003. The complete mouse nebulin gene sequence and the identification of cardiac nebulin. *Journal of Molecular Biology* 328:835-846.

Koide A, Bailey CW, Huang X, Koide S. 1998. The fibronectin type III domain as a scaffold for novel binding proteins. *Journal of Molecular Biology* 284:1141-1151.

Koide A, Wojcik J, Gilbreth RN, Hoey RJ, Koide S. 2012. Teaching an old scaffold new tricks: monobodies constructed using alternative surfaces of the FN3 scaffold. *Journal of Molecular Biology* 415:393-405.

Kuhlman PA, Hemmings L, Critchley DR. 1992. The identification and characterization of an actin-binding site in alpha-actinin by mutagenesis. *Febs Letters* 304:201-206.

Kunishima S, Okuno Y, Yoshida K, Shiraishi Y, Sanada M, Muramatsu H, Chiba K, Tanaka H, Miyazaki K, Sakai M, Ohtake M, Kobayashi R, Iguchi A, Niimi G, Otsu M, Takahashi Y, Miyano S, Saito H, Kojima S, Ogawa, S. 2013. ACTN1 Mutations Cause Congenital Macrothrombocytopenia. *American Journal of Human Genetics* 92:431-438.

Kunishima S, Saito H. 2006. Congenital macrothrombocytopenias. *Blood Reviews* 20:111-121.

Labeit S, Kolmerer B. 1995. The complete primary structure of human nebulin and its correlation to muscle structure. *Journal of Molecular Biology 248:308-315.*

Labeit S, Kolmerer B. 1995. Titins – Giant proteins in charge of muscle ultrastructure and elasticity. *Science* 270:293-296.

Lebart MC, Mejean C, Casanova D, Audemard E, Derancourt J, Roustan C, Benyamin Y. 1994. Characterization of the actin-binding site on smooth-muscle filamin. *Journal of Biological Chemistry* 269:4279-4284.

Lee SH, Weins A, Hayes DB, Pollak MR, Dominguez R. 2008. Crystal structure of the actin-binding domain of alpha-actinin-4 Lys255Glu mutant implicated in focal segmental glomerulosclerosis. *Journal of Molecular Biology* 376:317-324.

Levine BA, Moir AJG, Patchell VB, Perry SV. 1990. The interaction of actin with dystrophin. *Febs Letters* 263:159-162.

Levine BA, Moir AJG, Patchell VB, Perry SV. 1992. Binding-sites involved in the interaction of actin with the n-terminal region of dystrophin. *Febs Letters* 298:44-48.

Linke WA, Ivemeyer M, Mundel P, Stockmeier MR, Kolmerer B. 1998. Nature of the PEVK-titin elasticity in skeletal muscle. *PNAS* 795:8052-8057.

Linke WA, Rudy DE, Centner T, Gautel M, Witt C. 1999. I-band titin in cardiac muscle is a three-element molecular spring and is critical for maintaining thin filament structure. *Journal of Cell Biology* 146:631-644.

Liu J, Taylor DW, Taylor KA. 2004. A 3-D reconstruction of smooth muscle alpha-actinin by Cryo-EM reveals two different conformations at the actin-binding region. *Journal of Molecular Biology* 338:115-125.

Lopata A, Hughes R, Tiede C, Heissler SM, Sellers JR, Knight PJ, Tomlinson D, Peckham M. 2018. Affimer proteins for F-actin: novel affinity reagents that label F-actin in live and fixed cells. *Scientific Reports* 8:(art. 6572).

Luther PK. 1991. 3-dimensional reconstruction of a simple z-band in fish muscle. *Journal of Cell Biology* 113:1043-1055.

Luther PK. 2000. Three-dimensional structure of a vertebrate muscle Z-band: Implications for titin and alpha-actinin binding. *Journal of Structural Biology* 129:1-16.

Luther PK. 2009. The vertebrate muscle Z-disc: sarcomere anchor for structure and signalling. *Journal of Muscle Research and Cell Motility* 30:171-185.

Luther PK, Barry JS, Squire JM. 2002. The three-dimensional structure of a vertebrate wide (slow muscle) Z-band: Lessons on Z-band assembly. *Journal of Molecular Biology* 315:9-20.

Luther PK, Padron R, Ritter S, Craig R, Squire JM. 2003. Heterogeneity of Z-band structure within a single muscle sarcomere: Implications for sarcomere assembly. *Journal of Molecular Biology* 332:161-169.

Ma K, Wang K. 2002. Interaction of nebulin SH3 domain with titin PEVK and myopalladin: implications for the signalling and assembly role of titin and nebulin. *FEBS Letters* 532:273-278.

Maron BJ, Maron MS. 2015. The 20 advances that have defined contemporary hypertrophic cardiomyopathy. *Trends in Cardiovascular Medicine* 25:54-64.

Marino M, Zou PJ, Svergun D, Garcia P, Edlich C, Simon B, Wilmanns M, Muhle-Gol C, Mayans O. 2006. The Ig doublet Z1Z2: A model system for the hybrid analysis of conformational dynamics in Ig tandems from titin. *Structure* 14:1437-1447.

Moerner WE. 2012. Microscopy beyond the diffraction limit using actively controlled single molecules. *Journal of Microscopy* 246:213-220.

Moncman CL, Wang K. 1995. Nebulette – A 107 kD nebulin-like protein in cardiac muscle. *Cell Motility and the cytoskeleton* 32:205-225.

Moores CA, Keep NH, Kendrick-Jones J. 2000. Structure of the utrophin actin-binding domain bound to F-actin reveals binding by an induced fit mechanism. *Journal of Molecular Biology* 297:465-480.

Morris EP, Nneji G, Squire JM. 1990. The 3-dimensional structure of the nemaline rod z-band. *Journal of Cell Biology* 111:2961-2978.

Millevoi S, Trombitas K, Kolmerer B, Kostin S, Schaper J, Pelin K, Granzier H, Labeit S. 1998. Characterisation of nebulette and nebulin and emerging concepts of their roles for vertebrate Z-discs. *Journal of Cell Biology* 282:111-123.

Mues A, van der Ven PFM, Young P, Furst DO, Gautel M. 1998. Two immunoglobulin-like domains of the Z-disc portion of titin interact in a conformation-dependent way with telethonin. *Febs Letters* 428:111-114.

Murphy ACH, Lindsay AJ, McCaffrey MW, Djinovic-Carugo K, Young PW. 2016. Congenital macrothrombocytopenia-linked mutations in the actin-binding domain of alpha-actinin-1 enhance F-actin association. *Febs Letters* 590:685-695.

Nakayama S, Kretsinger RH. 1994. Evolution of the ef-hand family of proteins. *Annual Review of Biophysics and Biomolecular Structure* 23:473-507.

Nord K, Gunneriusson E, Ringdahl J, Stahl S, Uhlen M, Nygren PA. 1997. Binding proteins selected from combinatorial libraries of an alpha-helical bacterial receptor domain. *Nature Biotechnology* 15:772-777.

North KN, Yang N, Wattanasirichaigoon D, Mills M, Easteal S, Beggs AH. 1999. A common nonsense mutation results in alpha-actinin-3 deficiency in the general population. *Nature Genetics* 21:353-354.

Pappa CT, Bhattacharya N, Cooper JA, Gregorio CC. 2008. Nebulin interacts with CapZ and regulates thin filament architecture within the Z-disc. *Molecular Biology Cell* 19:1837-1847.

Pardee JD, Spudich JA. 1982. Purification of muscle actin. *Methods in Enzymology* 85:164-181.

Park SH, Park S, Kim DY, Pyo A, Kimura RH, Sathirachinda A, Choy HE, Min JJ, Gambhir SS, Hong Y. 2015. Isolation and characterisation of a Monobody with a fibronectin domain III scaffold that specifically binds EphA2. *PLoS One* 10:e0132976.

Pavalko FM, Burridge K. 1991. Disruption of the actin cytoskeleton after microinjection of proteolytic fragments of alpha-actinin. *Journal of Cell Biology* 114:481-491.

Peckys DB, Korf U, de Jonge N. 2015. Local variations of the HER2 dimerization in breast cancer cells discovered by correlative fluorescence and liquid electron microscopy. *Science Advanced* 1:e1500165.

Perz-Edwards RJ, Reedy MK. 2011. Electron Microscopy and X-Ray Diffraction Evidence for Two Z-Band Structural States. *Biophysical Journal* 101:709-717.

Ribeiro ED, **Pinotsis N, Ghisleni A, Salmazo A, Konarev PV, Kostan J, Sjoblom B, Schreiner C, Polyansky AA, Gkougkoulia EA, Holt MR, Aachmann FL, Zagrovic B, Bordignon E, Pirker KF, Svergun DI, Gautel M, Djinovic-Carugo K.** 2014. The Structure and Regulation of Human Muscle alpha-Actinin. *Cell* 159:1447-1460.

Ries J, Kaplan C, Platonova E, Eghlidi H, Ewers H. 2012. A simple, versatile method for GFP-based super-resolution microscopy via nanobodies. *Nature Methods* 9:582-584.

Safarikova M, Reiterova J, Safrankova H, Stekrova J, Zidkova A, Obeidova L, Kohoutova M, Tesar V. 2013. Mutational Analysis of ACTN4. Encoding alpha-Actinin 4, in Patients with Focal Segmental Glomerulosclerosis Using HRM Method. *Folia Biologica* 59:110-115.

Schafer DA, Hug C, Cooper JA. 1995. Inhibition of CapZ during myofibrilgenesis alters assembly of actin-filaments. *Journal of Cell Biology* 128:61-70.

Schierle GSK, van de Linde S, Erdelyi M, Esbjorner EK, Klein T, Rees E, Bertoncini CW, Dobson CM, Sauer M, Kaminski CF. 2011. In Situ Measurements of the Formation and Morphology of Intracellular beta-Amyloid Fibrils by Super-Resolution Fluorescence Imaging. *Journal of the American Chemical Society* 133:12902-12905.

Schlichthaerle T, Eklund AS, Schueder F, Strauss MT, Tiede C, Curd A, Ries J, Peckham M, Tomlinson DC, Jungmann R. 2018. Site-Specific Labeling of Affimers for DNA-PAINT Microscopy. *Angewandte Chemie-International Edition* 57:11060-11063.

Sewry CA, Wallgren-Pettersson C. 2017. Myopathology in congenital myopathies. *Neuropathology and Applied Neurobiology* 43:5-23.

Shams H, Golji J, Garakani K, Mofrad MRK. 2016. Dynamic Regulation of alpha-Actinin's Calponin Homology Domains on F-Actin. *Biophysical Journal* 110:1444-1455.

Singh SM, Mallela KMG. 2012. The N-Terminal Actin-Binding Tandem Calponin-Homology (CH) Domain of Dystrophin Is in a Closed Conformation in Solution and When Bound to F-actin. *Biophysical Journal* 103:1970-1978.

Sjoblom B, Salmazo A, Djinovic-Carugo K. 2008. alpha-actinin structure and regulation. *Cellular and Molecular Life Sciences* 65:2688-2701.

Skrlec K, Strukelj B, Berlec A. 2015. Non-immunoglobulin scaffolds: a focus on their targets. *Trends in Biotechnology* 33:408-418.

Sorimachi H, Freiburg A, Kolmerer B, Ishiura S, Stier G, Gregorio CC, Labeit D, Linke WA, Suzuki K, Labeit S. 1997. Tissue-specific expression and alpha-actinin binding properties of the Z-disc titin: Implications for the nature of vertebrate Z-discs. *Journal of Molecular Biology* 270:688-695.

Sutherland-Smith AJ, Moores CA, Norwood FLM, Hatch V, Craig R, Kendrick-Jones J, Lehman W. 2003. An atomic model for actin binding by the CH domains and spectrin-repeat modules of utrophin and dystrophin. *Journal of Molecular Biology* 329:15-33.

Theis JL, Bos JM, Bartleson VB, Will ML, Binder J, Vatta M, Towbin JA, Gersh BJ, Ornmen SR, Ackerman MJ. 2006. Echocardiographic-determined septal morphology in Z-disc hypertrophic cardiomyopathy. *Biochemical and Biophysical Research Communications* 351:896-902.

Tiede C, Bedford R, Heseltine SJ, Smith G, Wijetunga I, Ross R, Al Qallaf D, Roberts APE, Balls A, Curd A, Hughes RE, Martin H, Needham SR, Zanetti-Domingues LC, Sadigh Y, Peacock TP, Tang AA, Gibson N, Kyle H, Platt GW, Ingram N, Taylor T, Coletta LP, Manfield I, Knowles M, Bell S, Esteves F, Maqbool A, Prasad RK, Drinkhill M, Bon RS, Patel V, Goodchild SA, Martin-Fernandez M, Owens RJ, Nettleship JE, Webb ME, Harrison M, Lippiat JD, Ponnambalam S, Peckham M ,Smith A, Ferrigno PK, Johnson M, McPherson MJ, Tomlinson, DC. 2017. Affimers proteins are versatile and renewable affinity reagents. *Elife* 6:(art. e24903)

Tiede C, Tang AAS, Deacon SE, Mandal U, Nettleship JE, Owen RL, George SE, Harrison DJ, Owens RJ, Tomlinson DC, McPherson MJ. 2014. Adhiron: a stable and versatile peptide display scaffold for molecular recognition applications. *Protein Engineering Design & Selection* 27:145-155.

van de Linde S, Endesfelder U, Mukherjee A, Schüttplez M, Weibusch G, Wolter S, Heilemann M, Sauer M. 2009. Multicolor photoswitching microscopy for subdiffraction-resolution fluorescence imaging. *Photochemical and Photobiological Sciences* 8:465-469.

van de Linde S, Loschberger A, Klein T, Heidbreder M, Wolter S, Heilemann M, Sauer M. 2011. Direct stochastic optical reconstruction microscopy with standard fluorescent probes. *Nature Protocols* 6:991-1009.

Way M, Pope B, Weeds AG. 1992. Evidence for functional homology in the f-actin binding domains of gelsolin and alpha-actinin - implications for the requirements of severing and capping. *Journal of Cell Biology* 119:835-842.

Weins A, Kenlan P, Herbert S, Le TC, Villegas I, Kaplan BS, Appel GB, Pollak MR. 2005. Mutational and biological analysis of alpha-actinin-4 in focal segmental glomerulosclerosis. *Journal of the American Society of Nephrology* 16:3694-3701.

Weins A, Schiondorff JS, Nakamura F, Denker BM, Hartwig JH, Stossel TP, Pollak MR. 2007. Disease-associated mutant alpha-actinin-4 reveals a mechanism for regulating its F-actin-binding affinity. *Proceedings of the National Academy of Sciences of the United States of America* 104:16080-16085.

Westbury SK, Turro E, Greene D, Lentaigne C, Kelly AM, Bariana TK, Simeoni I, Pillois X, Attwood A, Austin S, Jansen SBG, Bakchoul T, Crisp-Hihn A, Erber WN, Favier R, Foad N, Gattens M, Jolley JD, Liesner R, Meacham S, Millar CM, Nurden AT, Peerlinck K, Perry DJ, Poudel P, Schulman S, Schulze H, Stephens JC, Furie B, Robinson PN, van Geet C, Rendon A, Gomez K, Laffan MA, Lambert MP, Nurden P, Ouwehand WH, Richardson S, Mumford AD, Freson K. 2015. Human phenotype ontology annotation and cluster analysis to unravel genetic defects in 707 cases with unexplained bleeding and platelet disorders. *Genome Medicine* 7: (art. 36).

Yasutomi M, Kunishima S, Okazaki S, Tanizawa A, Tsuchida S, Ohshima Y. 2016. ACTN1 rod domain mutation associated with congenital macrothrombocytopenia. *Annals of Hematology* 95:141-144.

Ylanne J, Scheffzek K, Young P, Saraste M. 2001. Crystal structure of the alpha-actinin rod reveals an extensive torsional twist. *Structure* 9:597-604.

York AG, Ghitani A, Vaziri A, Davidson MW, Shroff H. 2011. Confined activation and subdiffractive localization enables whole-cell PALM with genetically expressed probes. *Nature Methods* 8:327-U373.

Young P, Ferguson C, Banuelos S, Gautel M. 1998. Molecular structure of the sarcomeric Z-disk: two types of titin interactions lead to an asymmetrical sorting of alpha-actinin. *Embo Journal* 17:1614-1624.

Young P, Gautel M. 2000. The interaction of titin and alpha-actinin is controlled by a phospholipid-regulated intramolecular pseudoligand mechanism. *Embo Journal* 19:6331-6340.

Zou PJ, Pinotsis N, Lange S, Song YH, Popov A, Mavridis I, Mayans OM, Gautel M, Wilmanns M. 2006. Palindromic assembly of the giant muscle protein titin in the sarcomeric Z-disk. *Nature* 439:229-233.